Reducing Reactive Astrogliosis *in vitro* using Altered Gravity

Dissertation

zur

Erlangung des Doktorgrades (Dr. rer. nat.)

der

Mathematisch-Naturwissenschaftlichen Fakultät

der

Rheinischen Friedrich-Wilhelms-Universität Bonn

vorgelegt von

Yannick Gennady Lichterfeld

aus

Gütersloh

Bonn, Juli 2023

Angefertigt mit Genehmigung der Mathematisch-Naturwissenschaftlichen Fakultät
der Rheinischen Friedrich-Wilhelms-Universität Bonn

1. Gutachterin: PD Dr. Ruth Hemmersbach
2. Gutachter: Prof. Dr. Walter Witke

Tag der Promotion: 10.01.2024

Erscheinungsjahr: 2024

Table of Contents

Abbreviations

°C	degree Celsius
µg	microgram
µL	microliter
µM	micromolar
µ*g*	microgravity
s-µ*g*	simulated microgravity
MuSIC	Multi-Sample Incubator Centrifuge
SAHC	Short-Arm Human Centrifuge
g	gravitational constant
DLR	Deutsches Zentrum für Luft und Raumfahrt
ISS	International Space Station
m	meter
rpm	rotations per minute
mm	millimeter
CNS	Central nervous system
SANS	Spaceflight Associated Neuro-ocular Syndrome
PNS	Peripheral nervous system
BBB	Blood brain barrier
ATP	Adenosine triphosphate
GFAP	Glial fibrillary acidic protein
LZK	Leucin zipper-bearing kinase
ECM	Extracellular matrix
EGF	Epidermal growth factor
FGF	Fibroblast growth factor
CPSG	Chondroitin sulfate proteoglycan
FAK	Focal adhesion kinase

Abstract

Astrocytes are the prevalent type of glial cells in the brain and the whole central nervous system. In case of an injury or illness to the central nervous system (CNS), astrocytes in the surrounding tissue become reactive. Astrocytic reactivity is characterized by various complex phenotypic changes including hypertrophy, hyperproliferation, gene expression changes such as upregulation of GFAP (glial fibrillary acidic protein), and loss of clearly defined spatial astrocyte domains, connected to the migration of astrocytes to the region of injury. In case of severe trauma, the infiltration of astrocytes leads to reactive astrogliosis and ultimately to glial scarring. Reactive astrocytes form a scar-like barrier around the lesion by secreting a dense extracellular matrix and recruiting microglia and fibroblasts to prevent the intrusion of pathogens. Aside from these necessary functions to confine the injury, the glial scar negatively affects the regrowth of neuronal axons in the injured tissue leading to long-lasting obstruction of nerve fibers through the scar tissue, and in turn at worst case paralysis of patients.

In this thesis, altered mechanical loading achieved by hypergravity exposure on centrifuges or simulated microgravity on clinostats were evaluated as non-invasive methods to modify astrocyte behavior and reactivity. Primary murine cortical astrocytes were exposed to various gravity conditions and key parameters of astrocytic reactivity were investigated by biochemical assessment, live-cell, super-resolution and epifluorescence microscopy.

Hypergravity in the physiological range of 2*g* induced deficits in initial and long-term spreading of astrocytes with a reduction in cell area of app. 20-45%. Additionally, a reduction in migration velocities of astrocytes in a time-dependent manner was observed, indicating adaptive processes to hypergravity and readaptation to normal gravity. In parallel, STED microscopy revealed changes in the amount of cortical actin and less polarized lamellipodia as well as altered microtubule network polarization under hypergravity.

Cell proliferation and apoptosis under hypergravity were unchanged as compared to 1*g* controls. Interestingly, at the same time astrocyte reactivity marker protein expression was reduced, indicating that physiological hypergravity can be used to modulate reactivity *in vitro.*

Cultivation in simulated microgravity reduced cell spreading by app. 20-30% accompanied by changes in morphological parameters. No changes in astrocyte reactivity, proliferation or microtubule network integrity were measured.

Altogether, altered gravity exposure is a promising method to modify cellular behavior *in vitro*, potentially leading to new avenues of therapy for patients to control astrocytic reactivity and ultimately glial scarring *in vivo*.

1. Introduction

1.1 Gravity – definition and experimental approaches

Gravity is one of the four fundamental forces of physics and moves with approximately the speed of light (Cornish, Blas et al. 2017). Every object that has a mass also exerts a gravitational force on its surroundings, and thus Earth itself has a gravitational pull on its surface equaling an acceleration approximating 9.81 m/s² (Crossley, Hinderer et al. 2013). This normal Earth gravity is designated with the unit *g*.

Since the beginning of life on Earth, all living beings have developed under an enormous variety and fluctuation of environmental stimuli. Thus, the only consistent factor throughout the entire evolution of life is constant 1*g* gravity. As such, gravity is an important evolutionary factor and organisms have developed different ways of sensing gravity in order to use this environmental constant e.g. for orientation, directional growth and polarization. Highly suitable to investigate the effect of orientation in a medium is the in gravitaxis of single-celled organisms, as well as gravitropism for directional growth of plants (Braun, Böhmer et al. 2018). Gravisensory structures identified so far in some model systems range from mechano-sensitive ion channels in the cell membrane of unicellular gravitactic organisms (e.g., the ciliate Paramecium and the flagellate Euglena), specialized organelles in cells in plants (statocytes in roots) (Häder, Braun et al. 2017, Braun, Böhmer et al. 2018), to complex vestibular systems in higher animals and humans (Hanke, Kohn et al. 2018). However, it is an open question whether graviperception is a common cellular capacity and in this case, the underlying mechanisms still need to be investigated in more detail. Experiments in human-related cell cultures, e.g. of human or murine cells *in vitro*, under altered gravity conditions demonstrate changes in cellular physiology and signaling pathways, indicating that single cells react to changes in their gravitational environment (Häder, Braun et al. 2017).

The investigation of potential gravisensitive structures and pathways is performed on mostly custom-designed and sophisticated gravity research platforms. Altered gravity conditions are thus applied on platforms generating increased gravity (hypergravity) such as centrifuges, or reduced gravity such as real microgravity (µ*g*, i.e. weightlessness) on rockets, satellites and space stations (Herranz, Anken et al. 2013, Frett, Petrat et al. 2015, Liemersdorf, Lichterfeld et al. 2020, Grimm, Schulz et al. 2022). For short periods of time, real microgravity can also be generated using free fall in a drop tower and in parabolic flights (Corydon, Kopp et al. 2016, Hauslage, Cevik et al. 2017, Wuest, Arnold et al. 2020). Since achieving real microgravity requires immense technical and financial effort, platforms to simulate microgravity (s-µ*g*) on Earth have been developed (Herranz, Anken et al. 2013). Already in 1882, Julius Sachs

developed the first kind of microgravity simulator, a so-called clinostat (Sachs 1882). He used a slow-rotating clinostat to study and discern the influence of gravity (gravitropism) and light (phototropism) on plant growth.

Nowadays, different rotation-based platforms (clinostats, random positioning machines) have been developed to expose plants, cells and small organisms to alter the impact of gravity. The aim is to achieve simulated microgravity conditions, that means creating an environment which prevents sedimentation and the registration of the gravitational stimulus comparable to the situation in real microgravity, using the clinostat principle (see Figure 3C). The various platforms are characterized by different rotation speed, number of rotation axes and directions. Comparative studies and careful control experiments with the focus on residual accelerations and device-induced disturbing factors such as shear forces and vibration, as well as comparison to data obtained in real microgravity are necessary to choose and define the experimental conditions to solve a gravity-related question (Herranz, Anken et al. 2013, Hauslage, Cevik et al. 2017).

Research in the field of gravitational biology and physiology is motivated on one hand by the challenges on the human body posed by space flight. The human body responds to and has to adapt to the new experienced environmental condition under long periods of real microgravity exposure. Astronauts on the International Space Station (ISS) experience unpleasant periods of nausea and headache when arriving on orbit, caused by adjustments of the vestibular system and changes in the fluid distribution of the body. Long-term consequences of microgravity exposure to the human body produce unusual physiological and pathological effects revealed e.g. by neuro-ophthalmic findings in astronauts, as well as decreases in muscle and bone mass (LeBlanc, Lin et al. 2000, Lee, Mader et al. 2020, Martin Paez, Mudie et al. 2020). Functioning of the immune system is also impaired in astronauts in microgravity with a severe potential health risk (Crucian, Cubbage et al. 2000, Paulsen, Thiel et al. 2010, Wollseiffen, Klein et al. 2019). Cognitive dysfunction, spatiotemporal abnormalities and other neuronal symptoms are observed in astronauts as well, described in detail below (see 1.1.1).

Science in altered gravity does not only profit astronauts´ health, as many of the findings can and have been translated to applications for patients on Earth. This includes disorders such as muscle deterioration, disturbed vestibular, immune functions and cardiac diseases. Additionally, altered gravity and thus altered mechanical loading can be employed as a stimulus for cellular, plant, and animal systems to investigate responses on a molecular level on Earth or to create three-dimensional tissue cultures or organoids (Grimm, Egli et al. 2018).

As stated above, a multitude of gravity research platforms have been developed at DLR and evaluated to perform experiments under altered gravity conditions.

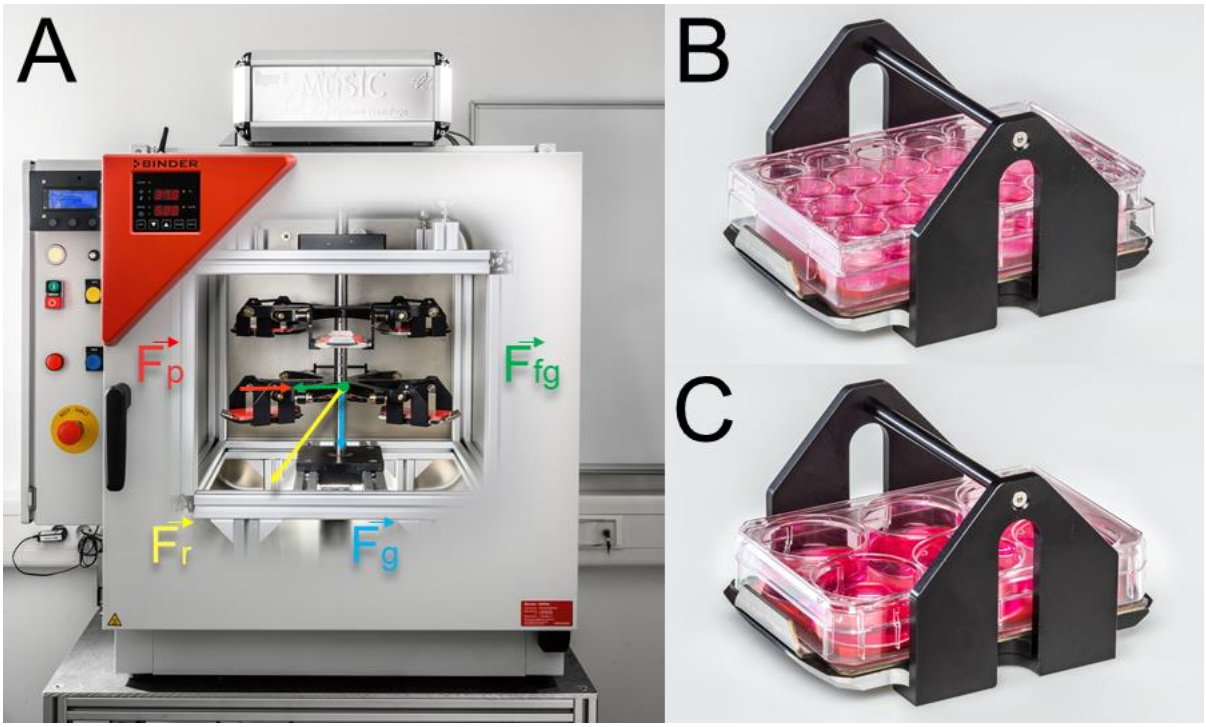

Figure 1: The Multi-Sample Incubator Centrifuge (MuSIC). (A) Front view of the centrifuge device inside the incubator, with the exerted and resulting forces marked with arrows. F_p: Centripetal force, F_{fg}: centrifugal force, F_r: resultant force, F_g: gravitational force. **(B)** One centrifuge gondola with a 24-well plate installed. The swing-out gondolas ensure a perpendicular *g* vector onto the sample to avoid shear forces. **(C)** One gondola with a 6-well plate installed. Various other cell culture vessels can be employed. The MuSIC supplies 37°C, >90% humidity, and 5% CO2. Maximum acceleration 50*g* with a ramp-up time of 3 s.

To subject various biological sample types to hypergravity, the Multi-Sample Incubator Centrifuge (MuSIC) was developed within the scope of this thesis (see Figure 1). It consists of a cell culture incubator with an integrated swing-out centrifuge platform (see 4.1.1). Here, a variety of cell culture vessels from slides and tubes to plates and flasks can be subjected to hypergravity of up to 50*g* for durations ranging from seconds to weeks in otherwise standardized cell culture conditions such as 37°C, >90% humidity, and 5% CO_2. This device is used in the current studies for moderately increased gravitational loading in a physiological range of 2*g* – 10*g*. The MuSIC can further be employed to generate the essential controls to discriminate hypergravity effects occurring in parabolic flights of airplanes or during rocket launches from microgravity-induced changes. The main challenge in altered gravity experiments is to separate the observed gravity-dependent effects and phenotypes from all other confounding factors or interferences. For this reason, any devices have to be vibration-free and the sample environment has to mirror that of the 1*g* control and baseline data with regards to e.g., temperature, gas composition, humidity or nutrient supply.

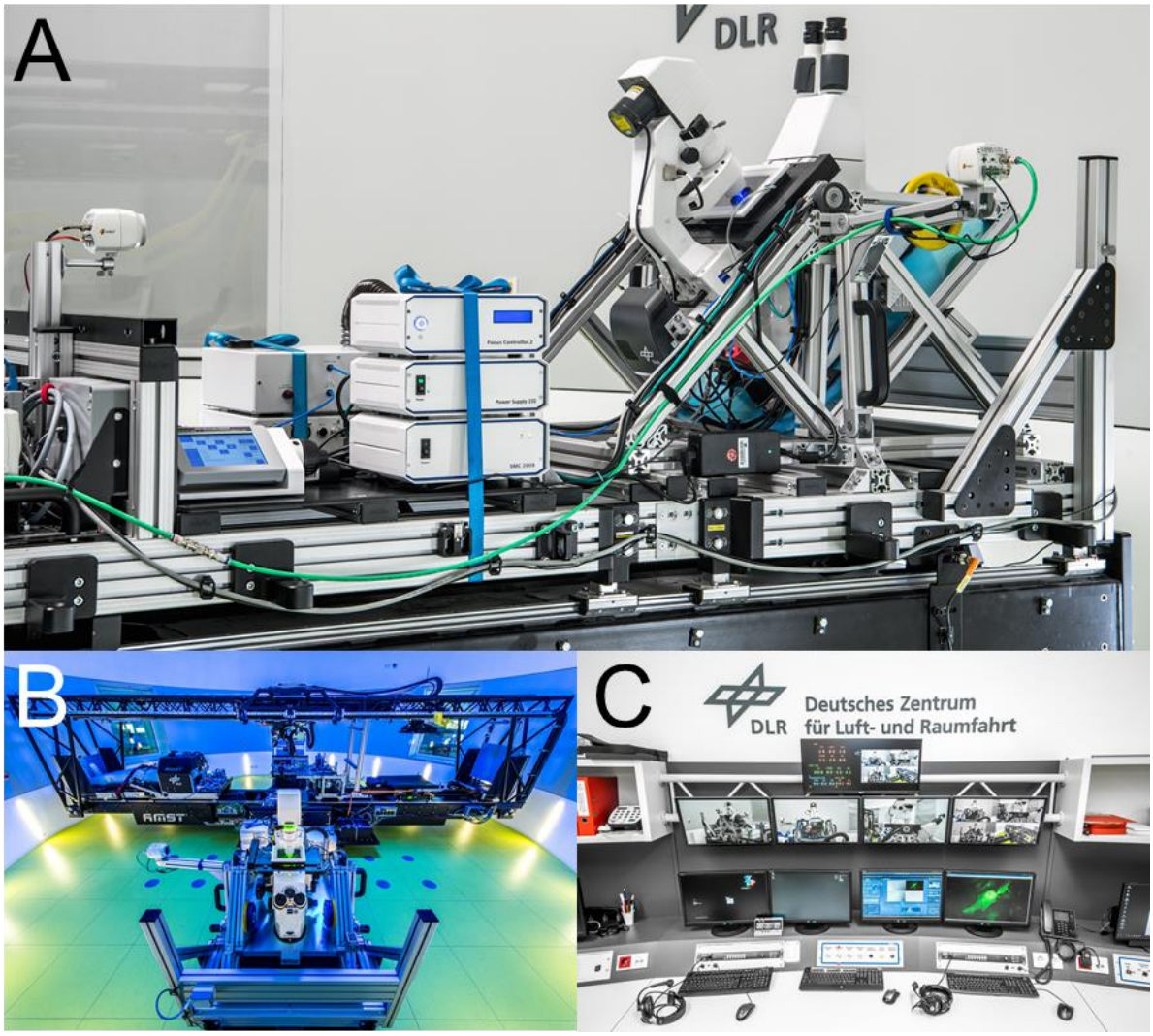

Figure 2: The Hyperscope. Live-cell microscopy under hypergravity. (A) Side view of the Hyperscope platform. A Zeiss Axio Observer microscope installed on a swing-out platform with the support electronics installed on the centrifuge arm. **(B)** Front view of the Hyperscope with all four centrifuge arms visible behind it. **(C)** Control room showing the experiment operator working space. The short-arm centrifuge has a 3.8m diameter and can accelerate to max. 4*g*. All microscope settings can be remote controlled also during centrifugation.

The DLR :envihab research facility houses the short-arm human centrifuge (SAHC). This centrifuge with a radius of 3.8 m can sustain a maximum acceleration of 6*g* and is mostly used for human physiological studies. During the scope of this thesis, a Zeiss Axio Observer epifluorescence live-cell microscope was integrated on a swing-out platform, called Hyperscope. The Hyperscope is designed for fluorescent and wide field microscopy on living cells under up to 2*g* hypergravity (see Figure 2, 4.1.2). While exposing living samples to hypergravity in otherwise optimal cell culture conditions, including temperature and CO_2 control, they can be imaged remotely and fully automated with live feedback for the operator to modify imaging parameters on the fly during centrifugation. The short arm centrifuge runs virtually vibration free, and the microscope incubation top is protected from wind and can ensure a constant temperature and gas supply to the sample.

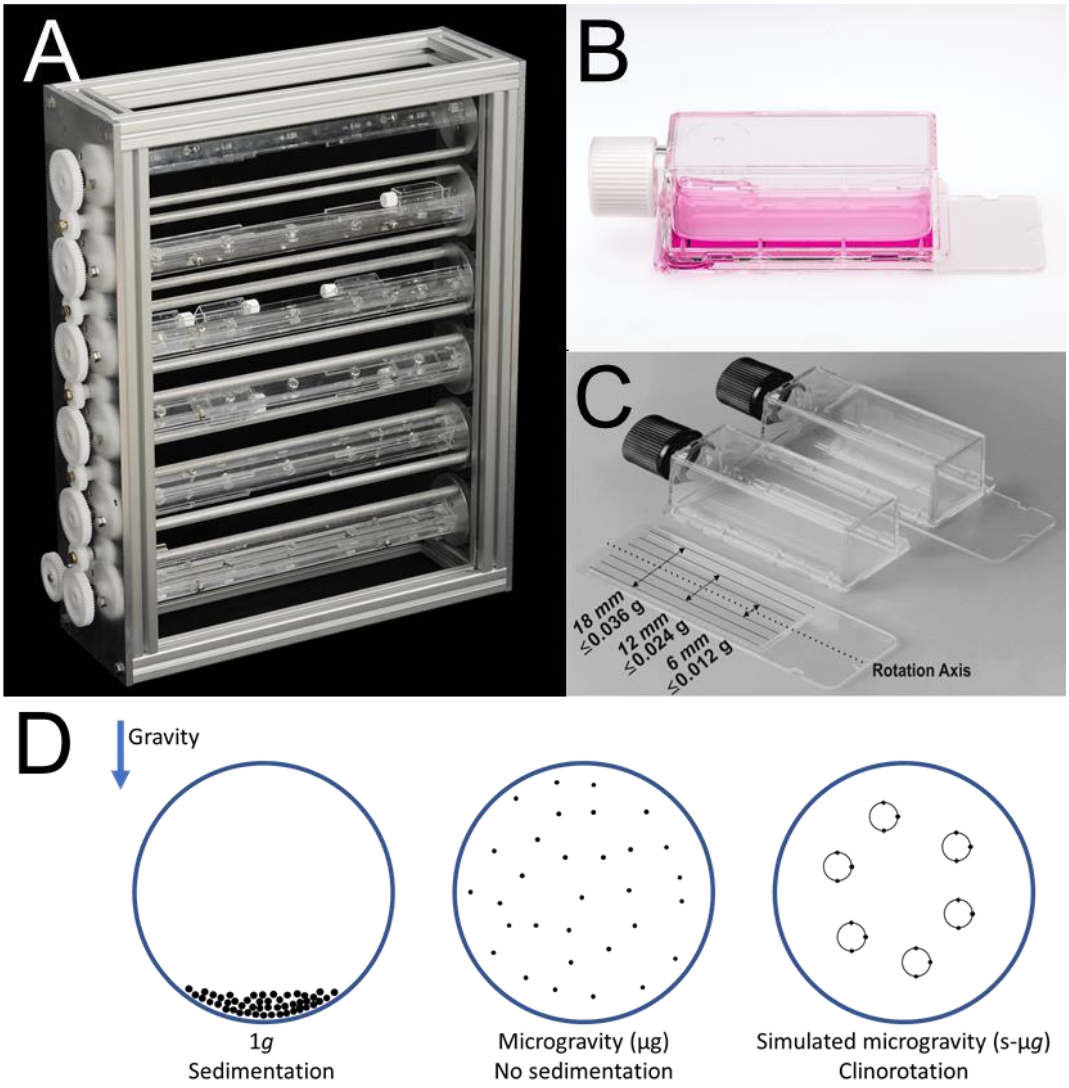

Figure 3: The slide flask clinostat for simulated microgravity exposure. (A) Front view of the slide flask clinostat with six rotating axes for four slide flasks each. **(B)** Side view of one slide flask, the growth surface for adherent cells situated on the bottom. **(C)** The quality of simulated microgravity is optimal near to the rotation axis +(Eiermann, Kopp et al. 2013). **(D)** Schematic of the clinostat principle.

For the simulation of microgravity, several types of clinostats are available at DLR (see 4.1.3). By constant rotation around one axis of the sample, sedimentation and thus the registration of gravity in the sample is prevented. This mode of action is called the clinostat principle (see Figure 3C) For the exposure of adherent cells to s-µ*g* the so-called slide flask clinostat is employed in this thesis (see Figure 3). It consists of five axes rotating in parallel which can each hold up to 4 slide flasks. Cells grown on the slide flask are situated close to the axis of rotation when the slide flask is integrated into the clinostat. At a constant rotation speed of 60 rpm all cells lying within three millimeters of the rotation axis center will perceive a maximum acceleration of ≤ 0.006*g*. The further away a sample is from the rotational axis, the more residual g-forces it will be subjected to (Eiermann, Kopp et al. 2013). For this reason, it is

advised to mostly analyze the middle region with the highest quality of simulated microgravity for analyses.

1.1.1 Altered gravity and the central nervous system

The extreme environmental conditions of space, especially radiation and microgravity, exert diverse and often detrimental effects on the human body. It is known that the brain and central nervous system (CNS) are influenced, studies on astronauts and model animals have shown changes in the CNS on a cellular as well as functional and morphological level leading to various impairments (Charles M. Oman 2003, Kalb 2003, Van Ombergen 2018, Popova, Kulikov et al. 2020). It has been reported that space flight has a negative impact on cognitive performance and focus (Kanas and Manzey 2008). A decrease in neuronal plasticity and changes in grey matter distribution were detected with MRI scans of astronaut brains (Demertzi, Van Ombergen et al. 2016, Koppelmans, Bloomberg et al. 2016, Van Ombergen, Demertzi et al. 2017, Ombergen 2018, Donna R Roberts and Rachael D Seidler 2020). Microgravity exposure strongly impacts the optical nerve and associated system in astronauts and leads to increased intracranial pressure with long-term effects on astronauts' eyesight, summarized as Spaceflight Associated Neuro-ocular Syndrome (SANS) (Martin Paez, Mudie et al. 2020).

Most of the studies related to the nervous system in real microgravity have been behavioral and non-invasive with few studies focused on the cellular level. In this context, a study on rat hair cells identified a significant increase in synapses after 9 days of real microgravity (Ross 2009). Of the different neuronal cell types, neurons have been of most interest with regards to studies in microgravity. Changes in the distribution of neuronal subgroups and number of motor neurons in the spinal cord of rats have been reported after 30 days of microgravity exposure on the Bion-M1 satellite (Porseva, Shilkin et al. 2017). When exposed to hypergravity, neuron-like PC12 cells demonstrated increased neurite growth, cell area, and changes in microtubule filament distribution (Genchi, Cialdai et al. 2015).

Until now, there have been little to no conclusive reports on astrocytes, the major type of glial cell, in microgravity on a cellular level. Studies on glial cells from a C6 glioma cell line on a Random Positioning Machine (RPM) used in a fast and constant 2D clinorotation mode (60 rpm) showed immediate damage to the cytoskeleton after 30 minutes of exposure and highly increased apoptosis rate, which according to the investigators' hypothesis, might have severe consequences for astronauts (Uva, Masini et al. 2002). Interestingly, the cytoskeletal disruptions were alleviated after 24 hours of clinorotation. However, it has to be kept in mind, that these simulation approaches have so far not been evaluated in real microgravity. The neuronal glioblastoma cell line, SH-SY5Y, was exposed to alternating micro- and hypergravity on a parabolic flight and constant 2*g* hypergravity on ground and showed spontaneous and

evoked lamellar protrusive activity. Gravity-dependent microtubular rearrangements in SH-SY5Y cells were stated after parabolic flights or after 20 minutes of clinorotation (60 rpm), but not after 2*g* hypergravity (Rosner, Wassermann et al. 2006). In summary, so far, no conclusive model of astrocyte or any glial cell type functions under altered gravity exists. This is not only the case for astrocytes, but also for other more intensively studied cell types that are still lacking conclusive insights into gravi-sensitive mechanisms on a cellular level (Häder, Braun et al. 2017). Endothelial cells, for example, are easier to culture and handle in vitro and thus are studied more frequently under altered gravity in flight and in ground simulations. But still, there are quite discordant results regarding cellular migration, proliferation, apoptosis, gene expression and cytoskeletal dynamics (Maier, Cialdai et al. 2015).

1.2 The central nervous system

The central nervous system (CNS) encompasses the brain as well as the spinal cord, in contrast to the peripheral nervous system (PNS), which contains ganglia, sensory nerve fibers and neuromuscular junctions. The CNS receives and integrates input from the PNS, relays information and gives commands as outputs via electrochemical potentials. Cells in the CNS can be roughly divided into neurons, which transmit electrical signals via action potentials, and glial cells.

The population of glial cells in the CNS comprises four subtypes: astrocytes, oligodendrocytes, microglia and ependymal cells (Jakel and Dimou 2017).

Astrocytes have various functions, such as delivering nutrients to neurons, giving structural support and removing residual neurotransmitters from the intracellular space. Recently, astrocytes have been increasingly implicated in fine regulations of nervous function via gliotransmitter release as well as receptor uptake and trafficking towards neurons. In the case of an injury to the CNS tissue, astrocytes have the property to become reactive and form glial scar tissue which is the focus of this thesis.

Oligodendrocytes engage in bidirectional communication with neurons and form myelin sheaths around axons, resulting in highly increased conduction velocity of action potentials and in turn improve the metabolic efficiency and information processing capacity of the CNS (Thornton and Hughes 2020).

Microglia are immunocompetent cells of the CNS with phagocytic capacities. They remove apoptotic material and cell debris from neuronal tissue and are activated by inflammatory signals. Furthermore, they are involved in synaptic pruning in brain development and also in the adult brain (Jakel and Dimou 2017).

Ependymal cells are ciliated epithelia-like cells that line the ventricular surface of the CNS. They are implicated in neurogenesis and in the control and production of cerebrospinal fluid (Del Bigio 2010).

1.2.1 Key characteristics of astrocytes

Astrocytes are the most abundant type of glial cell in the brain and CNS, with ratios varying between 20 and 40% of the total number of cells depending on the brain region (von Bartheld, Bahney et al. 2016). These cells have supportive, active, and homeostatic functions. Astrocytes *in vivo* are present as finely branched, star-like cells. In addition to their role in most areas of the brain and spinal cord, with those thousands of processes, astrocytes link their surrounding neurons and cerebral endothelial cells, forming the blood brain barrier (BBB). Thus, every astrocyte has a three-dimensional volume, which is usually not invaded by other astrocytes, and interacts with up to 2 million synapses (Fields, Araque et al. 2014). One important function is the metabolic support of connected neurons by forming the tripartite synapse together with the pre- and postsynaptic membranes (Allen and Eroglu 2017). Astrocytes supply lactate and other nutrients to neurons and act as a glycogen fuel reserve buffer by distributing glucose to their surrounding cells in times of high rate of consumption or exhaustive physical exercise (Matsui, Ishikawa et al. 2012). These processes are thought to be regulated in part by astrocytic insulin signaling (Garcia-Caceres, Quarta et al. 2016).

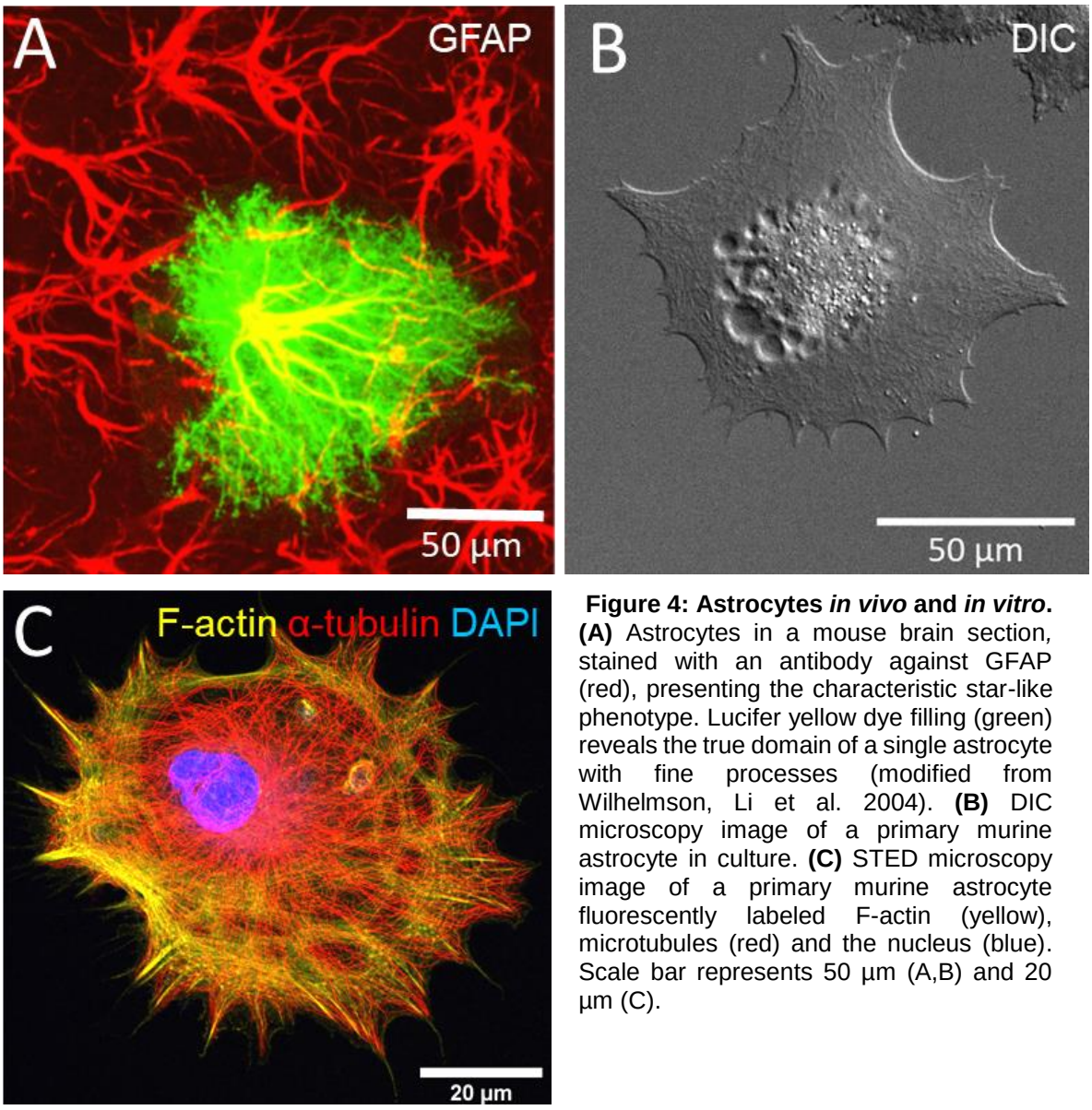

Figure 4: Astrocytes *in vivo* and *in vitro*. **(A)** Astrocytes in a mouse brain section, stained with an antibody against GFAP (red), presenting the characteristic star-like phenotype. Lucifer yellow dye filling (green) reveals the true domain of a single astrocyte with fine processes (modified from Wilhelmson, Li et al. 2004). **(B)** DIC microscopy image of a primary murine astrocyte in culture. **(C)** STED microscopy image of a primary murine astrocyte fluorescently labeled F-actin (yellow), microtubules (red) and the nucleus (blue). Scale bar represents 50 µm (A,B) and 20 µm (C).

Unlike neurons, astrocytes are not electrically excitable (Verkhratsky and Nedergaard 2018). They do, however, display intracellular calcium ion activity within single astrocytes and across syncytia of multiple astrocytes (Semyanov, Henneberger et al. 2020). It is hypothesized, that calcium elevation in astrocytes results in release of gliotransmitters to modulate neuronal function and neurovascular coupling, although direct connections between astrocyte calcium activity and synaptic activity and plasticity are still debated (Agulhon, Fiacco et al. 2010, Bazargani and Attwell 2016). In *in vivo* mouse models, locomotion-driven Ca2+ gradients could be observed in astrocytes in the brain (King, Bohmbach et al. 2020), and relations between Ca2+-related neurotransmitter release attributed to astrocytes and astrocyte reactivity are suspected (Agulhon, Sun et al. 2012).

In dependence on Ca2+ signaling, but also independent from it, astrocytes release ATP into their extracellular environment. ATP is hydrolyzed to adenosine and can bind to neuronal

receptors and in consequence inhibit synaptic transmission. In addition, axonal myelination by oligodendrocytes is promoted by ATP release (Ishibashi, Dakin et al. 2006). Large amounts of calcium-independent ATP release are proposed to be a form of damage response and support the recruitment of microglia in case of injury (Xiong, Sun et al. 2018).

Astrocytes play a key part in the regulation of extracellular potassium homeostasis in the brain, by clearing increased extracellular ion concentrations resulting from neuronal signaling via potassium channels in their membranes (Walz 2000).

1.2.2 Astrocyte reactivity and reactive astrogliosis

In addition to their crucial role in normal cognitive function, astrocytes also play a key role in the response of the CNS to illness, physical damage or injury via the process of reactive astrogliosis, which is the focus of this thesis. Astrocytes in the CNS can respond to injury or diseases of all severities with changes on a molecular, cellular, and functional level. These changes are controlled by intra- and extracellular signaling molecules and can positively, as well as negatively impact the surrounding neuronal and non-neuronal cells (Pekny and Nilsson 2005, Sofroniew 2009, Sofroniew and Vinters 2010, Omura, Omura et al. 2015, Liddelow and Barres 2017, Escartin, Galea et al. 2021) (see Figure 5).

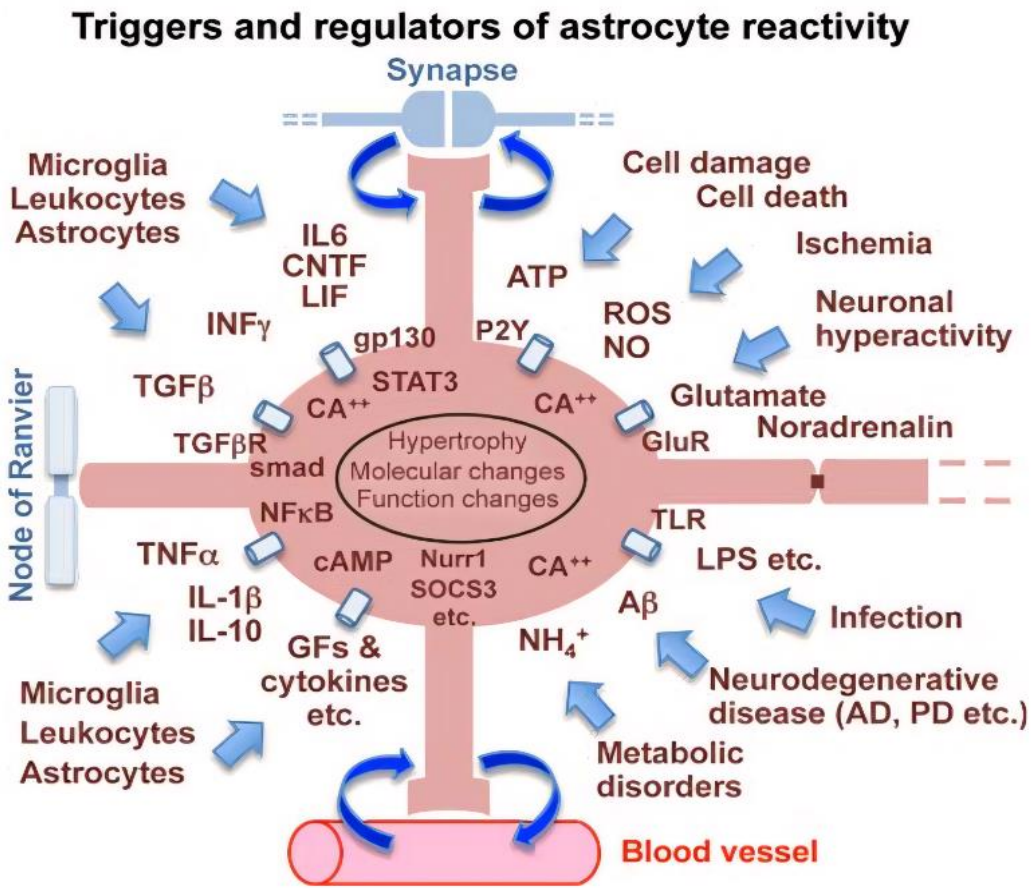

Figure 5: Intra- and extracellular signaling molecules and factors known to trigger astrocyte reactivity. Signaling from surrounding glia cells, the connection to synapses, Nodes of Ranvier or the blood brain barrier as well as a multitude of signaling molecules and cytokines diffusing through the CNS can trigger or regulate astrocyte reactivity (modified from Sofroniew and Vinters 2010).

Astrocytic alterations vary with the severity of the damage, starting with the mild to moderate reactive astrogliosis which includes upregulation of reactivity-associated genes such as GFAP and hypertrophy of cell bodies and processes but no entwining of astrocytic domains at these

stages (Sofroniew and Vinters 2010). This earliest form of astrogliosis is usually associated with mild trauma, systemic viral or bacterial infections, or seen in cells in some distance to CNS lesions, however the cellular changes are mostly reversible (Sofroniew and Vinters 2010). In the case of a severe diffuse reactive astrogliosis, a pronounced GFAP expression and pronounced hypertrophy of cell bodies and processes are observed (Pekny and Nilsson 2005). This leads to substantive overlapping of single astrocyte domains and can result in long-lasting modifications of the affected tissue, observed in areas close to focal CNS lesions or in neurodegenerative disorders (Escartin, Galea et al. 2021).

Severe reactive astrogliosis with compact glial scar formation encompasses all hallmarks of milder types of astrogliosis such as GFAP expression and cellular hypertrophy. Additionally, reactive astrocytes lose their individual domains and increase their proliferation and cellular maintenance as well as initiate migration into the damaged region. Ultimately, reactive astrogliosis can lead to the formation of a glial scar (Lagos-Cabre, Burgos-Bravo et al. 2019). In the case of compact glial scar formation, the involved reactive astrocytes are also described as scar-forming astrocytes (Okada, Nakamura et al. 2006, Sofroniew and Vinters 2010, Hur, Saijilafu et al. 2012, Okada, Hara et al. 2018).

1.2.3 Molecular markers of reactive astrocytes

Reactive astrocyte populations *in vivo* and *in vitro* are most commonly characterized by a major increase in astrocytic glial fibrillary acidic protein (GFAP) expression. Thus, GFAP is widely used as a specific marker for reactive astrocytes. Expression of this type of intermediate filament is highest in reactive and scar-forming astrocytes where nearly all cells responding to CNS injuries have a high intracellular GFAP concentration. In healthy non-reactive astrocytes, or in the ones distant from CNS lesions, GFAP is usually expressed only at basal levels (Sofroniew and Vinters 2010). Since reactive astrogliosis is a multistage and complex process, more molecular expression markers are necessary to reliably identify variations in astrocyte reactivity. Proteins known to be modulated in reactive astrogliosis are vimentin, nestin and LZK (MAP3K13), which were selected together with GFAP for an immunofluorescence reactivity panel in this thesis (Sofroniew 2009, Nathan and Li 2017, Chen, Geoffroy et al. 2018). Other proteins regulated by astrogliosis are e.g. β-catenin, n-cadherin and S100-β (Chadi 1999, Cunningham, Wetzel et al. 2005, Yang, Iyer et al. 2012, Hara, Kobayakawa et al. 2017). The matrix-metalloproteases MMP2 and MMP13 have been found to be expressed in reactive, migrating astrocytes, but not in stationary, scar-forming astrocytes (Verslegers, Lemmens et al. 2013).

Vimentin and nestin are, like GFAP, intermediate filaments. They are upregulated in reactive astrocytes, with vimentin upregulated also in scar-forming astrocytes and nestin only at the earlier reactive state (Nathan and Li 2017). Ablation of GFAP or vimentin led to no changes in

astrogliosis, but deleting both genes impaired glial scar formation (Pekny, Johansson et al. 1999). In mice lacking LZK, an enzyme which is upregulated in the nuclei of astrocytes after CNS injury, astrogliosis was impaired and lesion size after spinal cord injury increased, while conversely LZK overexpression led to an enhanced astrogliosis (Chen, Geoffroy et al. 2018).

1.2.4 Glial scar formation and neuronal regeneration

In the case of severe injury to the CNS, naive astrocytes in the surrounding tissue become reactive, triggered by molecular cues such as EGF, FGF, endothelin 1, myelin debris and ATP (Sofroniew 2009, Hur, Saijilafu et al. 2012). This process is characterized by intermediate filament expression, hypertrophy, hyperproliferation, enhanced cellular maintenance, and migration to the damaged region (Zhan, Gao et al. 2017). These scar-forming astrocytes are the key players in glial scar formation or astrogliosis, accompanied by microglia and meningeal fibroblasts (see Figure 6). The glial scar is formed by an aggregation of hypertrophic and proliferating reactive astrocytes which form a border between the lesion and the surrounding healthy CNS tissue, acting as a neuroprotective barrier for inflammatory cells and infectious agents (Sofroniew and Vinters 2010). Nearly half of the astrocytes closest to a CNS injury are morphologically strongly polarized, perpendicular to the injury (Schiweck, Eickholt et al. 2018). Scar-forming reactive astrocytes secrete a dense, collagenous extracellular matrix (ECM), rich in cytokines and molecules that inhibit axonal and cellular regeneration. One key group of inhibitory ECM molecules secreted by reactive astrocytes are chondroitin sulfate proteoglycans (CPSGs) (Kamermans, Planting et al. 2019). CPSGs are known to inhibit axonal regrowth by causing dystrophic growth cones in the affected neurons, and in turn inhibition of CPSG production led to improved axonal regeneration after trauma (Erturk, Hellal et al. 2007, Bradbury and Carter 2011).

In summary, glial scar formation has positive and negative consequences for neuronal tissue affected by injury or inflammation. As an intermediary and essential step for the conservation of the CNS, the glial scar forms a barrier around the lesion and prevents spreading of the injury. Leukocyte infiltration is reduced and repair of the damaged BBB is promoted (Pekny and Pekna 2014). The microenvironment in the glial scar can have pro- and anti-inflammatory effects on microglia, helping with the clearance of apoptotic cells and debris. In neurodegenerative diseases, glial scarring also slows down disease progression (Kraft, Hu et al. 2013). Negative effects of glial scarring are primarily the inhibition of neuronal regeneration by limiting the synaptic regeneration and axonal regrowth capabilities of affected neurons. This is critical especially, since the glial scar is a long-lasting remodeling of the affected CNS tissue which persists even after the injury has been resolved. Neural grafts or stem cell therapies are also affected by these negative effects of astrocyte reactivity (Sofroniew 2009, Sofroniew and Vinters 2010, Pekny and Pekna 2014).

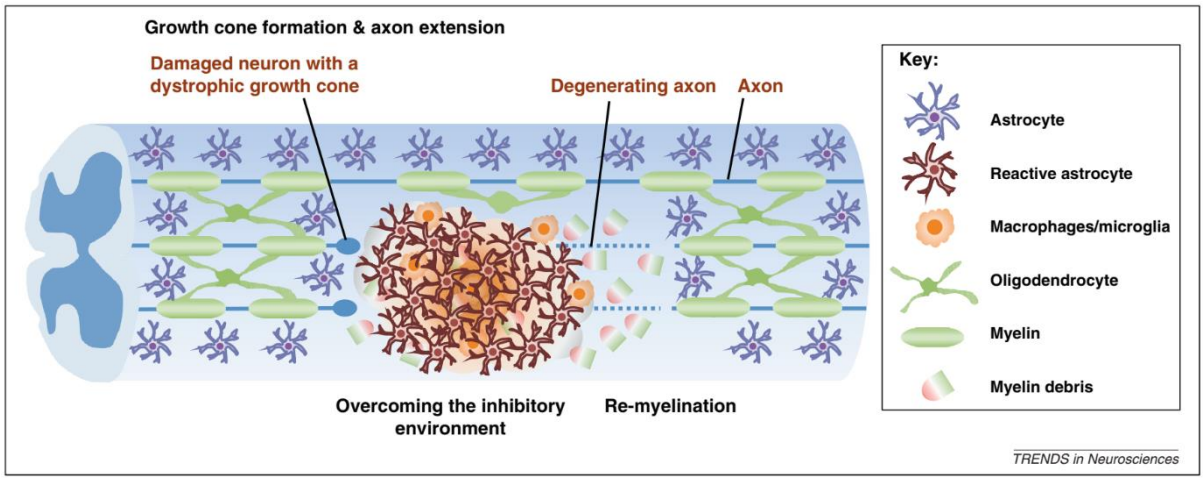

Figure 6: Glial scar formation and challenges for neuronal regeneration. Schematic overview of CNS tissue affected by a severe lesion. Neuronal transmission is disrupted by degenerating axons and dystrophic growth cones. Naive astrocytes in the surrounding tissue become reactive and migrate into the region of the injury where they proliferate and form the glial scar. Macrophages and microglia are recruited by reactive astrocytes to clean the extracellular space (modified from Hur, Saijilafu et al, 2012).

The induction of neuronal regeneration and reduction of regrowth inhibition is a topic of high relevance in the field of biomedicine, since injury to the CNS leads to permanent negative consequences for patients, for example paralysis in the case of spinal cord injury, as well as scarring in the brain as a result of neuronal or neurodegenerative disorders. For these reasons, many different avenues of therapy have been investigated. Some of these potential remedies include the stabilization of neuronal growth cones with tubulin stabilizers, modulation of the glial scar ECM and removal of inhibitory factors such as CPSGs. Additional, highly invasive therapeutic approaches include targeted gene therapy or microsurgery. Astrocytes have also been specifically targeted in neuronal regeneration for their role in glial scarring (Romero, Lin et al. 2007, Bradbury and Carter 2011, Hur, Saijilafu et al. 2012, Tedeschi and Bradke 2017). Consequently, the aim of modern therapies for patients with neurological disorders is to inhibit but not to completely ablate astrocytic reactivity and scar formation.

1.3 The cytoskeleton

As described above, changes in gravity conditions and as such in mechanical loading often have consequences also for cytoskeletal rearrangements. Thus, a major target for the current investigations were neuronal cytoskeletal structures and related functional mechanisms.

The cytoskeleton of a eukaryotic cell serves three major functions: first of all, intracellular localization of proteins, organelles and other contents of the cell has to be organized and the transport to different parts of the cell has to be facilitated. Secondly, the cytoskeleton anchors the cell to its growth substrate or inside of tissues or ECM in a physical and biochemical respect. The last major function of the cytoskeleton is to enable cellular movement and reshaping. All these functions are majorly dependent on microtubules, actin fibers,

intermediate filaments and their vast respective families of associated proteins (see Figure 7) (Fletcher and Mullins 2010).

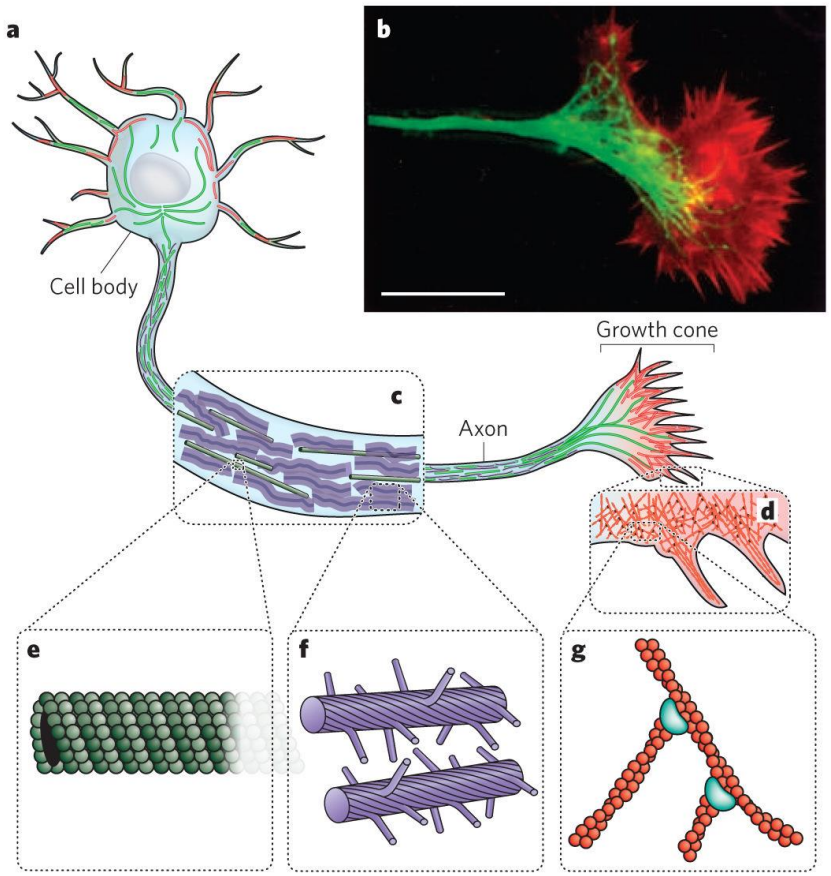

Figure 7: The three types of cytoskeletal networks. Depicted are microtubules (e), intermediate filaments (f) and actin fibers (g) and their rough intracellular localizations in a neuron (a). The axon contains microtubules and is stabilized by intermediate filaments (c), whereas newly forming cellular protrusions, in this case the growth cone (b) are actin rich since the actin cortex at the cell perimeter (d) forms actin fibers out of a dendritic network to create protrusions of the cellular membrane (modified from Fletcher and Mullins 2010).

1.3.1 Actin

The actin cytoskeleton relies on the dynamic polymerization and depolymerization of filamentous actin (F-actin) from single building blocks of globular actin (G-actin). G-actin monomers polymerize into a helical F-actin structure with a diameter of approximately 7 nm. These fibers steadily polymerize on the side of the so-called barbed end (or (+)-end) of the fiber by filament nuclei consisting of at least di- and trimers of ATP-bound G-actin. In contrast, the pointed end (or (-)-end) has a ten-times lower polymerization affinity resulting in highly polarized actin filaments (see Figure 8). This spontaneous F-actin polymerization is regulated by a huge variety of actin-binding proteins, e.g., profilins or cofilins, which either promote or inhibit actin proliferation (Thomas D. Pollard 1974, Gurniak, Perlas et al. 2005, Rotty and Bear 2014, Pollard 2016). The actin cytoskeleton is highly dynamic and forms superstructures that strongly differ in shape and function. Astrocytes are very reliant on the nominal functioning of their actin cytoskeleton since they need to spread their cell body thinly to connect to their surrounding neurons and synapses, and also to change their morphology and to migrate in case of reactive astrogliosis.

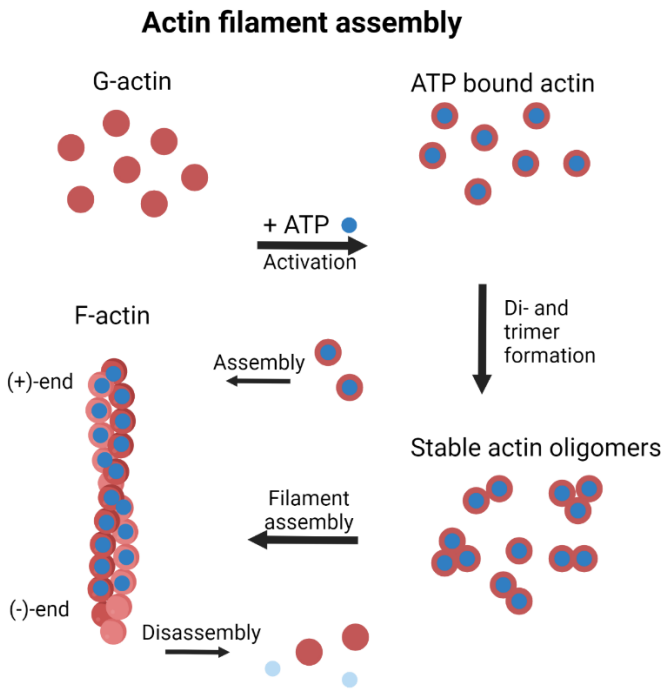

Figure 8: Actin filament assembly
Inside the cell, G-actin binds to cytosolic ATP, these activated G-actin monomers form di- and trimers which assemble on the (+)-end of F-actin. At the (-)-end of the actin filament G-actin is dephosphorylated and the ADP-bound monomers disassemble (created with Biorender).

One key player in the formation of dendritic F-actin networks is the group of actin-related proteins (e.g., the Arp2/3 complex) (Pollard 2016). The Arp proteins bind to the sides of actin fibers to form branching points and so to create a highly branched F-actin network. This network is typically found at the front of the cell near the actin cortex and is often visible in astrocytes *in vitro*. At this leading edge of a polarized cell, the Arp2/3 complex is responsible for the formation of lamellipodia and allows the cell to move forward in a crawling motion towards the leading edge. On the contrary, at the trailing edge of the cell, the F-actin network is disassembled by proteins of the ADF/cofilin family (Kovar, Harris et al. 2006). At the same time, bipolar filaments of the motor protein myosin II are responsible for retracting the cell rear by exerting contractile forces on anti-parallel actin fibers. The coordination of lamellipodial protrusion and trailing edge contraction and disassembly creates the actin treadmilling effect and a retrograde actin flow throughout the polarized cell, enabling cellular migration. When an actin fiber growth shall be stopped, it is capped by certain proteins that prevent G-actin from attaching to the barbed end of the fiber (Blanchoin, Boujemaa-Paterski et al. 2014). Filopodia represent another structure implicated in cell motility, but also responsible for cell-cell contacts, chemosensing of the cellular environment, and cell-cell signaling, all of which are important functions for astrocytes. These thin membrane protrusions are formed by parallel actin filaments in coordination with the Arp2/3 complex and formins (Vignjevic, Yarar et al. 2003). Other intracellular actin structures are actin bundles linked together by crosslinking proteins. These crosslinkers, for example filamin and fimbrin, can bind to and crosslink multiple actin fibers and create bundles of varying thickness, with the single fibers either being parallel (the (+)-ends of neighboring filaments are pointing in the same direction) or anti-parallel with the (+)-ends of neighboring filaments pointing in opposite directions.

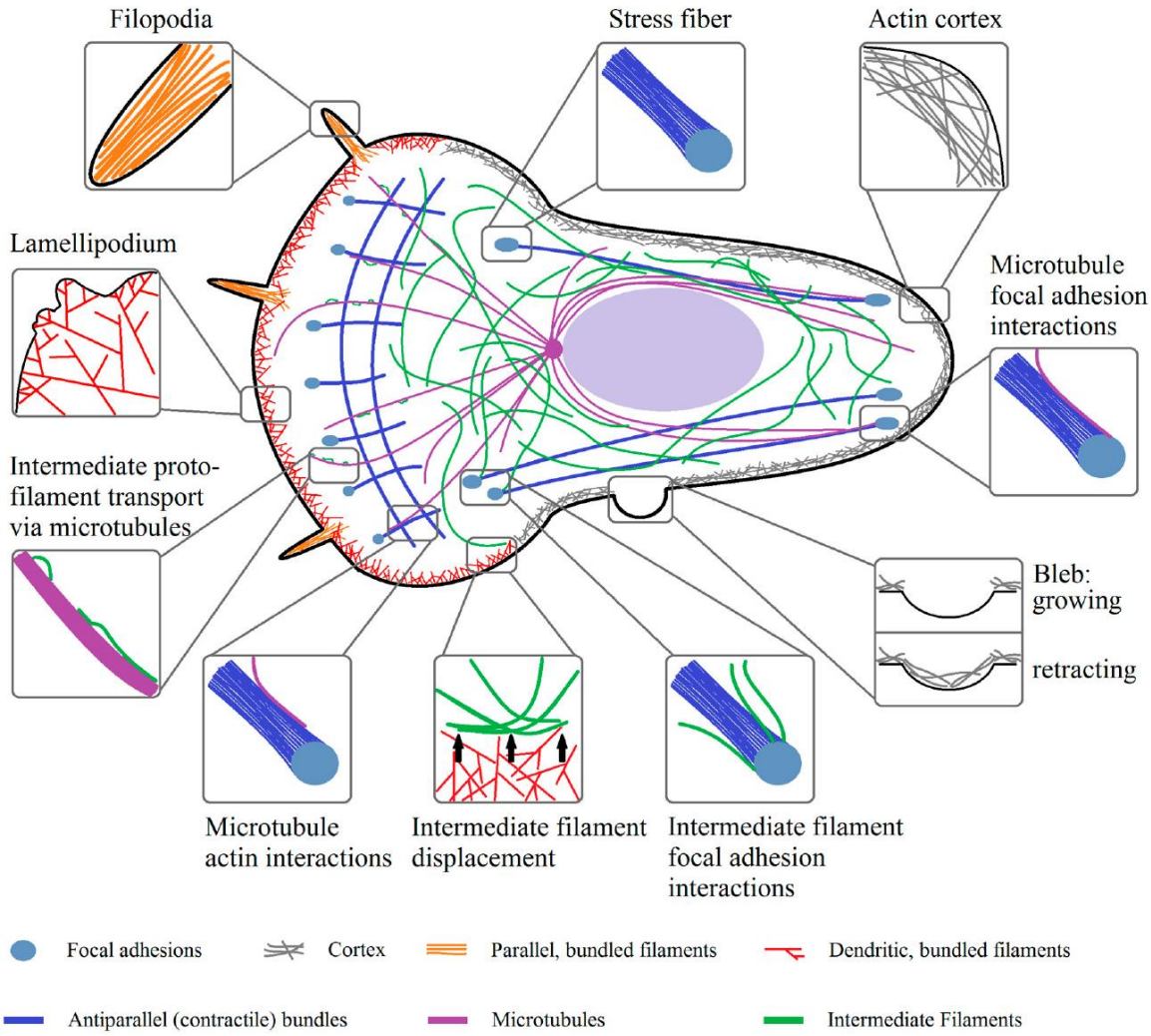

Figure 9: Cellular structures organized by actin, tubulin, and intermediate filaments The various cytoskeletal elements are interconnected and have many functions. Microtubules are used as ways of transport; actin filaments are forming membrane protrusions and stress fibers which connect to focal adhesions. Intermediate filaments are connected to focal adhesions and microtubules (modified from Hohmann and Deghani, 2019).

One type of anti-parallel structured actin-filament bundles are actin stress fibers (Naumanen 2008). Stress fibers consist of bundles of 10 – 30 actin filaments crosslinked by proteins such as α-actinin and are contractile due to myosin proteins. Stress fibers are the main load-bearing elements of the cell as well as responsible for cellular contractility. They link the cell to its substrate or ECM via focal adhesions, which are large protein assemblies connected to actin and intermediate filaments. Important focal adhesion proteins include several integrins as well as focal adhesion kinase (FAK) and vinculin (Naumanen 2008). Non-motile cells usually contain more, and thicker stress fibers compared to motile cells, which can also help to separate astrocytes. More specialized intracellular actin fibers are the transmembrane nuclear

actin-associated (TAN) lines which are traversing the nucleus from one end to the other and are connected to the nuclear envelope, but not to focal adhesions.

Another type of specialized actin structure are the perinuclear actin caps, which are longitudinal actin fibers connected to the nucleus and originating from focal adhesions (Davidson and Cadot 2021). These two types are regulating the nucleus shape and are also implicated in mechanosensing by transmitting mechanical forces affecting the cell into the nucleus, regulating gene expression.

Lastly, the actin cortex is situated at the cell membrane and forms a border region made up of crosslinked actin filaments and filament bundles. The tension of the cortical actin network regulates the cellular shape and its response to mechanical stimuli. It is also seen as a starting point for actin fiber polymerization in preparation for lamellipodia or filopodia extrusion (Fletcher and Mullins 2010, Hohmann and Dehghani 2019).

1.3.2 Tubulin

The tubulin cytoskeleton consists of microtubules. These hollow, helical structures are made up of α- and β-tubulin heterodimers and are 12 nm in diameter (Ohi and Zanic 2016). Microtubules are generally seeded by the microtubule organization center (MTOC) and are anchored there with their (-)-ends. GTP-bound tubulin heterodimers attach at the (+)-end of the microtubule to elongate it but can also rapidly disassemble at this end (see Figure 10). Thus, microtubules can either steadily elongate or rapidly disassemble, which is called dynamic instability of the microtubule cytoskeleton.

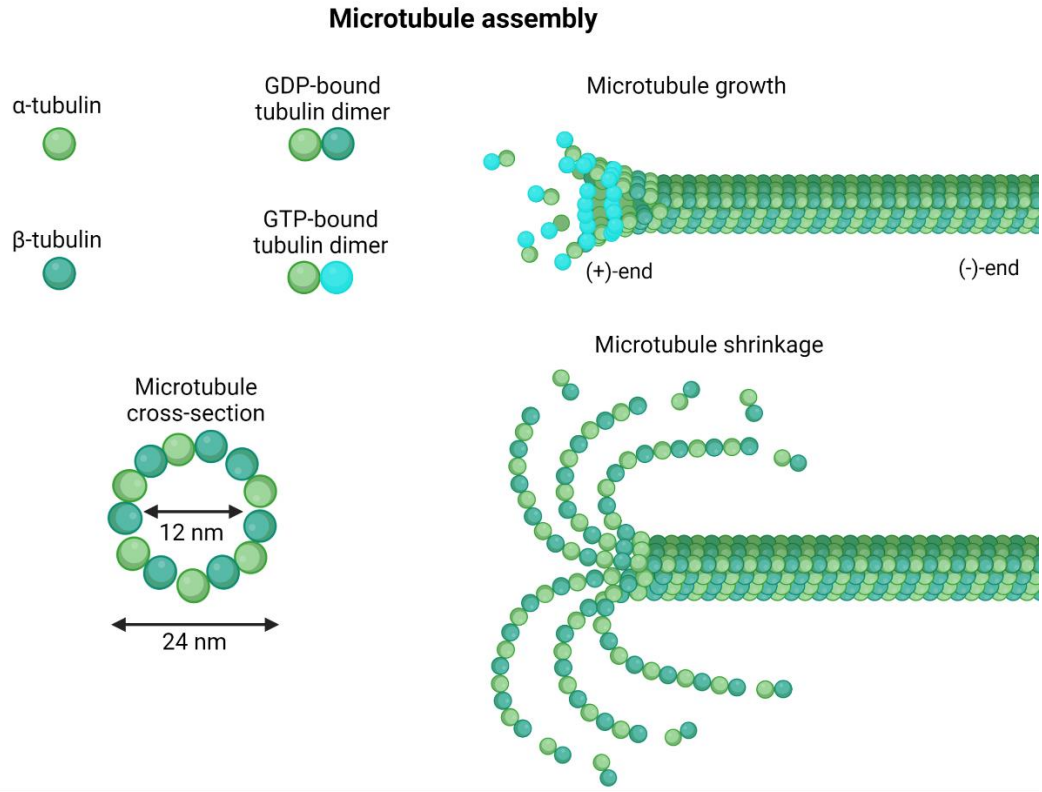

Figure 10: Microtubule assembly and disassembly. Microtubules are heterodimeric helices made from GTP bound α - and β -tubulin dimers. They elongate at the (+)-end but can also disassemble from this end when not enough GTP is bound anymore (created in Biorender).

Microtubule dynamics are regulated by microtubule interacting proteins which bind to the top a tubule to stabilize it, such as proteins of the cytoplasmic linker associated protein (CLASP) family (Nakamura 2001). Other proteins can sever microtubules, influence (de-)polymerization dynamics or interact with whole filaments to stabilize it, such as Tau and MAP2 (Komarova, De Groot et al. 2009). Motorproteins of the kinesin family are able to traverse the microtubule network and thus facilitate its main role as transport tracks for kinesin coupled vesicles and

organelles throughout the cell. For this reason, the microtubule network is usually most concentrated at the center of a cell near the nucleus, endoplasmatic reticulum and Golgi apparatus and thins out leading to the edges of a cell. Microtubule stability is an important factor in the growth and regeneration of dendrites, as microtubules leading into the axonal growth cone supply building blocks and are involved in path finding of the newly generated axon (Hur, Saijilafu et al. 2012). Another very important function of the microtubule cytoskeleton is the formation of the mitotic spindle. It is responsible for the separation of newly duplicated chromosomes in the course of cell division (Petry 2016). In general, the actin and tubulin networks are interacting at various points, for example focal adhesions, and actin fibers (see Figure 9). They are regulated by partly the same proteins and are connected physically in some regions (Erturk, Hellal et al. 2007, Fletcher and Mullins 2010, Hohmann and Dehghani 2019). In astrocytes specifically, the tubulin cytoskeleton is loosely packed during development, but densely developed in matured cells. Microtubules extend throughout astrocyte main processes *in vivo* but not into the finest intercellular connections, tubulin co-locates with intermediate filaments such as GFAP. Interestingly, microtubules are observed to reach the furthest tip of polarized reactive astrocyte processes, in contrast to membrane protrusions such as lamellipodia or filopodia in other cells (Schiweck, Eickholt et al. 2018).

1.3.3 Intermediate filaments

Intermediate filaments are a group of filament-forming proteins that encompasses several different types of proteins. It can be subdivided into five classes, the first four of those encoding cytoplasmic filaments and the fifth class generating the nuclear filaments called lamins. Type I and II intermediate filaments include different kinds of keratins (Moll, Divo et al. 2008). Type III filaments are vimentin, desmin, peripherin or GFAP. Vimentin and GFAP are expressed in astrocytes, while desmin is expressed mainly in muscle cells. The fourth class of intermediate filaments are the neuronal filaments internexin, synemin and nestin. The last of which is also expressed in astrocyte progenitors but not in mature cells (Schiweck, Eickholt et al. 2018). The superstructure formed from single intermediate filaments is a coiled-coil structure formed from two monomeric, polarized helices. Two of these coiled coils associate antiparallel in regards to the polarity of the single helices, with eight such structures completing one unit length filament. Several of these unit lengths can then form the final filament via end-to-end aggregation.

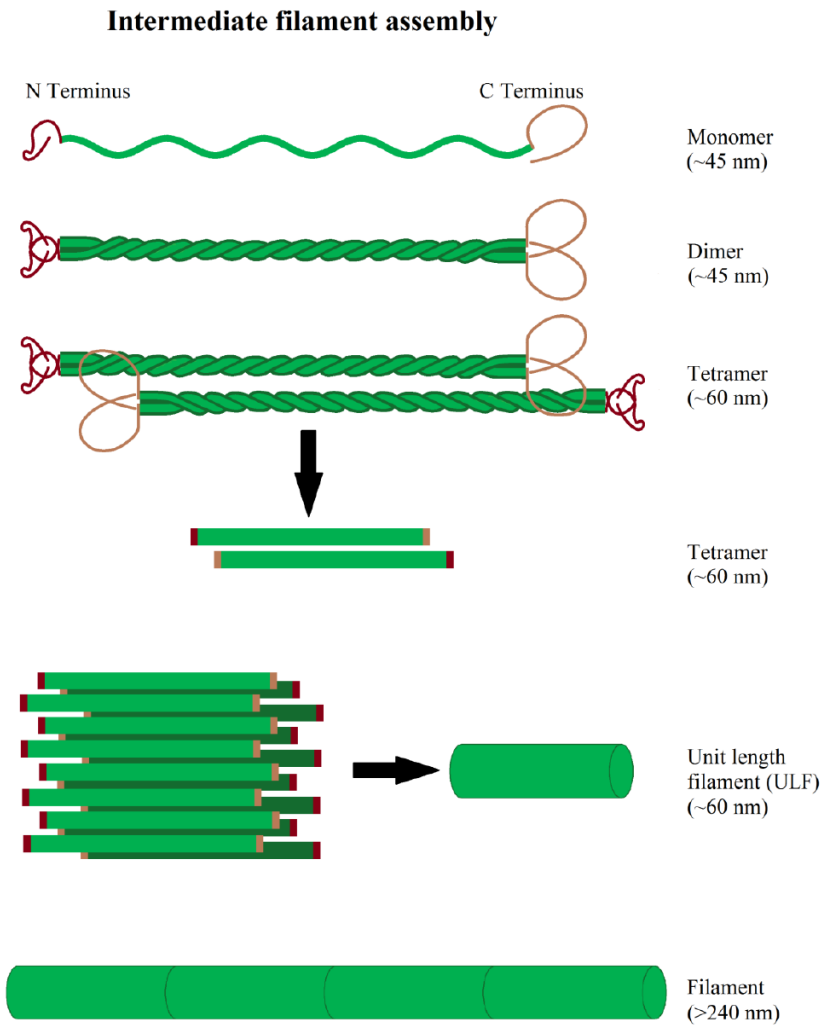

Figure 11: Intermediate filament assembly. Monofilaments form dimers, which in turn aggregate into a tetramer. Four tetramers combine into a unit length filament and several unit length filaments form a filament (modified from Hohmann and Dehghani 2019).

Intermediate filaments form a network which is similarly to tubulin focused in the perinuclear space but also extends up to the cell perimeter. Intermediate filaments can interact with focal adhesions and desmosomes to uphold cellular integrity and also organize the location of and scaffold mitochondria, Golgi and other organelles. Generally, the functions of intermediate filaments are manifold and dependent on the specific cell type they are expressed in. GFAP in astrocytes is connected to reactivity and cell motility and expressed in the main processes of the cells but not into the finest ones (see Figure 4A) (Schiweck, Eickholt et al. 2018, Hohmann and Dehghani 2019). In the human genome, ten different GFAP isoforms have been identified. These isoforms are known to be expressed in different astrocyte subpopulations (Middeldorp and Hol 2011). The two main GFAP isoforms are GFAPα and GFAPδ and control the intermediate filament network dynamics, although it is still to be discovered if the single isoforms have specific effects on the intermediate filament network (Moeton, Stassen et al. 2016).

1.3.4 The cytoskeleton and cell migration

As already mentioned, cellular migration relies on the collaboration of many cytoskeletal elements and is essential for reactive astrogliosis and the formation of the glial scar. Actin is the main player in mesenchymal cell migration since the lamellipodium which signifies the forward region of a polarized migrating cell is protruded through actin fibers formed from a dendritic network constructed by Arp2/3 and WAVE. At the trailing end of the cell, actin stress fibers contract with the help of myosin and actin fibers are disassembled by profilin, creating the actin treadmilling effect. Focal adhesions play a big part in cellular migration because they anchor the cell to its substrate via stress fibers. New focal adhesions have to be formed at the lamellipodium to keep the cell in place and prevent a retraction from the tension of the actin cortex. At the trailing end of a cell, focal adhesions must be depolymerized and uncoupled from the cytoskeleton to allow retraction of the cell membrane. The family of Rho GTPases are key players in the regulation of cellular migration. Rac1 is essential for the formation of the lamellipodium as it activates the Arp2/3 complex via Scar/WAVE (Krause and Gautreau 2014). Rac1 is also implicated in the formation of nascent adhesion in the newly formed lamellipodium and in the crosstalk between actin cortex and tubulin network Rac1 together with RhoA stabilize microtubuli (Wittmann, Bokoch et al. 2003). RhoA additionally participates in stress fiber formation and the maturation of newly formed nascent focal adhesions at the leading edge of a cell (Pellegrin and Mellor 2007). A too high activation of RhoA inhibits cell migration because the high amount of stress fibers are formed, leading to an increase in contractility of the cell (Cheng, Castillo et al. 2016).

Located shortly behind the leading edge of the lamellipodium are extensions of the tubulin cytoskeleton. These serve mainly as tracks to supply the actin cortex with building blocks such

as membrane components, Rho GTPases and associated molecules and intermediate filaments. Thus, proper function of the tubulin cytoskeleton is necessary for cellular migration (Miller, Folkmann et al. 2009). At the leading edge of a cell, microtubules connect with nascent focal adhesions and supply integrins their maturation (Gu, Noss et al. 2011).

The role of intermediate filaments in cell motility is different depending on the cell type and expressed IFs. It is generally established that also IFs are needed for nominal migration, since they influence the cell-matrix adhesion. Ablation of vimentin led to the inhibition of cell migration (Battaglia, Delic et al. 2018). Specific for astrocytes, GFAP has also been shown to be crucial for astrocytic migration and its ablation inhibited cellular motility (Pekny, Johansson et al. 1999, Zhan, Gao et al. 2017). A confounding observation for this is, that GFAP is upregulated in reactive astrocytes which are also at the same time acquiring cell motility to migrate into an injured CNS region (Pekny and Pekna 2014).

1.3.5 Rho GTPases

The family of Rho (Ras homologue) GTPases consists of 20 members and is part of the Ras superfamily. In general, Rho GTPases control cytoskeletal dynamics and cell adhesion and thus are important players in cellular migration, polarity, and cell cycle progression (Madaule 1985, Hodge and Ridley 2016). As other GTPases, the Rho family proteins exist in an active, GTP-bound and an inactive, GDP-bound state. These states can be regulated by guanine nucleotide exchange factors (GEFs) which catalyze the switch from GDP to GTP and thus activate the GTPase. Additionally, GTPase-activating molecules (GAPs) increase the GTPases GTP hydrolysis rate and so inactivate it. The last group of regulating molecules are the guanine nucleotide dissociation inhibitors (GDIs) which inhibit Rho signaling by preventing GTPase membrane localization. Rho GTPases are activated by many different cell-surface receptors such as cadherins, integrins and G-protein coupled receptors (Hodge and Ridley 2016).

RhoA activation is involved in cytoskeletal dynamics and cell migration by facilitating actin stress fiber formation via ROCK (Burridge and Guilluy 2016). These stress fibers are needed for cellular contractility and to anchor the cell to its substrate with focal adhesions and activated RhoA leads to increased cellular contractility via myosin activation. RhoA is also responsible for the maturation of nascent focal adhesions in newly formed lamellipodia (Pellegrin and Mellor 2007). For the formation of lamellipodia the Rho GTPase Rac1 is needed since it activates the WAVE complex which leads to Arp2/3 activation (Krause and Gautreau 2014). Another involvement in cell migration by Rac1 is the formation of nascent adhesions in the lamellipodium (Ridley 2011). Rho GTPases are not only involved in actin cytoskeleton dynamics but also in the tubulin cytoskeleton. RhoA can stabilize microtubules via its effector mDia (Morris, Nader et al. 2014), and Rac1 together with the Rho GTPase Cdc42 can stabilize

microtubule (+)-ends (Fukata and Perez 2002). Cdc42 is furthermore needed for the protrusion of filopodia (Block, Breitsprecher et al. 2012). Cdc42 and Rac1 are activated by RhoG, which leads to the formation of membrane ruffles, lamellipodia, and filopodia (Cecile Gauthier-Rouviere 1998).

1.4 Aim of this thesis

So far, the effects of hypergravity and microgravity and thus altered mechanical loading on morphology, behavior and reactivity of astrocytes had not been investigated. This glial cell type plays an important role in brain health and function and is also implicated in CNS disease response and complication through astrocyte reactivity. This is characterized by astrocytic hypertrophy, hyperproliferation and migration which, *in vivo*, results in astrogliosis. The response of primary astrocytes to altered gravity conditions will provide fundamental knowledge whether and how environmental stimuli trigger their (re-)activity. This in turn might in the future bear new avenues of research for manned space flight as well as developing therapies for patients with neurological disorders.

In this thesis primary murine cortical astrocytes are employed as a physiologically relevant model system of astrocyte response to altered gravity, in normal gravity (1*g*), in 2*g* hypergravity as a physiological level of hypergravity which can also be tolerated by mice and humans, and simulated microgravity using the principle of 2D clinorotation.

Parameters of cellular morphology, such as cell size, circularity, Feret measurements and nucleus count and morphology are analyzed using epifluorescence microscopy. Since gravity impacts the cytoskeleton in other cell types, super resolution STED microscopy as well as live cell imaging is employed to investigate cytoskeletal rearrangements of astrocytes during and after hypergravity exposure. The cytoskeleton is not only involved in cellular morphology but also in cellular behaviors such as spreading and migration. To image the effects of hypergravity exposure on dynamic cell movements, live-cell imaging of spreading cells and scratch assays under hypergravity are used. Astrocyte reactivity, which occurs during injury or illness of the CNS is measured by fluorescence quantification of associated proteins to investigate to which extent astrocyte reactivity can be modulated by altered gravity. To verify that altered gravity does not influence cell viability, proliferation and apoptosis assays will be performed on cells exposed to 2*g* hypergravity, simulated microgravity, and 1*g* - controls.

Dynamic changes of the actin cytoskeleton caused by hypergravity exposure is observed using the transgenic LifeAct-GFP mouse line in live-cell imaging under hypergravity.

To validate the observed reactions to altered gravity on a biochemical level, and to assess the underlying mechanisms, Western blotting of marker proteins relevant for reactivity, migration, and cytoskeletal processes after hypergravity exposure are performed.

1.5 Publications resulting from this work

Significant parts of this thesis have been submitted as research articles.

A journal article titled “Hypergravity Attenuates Reactivity in Primary Murine Astrocytes” was published in August 2022 (Lichterfeld, Kalinski et al. 2022).

The following data produced in this thesis was published in this publication:

- 2.1 Astrocyte initial spreading and long-term hypergravity exposure data including morphological parameters
- 2.2 GFAP count and reactivity marker fluorescence quantification
- 2.3 Nuclear morphology analysis
- 2.4 Astrocyte migration under hypergravity, long-term and live-cell imaging
- 2.5 Super resolution microscopy of the cytoskeleton
- 2.6 LifeAct-GFP astrocyte live-cell microscopy under hypergravity
- 2.7 GFAP, Vimentin, and FAK western blot data

A second manuscript is in preparation. It will contain the following data from this thesis:

- 2.8.1 Astrocyte spreading under simulated microgravity
- 2.8.2 Morphology parameters of astrocytes exposed to simulated microgravity
- 2.8.3 Circularity changes of astrocytes in simulated microgravity
- 2.8.4 Proliferation data of astrocytes in simulated microgravity
- 2.8.5 GFAP expression in astrocytes exposed to simulated microgravity

2. Results

2.1 Morphological features and dynamics related to reactive astrogliosis are influenced by hypergravity

Cellular two-dimensional morphology can be used as a readout for various characteristics of a cell *in vitro* and apply it to investigations *in vivo*. Amongst others, cell viability can be investigated regarding e.g. cell spreading or apoptotic blebbing, as well as cellular behavior such as the directional migration. Impacts on cytoskeletal load bearing or force-transducing elements can be inferred from morphological observations. Cell morphology, behavior and cytoskeletal elements are known to be affected by altered gravity exposure. Additionally, reactive astrocytes forming the glial scar undergo morphological changes after injury that can be measured and used as an *in vitro* marker to assess the reactive state of cultured astrocytes.

2.1.1 Astrocyte spreading is impacted by hypergravity exposure

Astrocyte morphology *in vivo* is characterized as star-shaped with a central soma with many branched and elongated processes. In cell culture, astrocytes have a contrasting and less stellate appearance. After seeding the cells onto a growth substrate, the globular astrocytes quickly adhere to the surface and start to flatten, maximizing the contact area. This so-called cell spreading is a widely seen process in astrocyte primary cell culture. Cell spreading is, like all alterations in cell shape, dependent on the coordinated action of different cytoskeletal elements. Filamentous actin (F-actin) must be assembled from globular actin (G-actin) which is localized throughout the cytoplasm. Coordinated actin fiber assembly at the cell perimeter then leads to the protrusion of the cell membrane and thus the enlargement of the cell body at the respective side. This is the prerequisite transformation to induce cell migration e.g. in response to reactive astrogliosis. This process is regulated by several mechanisms such as actin-associated motorproteins, Rho GTPases and focal adhesion related proteins.

In case of a CNS injury *in vivo,* reactive astrocytes which have migrated into the region of the injury and have proliferated also show this a spreading-like increase in surface area in order to release ECM-related proteins and to form the glial scar tissue.

Cell spreading can be measured by analyzing fluorescence microscopy images of cells in which actin is co-stained with a fluorophore-conjugated phalloidin. The cell perimeter can be easily discerned in the corresponding fluorescence channel and by using the Zeiss Zen image analysis module the size of each single cell can be measured and later analyzed. For live-cell microscopy it is also possible to analyze cell size using polarized light DIC microscopy where the cell perimeter is easily discernible.

Because of the well-established readout and analysis combined with a great relevance for processes related to cytoskeleton dynamics and astrocyte reactivity, cell spreading was one of the first parameters to be analyzed in astrocytes exposed to altered gravity conditions.

2.1.1.1 Initial astrocyte spreading is impaired by hypergravity

By employing the Hyperscope (see 1.1, Figure 2), the initial spreading of astrocytes was imaged in real-time under normal gravity and hypergravity conditions. Primary astrocytes were seeded into Ibidi µ-Slide wells. The cells' adherence to the surface and initial spreading was then imaged in 30-minute intervals for a total of five hours. The experiment was repeated three times with independent primary cultures derived from individual mice at 2*g* and as a control the same protocol was performed in 1*g* with cells from the same respective culture on the Hyperscope on the same day.

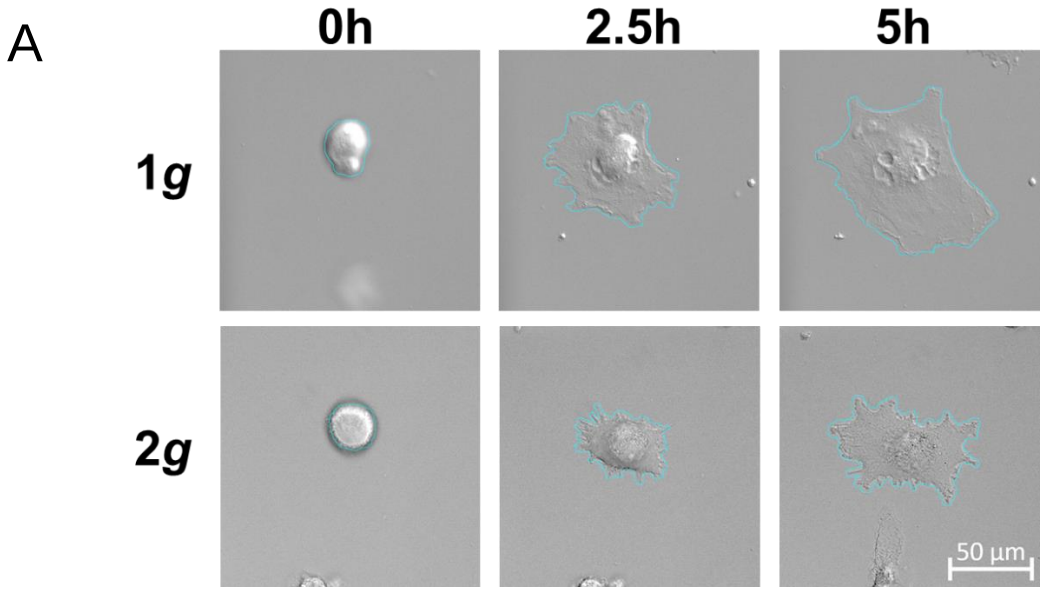

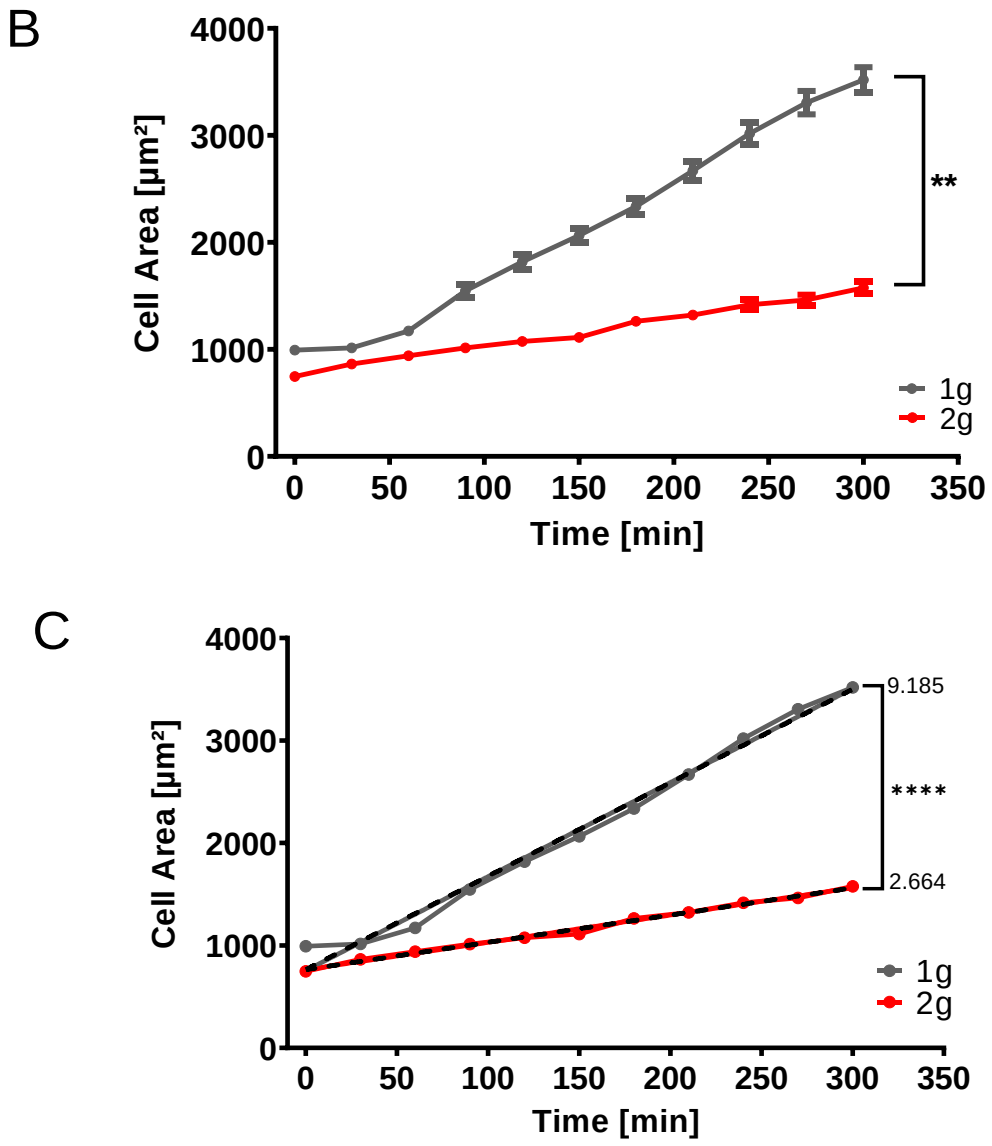

Figure 12: Initial spreading of astrocytes in normal and hypergravity.
(A) DIC microscopy images of freshly seeded astrocytes at 0h, 2.5h and 5h after seeding. Top row shows the 1*g* control cells, bottom row shows cells which were exposed to 2*g* hypergravity on the Hyperscope. Cells which were adhering and spreading in hypergravity conditions appeared to have a smaller cell area compared to the control cells. **(B)** Initial spreading of primary astrocytes. Shown is the average cell area with SEM in µm² of astrocytes in 2*g* hypergravity (red) vs. 1*g* control (grey). Cells exposed to hypergravity exhibit a slower increase in their average cell area. After five hours the 1*g* control cells had an average cell size of 3517 µm² ± 119 µm² vs. 1576 µm² ± 57 µm² for the 2*g* sample. Mann-Whitney test (p=0.0083). **(C)** Linear regression of initial astrocyte spreading. The regression line of the 1*g* condition has a slope of 9.185 and the 2*g* curve has a slope of 2.664. The sample size n is (1*g*=136; 2*g*=131) cells from 3 individual astrocyte cultures derived from 3 gravid mice. Scale bar represents 50 µm.

The freshly seeded astrocytes appeared as globular cells while in suspension, which could be observed slightly out of focus since the surface of the slide was set to be the focus reference (see Figure 12A). After adhering to the substrate, astrocytes instantly began to spread and the cell perimeter including fine details such as filopodia could be discerned using live DIC microscopy. Single cells that started to adhere to the surface in the first 30 minutes were

selected for image analysis using Zeiss Zen. Here the time-lapse videos consisting of 11 frames each were analyzed with regard to cell area and plotted in GraphPad Prism for statistical analysis.

The initial spreading dynamics of astrocytes in hypergravity versus 1*g* controls became visible when depicting the area of each analyzed cell per time point on an XY graph (see Figure 12B). For the first hour, samples in both conditions only slowly increased in average cell area. Following the 1h mark, the control cells started to show an increased spreading rate and the two curves for the respective spreading rates at 1*g* and 2*g* diverged. Over the observed five hours the control cells had an increase in average cell area of 255% from 992 µm² ± 33 µm² to 3517 µm² ± 119 µm² whereas the astrocytes exposed to hypergravity only increased their cell area by 111% from 747 µm² ± 26 µm² to 1576 µm² ± 57 µm². At the end point of the experiment at five hours, spreading astrocytes exposed to hypergravity were by average 45% smaller than the 1*g* control cells. This significant decrease in initial spreading was also confirmed by a Mann-Whitney test with a statistical significance of $p= 0.0083$.

The slopes of the linear regression lines were 9.185 for the 1*g* samples and 2.664 for the 2*g* samples (see Figure 12C). The slopes of the two regression lines differed significantly ($p < 0.001$) following a lag phase of approximately 1h, and thus indicated a measurable difference in initial spreading speed between the two groups.

2.1.1.2 Astrocyte spreading reduced after one and two days of hypergravity exposure

Since the initial spreading of astrocytes was markedly reduced by 2*g* hypergravity (see 2.1.1.1 Figure 12), the next step was to verify whether long-term effects would arise after several days of hypergravity exposure. For this, primary astrocytes were seeded on coverslips and then exposed in the MuSIC incubator-centrifuge to 2*g* hypergravity for one and two days. Directly after exposure the cells were fixed with 4% PFA and the cell outline was visualized by staining F-actin using fluorophore-conjugated Phalloidin. The general astrocytic marker GFAP was immune-labeled confirm the purity of the astrocyte culture. The coverslips were subsequently scanned on an epifluorescence microscope and analyzed using Zeiss Zen. The experiment was repeated three times with independent primary cultures and compared to identically treated control cells kept at normal gravity.

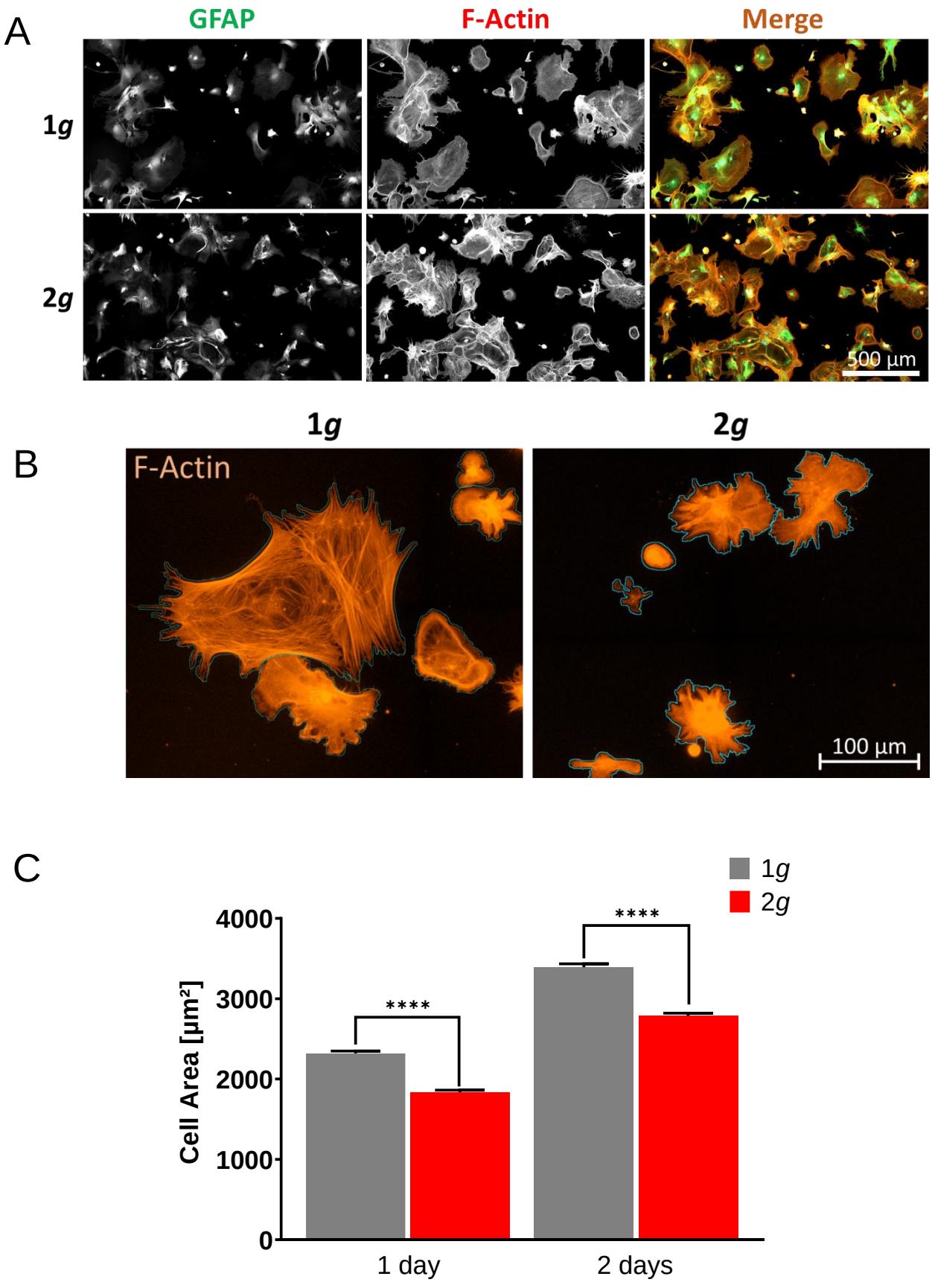

Figure 13: Astrocyte spreading is reduced after one and two days hypergravity exposure. (A) Exemplary immunofluorescence image of astrocytes stained with Phalloidin to visualize F-actin (red) and an anti-GFAP antibody (green). The 1*g* control is depicted in the top row and the 2*g* hypergravity

sample in the bottom row. The samples were exposed for 24h. **(B)** Astrocytes of the 1*g* control sample and after one day of 2*g* hypergravity exposure with fluorescently labeled F-actin (red). The cell perimeter as recognized by semi-automatic Zeiss Zen image analysis is marked (blue). **(C)** Average cell area in µm² and SEM of astrocytes in the 1*g* control group after one day (grey, 2320 µm² ± 29 µm²) and after one day of 2*g* hypergravity exposure (red, 1839 µm² ± 22 µm², $p < 0.0001$). Same analysis after two days of 1*g* control (3392 µm² ± 43 µm²) and 2*g* hypergravity exposure (2785 µm² ± 34 µm², $p < 0.0001$). The samples were compared via t-test. Sample size n is 1 day: 1*g*=2320; 2*g*=2218; 2 days: 1*g*=2572; 2*g*=2491 cells from 3 individual astrocyte cultures derived from 3 gravid mice. Scale bar represents 100µm.

Astrocytes exposed to 2*g* hypergravity exhibited no obvious disturbances due to mild hypergravity of 2*g* (see Figure 13A). The cells showed a ubiquitous baseline GFAP fluorescence under normal and hypergravity. Over the course of two days at constant 2*g* hypergravity, astrocytes exhibited visibly smaller cell surfaces (see Figure 13B). Statistical analysis (see Figure 13C) revealed a significant decrease in cell area of 21% in astrocytes exposed to 2*g* hypergravity for one day compared to a 1*g* control (1839 µm² ± 22 µm² vs. 2320 µm² ± 30 µm²). After two days of hypergravity exposure, the cells exhibited a significantly decreased cell area with a reduction of 18% compared to the 1*g* control (2785 µm² ± 34 µm² vs. 3392 µm² ± 43 µm²). The average cell area of the 1*g* control cells increased by an average of 46% during the investigated time frame of 24h, whereas the 2*g* hypergravity sample area displayed an increase of on average 50% over the same time.

2.1.1.3 Hypergravity exposure induces decreased cell polarity in correlation with cell size

To quantify and interpret the two-dimensional morphology and geometry of astrocytes, several measurement parameters can be used. Commonly used parameters are the Feret minimum and maximum diameters as well as the Feret ratio (see Figure 14A, B, C).

Within the cell outline in 2D as detected semi-automatically by Zeiss Zen, the program places two straight lines on opposite sides of the detected cell area and measures their distance. These straight lines are then rotated in 32 angle positions. The shortest measured distance is the Feret minimum (see Figure 14D, bright blue line). The Feret maximum is the longest of such distances, respectively (see Figure 14C, bright blue line). The Feret ratio is calculated from $\frac{FeretMin}{FeretMax}$.

With increasing cell size, the Feret minimum and maximum will also increase, whereas if a cell is roundish, the Feret ratio will approach 1 (Feret minimum and maximum are similar). If a cell is more polarized or elongated, the Feret ratio will approach 0 (Feret minimum and maximum become increasingly dissimilar). Using the Feret ratio in particular, one can make assertions about cellular behavior. Cells with a low Feret ratio have an elongated shape which might be caused by stellation processes or lamellipodial protrusion during cell migration. Depending on the cell type, a low Feret ratio can also be an indicator for cellular polarity. In

the case of astrocyte reactivity, a decreasing Feret ratio could indicate a pronounced migratory behavior, as the cells would exhibit *in vivo* to migrate to injured tissue in the CNS.

Astrocytes exposed to 2*g* hypergravity for one and two days before fixation were analyzed with regards to their Feret values and compared to 1*g* controls based on fluorescence staining of the cell outline (Phalloidin-labelled F-actin filament networks).

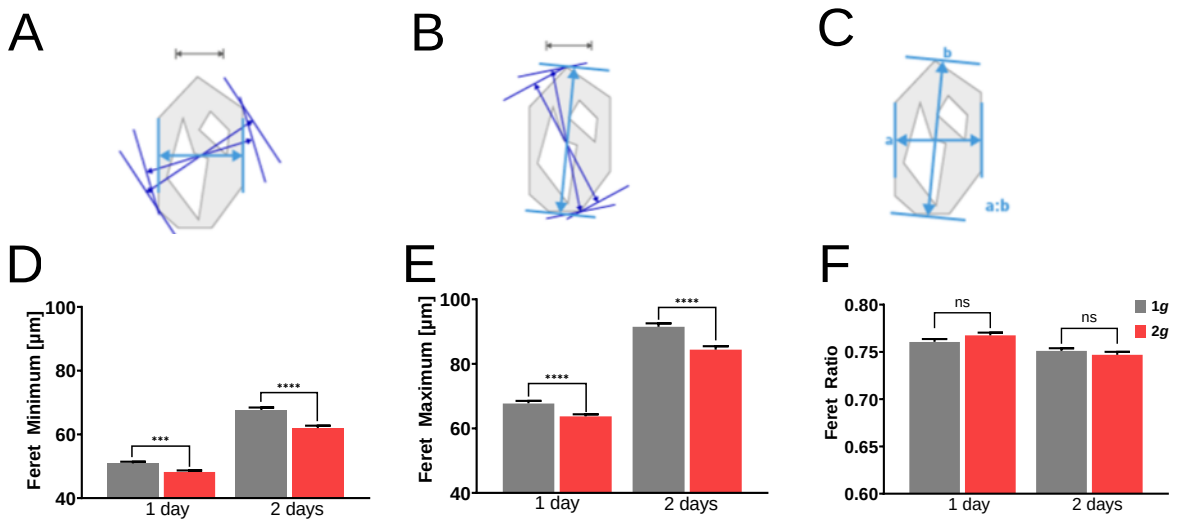

Figure 14: Feret ratio, minimum and maximum of astrocytes after one and two days of hypergravity (2*g*) exposure. Schemes of the **(A)** Feret minimum **(B)** Feret maximum and **(C)** Feret ratio of a cell. **(D)** Mean Feret minimum with SEM after 1 day of 1*g* control cells (grey, 50.89 µm ± 0.54 µm) and of 2*g* hypergravity exposed cells (red, 48.22 µm ± 0.47 µm, p = 0.0002) and after 2 days of 1*g* control (grey, 67.66 µm ± 0.78 µm) and the 2*g* sample (red, 62.00 µm ± 0.74 µm, p <0.0001,). **(E)** Mean Feret maximum after 1 day of 1*g* control (grey, 67.77 µm ± 0.76 µm) and 2*g* hypergravity sample (red, 63.73 µm ± 0.64 µm, p <0.0001), and after 2 days 1*g* control (grey, 91.49 µm ± 1.06 µm) and 2*g* exposure (red, 84.40 µm ± 1.05 µm, p <0.0001). **(F)** Mean Feret ratio with SEM after 1 day of 1*g* control cells (grey, 0.76 ± 0.01) and 2*g* hypergravity exposure (red, 0.77 ± 0.01, p = 0.0977), and after 2 days of 1*g* control (grey, 0.75 ± 0.01) and 2*g* hypergravity exposure (red, 0.75 ± 0.01, p = 0.3219). Sample size n is 1 day: 1*g*=2320; 2*g*=2218; 2 days: 1*g*=2572; 2*g*=2491 cells from 3 individual astrocyte cultures derived from 3 gravid mice.

When comparing the Feret values of astrocytes exposed to 2*g* hypergravity to 1*g* control conditions, it became apparent, that after one and two days, the Feret minima and maxima of the control cells were significantly higher than the values of the 2*g* exposed cells (see Figure 14D, E). This general decrease of Feret minima and maxima did not translate to the Feret ratio, as no significant changes between the hypergravity and control samples were observed at any time point (see Figure 14F). The Feret minima and maxima in both conditions increased on average between 29% and 35% (1 day: 1*g*: 0.7607 ± 0.0029, 2*g*: 0.7675 ± 0.0029; 2 days: 1*g*: 0.7511 ± 0.0028, 2*g*: 0.7470 ± 0.0031) during the course of the measurements. The Feret ratios decreased marginally and insignificantly from one day to two days.

2.1.1.4 Hypergravity exposure affects astrocyte circularity

Upon induction of astrocyte reactivity, the cells become increasingly stellar, thus another important parameter related to the morphological alterations of cell shape is the circularity. It is calculated by the Zeiss Zen image analysis program from the cell area and Feret maximum according to the formula: $\sqrt{\frac{4 * Area}{\pi * Feret\ Max^2}}$

A perfectly round cell or a circle would have a circularity of 1 whereas more elongated or coarse shapes will have a decreasing circularity approaching 0.

In a biological context, the circularity of single cells can provide information about the polarity and/or behavior of a cell. Cells that are polarized or migrating will have a comparably lower circularity, as for cell migration protrusions need to be formed, e.g. by formation of a lamellipodium. Thus, in order to start migrating, the cells elongate in a one-sided polar fashion, hence decreasing their circularity. Determining circularity values is superior to the Feret ratio measurement in that it also considers cells which have a highly serrated boundary stemming from filopodia or the formation of other cellular processes. Here, the Feret minimum and maximum would be similar and thus the cell would have a high Feret ratio, but a lower circularity compared to a cell with a smoother cell boundary.

For the analysis of cell circularity, the same samples as in paragraph 2.1.1.2 were used.

Astrocytes were exposed to 2*g* hypergravity for one and two days were compared with control cells that were cultured at 1*g* and immunostained for F-actin structures.

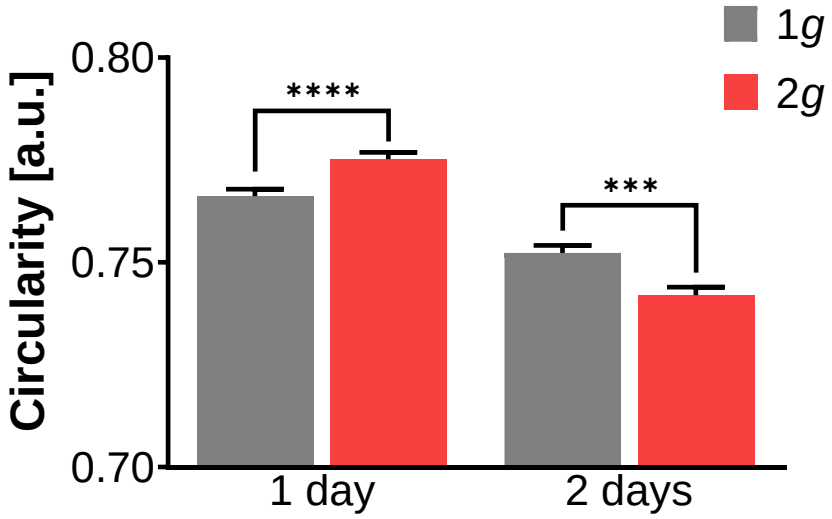

Figure 15: Astrocyte circularity in hypergravity. Mean circularity with SEM of astrocytes in the 1*g* control group (grey, 0.77 ± 0.01) and cells exposed to 2*g* hypergravity for one day (red, 0.78 ± 0.01, $p < 0.0001$) and two days in 1*g* (0.75 ± 0.01) and 2*g* hypergravity (0.74 ± 0.01, $p = 0.0001$). Sample size n is 1 day: 1*g*=2320; 2*g*=2218; 2 days: 1*g*=2572; 2*g*=2491 cells from 3 individual astrocyte cultures derived from 3 gravid mice.

After one day of hypergravity exposure, a small but significant increase in circularity by 1.3% could be measured in the hypergravity sample compared to a 1*g* control (see Figure 15).

Similar measurements after two days of 2*g* exposure showed a 1.1% decrease in circularity, compared with the time-matched 1*g* control samples. During the course of 24h from the first and second day of measurement, cell circularity decreased more pronounced in the hypergravity sample (0.78 ± 0.01 -> 0.74 ± 0.01, 5.4% reduction) then in the control sample (0.77 ± 0.01 -> 0.75 ± 0.01, 2.7% reduction).

2.1.1.5 Changes in astrocyte spreading are not influenced by altered proliferation or viability under hypergravity

A decrease in cell size (see 2.1.1.2) or defects in initial cell spreading (see 2.1.1.1) in primary murine astrocytes are hypothesized to be a phenotype of hypergravity exposure possibly related to astrocytic reactivity. Since these changes in cell behavior and morphology could also be indicators for a decrease in cell viability or an increase in proliferation, astrocyte cultures were analyzed for these properties. To verify that hypergravity exposure does not have cytotoxic or tumorigenic properties, primary murine astrocytes were cultured for several days in 2*g* hypergravity as well as 1*g* control conditions. In six-hour intervals, an Annexin V / propidium iodide (AV / PI) assay was conducted to measure apoptosis and necrosis in the samples (see Figure 16), as well as a Ki67-immunofluorescence staining to measure cell proliferation (see Figure 17).

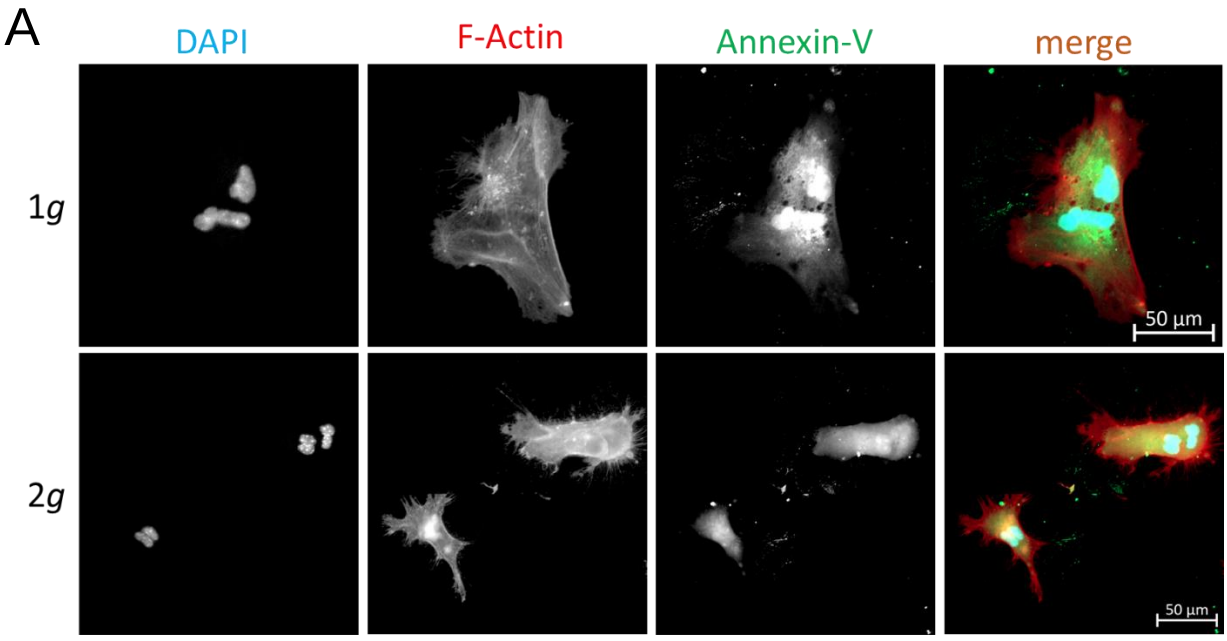

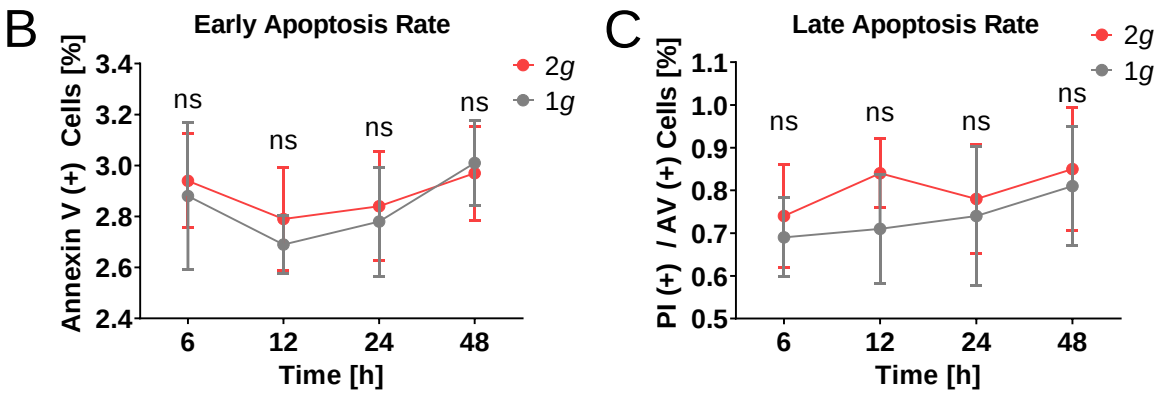

Figure 16: Apoptosis and necrosis of astrocytes over two days hypergravity exposure. (A) Exemplary immunofluorescence image of astrocytes stained with DAPI and Annexin V (AV), as well as fluorescently conjugated Phalloidin as a control staining. The 1*g* control is depicted in the top row and the 2*g* hypergravity sample in the bottom row. **(B)** Percentage of Annexin V-positive cells (± SEM) and propidium iodide (PI)-negative cells obtained by immunofluorescence apoptosis assay. Astrocytes were exposed to 2*g* hypergravity (red) for two days and the number of apoptotic Annexin V positive cells with SEM was counted and compared to 1*g* controls (grey) after 6, 12, 24, and 48 hours of exposure. **(C)** Similarly, astrocytes exposed to 2*g* (red) vs. 1*g* (grey) were necrotic when they appeared Annexin V and PI double positive. For every time point the two conditions were compared via t-test, as well as both curves compared via Mann-Whitney test. Apoptosis and necrosis rates were not significantly different. Sample size n is 3 individual astrocyte cultures derived from 3 gravid mice. Values are shown as SEM. Scale bar represents 100 µm.

To compare the apoptosis rate of astrocytes exposed to 2*g* hypergravity with 1*g* control conditions, an Annexin V immunofluorescence assay was performed (see Figure 16A, B). Annexin-V is a protein specifically recognizing apoptotic cells by binding phosphatidyl-serine amino acid-residues that are exposed on the outer layer of plasma membrane already during early stages of apoptosis. Low apoptosis rates occur in astrocytes in vivo, which is reflected in the in vitro model. Upon induction of reactive astrogliosis, the cells undergo a phenotypic change and enhance cell maintenance diminishing apoptosis rates.

Annexin V positive cells were counted in both conditions and the percentages of positive cells was compared. Over the analyzed time frame of 48 hours, the apoptosis rate between cells at 2*g* and 1*g* was similar, with the lowest values after 12 hours (2*g*: 2.79% ± 0.35%; 1*g*: 2.69% ± 0.20%) and a slightly increasing apoptosis rate at 48 hours (2*g*: 2.97% ± 0.32%; 1*g*: 3.01% ± 0.29%). The fraction of apoptotic cells between the 2*g* and 1*g* samples did not significantly diverge.

By also incubating the samples with propidium iodide (PI) and counting the number of Annexin V and PI double positive cells, the percentage of necrotic cells in the culture could be determined (see Figure 16C). The 1*g* control sample showed a slight increase of the number of necrotic cells over 48 hours (6h: 0.69% ± 0.16%; 48h: 0.81% ± 0.24%). The astrocytes exposed to 2*g* showed similar numbers (6h: 0.74% ± 0.21; 48h: 0.85% ± 0.25%) with a

transient increase after 12 hours (0.84% ± 0.14%). There was no significant change in necrotic cell number under 2*g*.

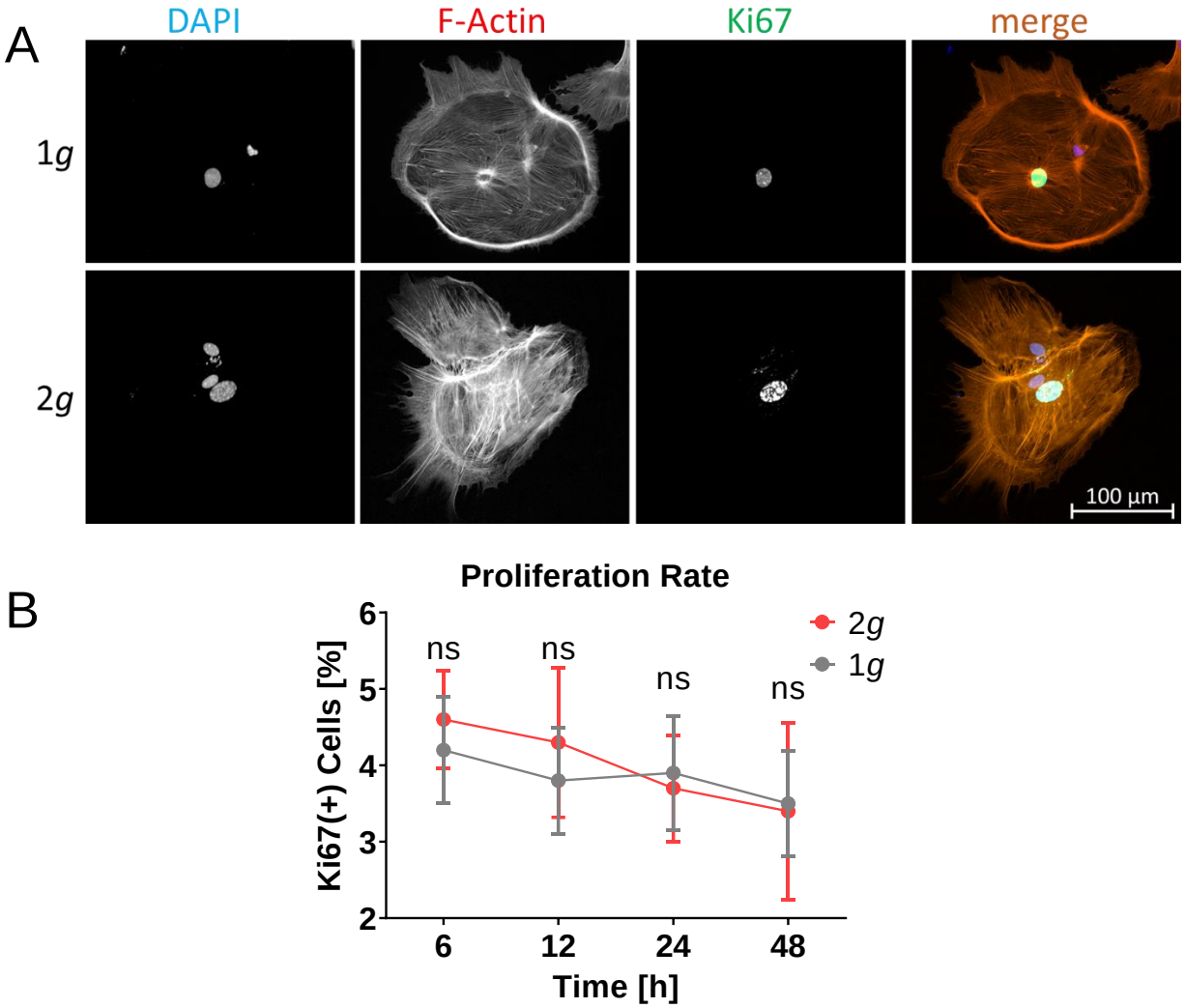

Figure 17: Cell proliferation analysis by Ki67 immunofluorescent staining of astrocytes exposed to hypergravity over two days. (A) Exemplary immunofluorescence image of astrocytes stained with DAPI, Phalloidin as an F-actin stain and an anti-Ki67 antibody, with the 1*g* control in the top row and the 2*g* hypergravity sample in the bottom row. **(B)** Percentage of Ki67-positive cells (± SEM). The number of Ki67-positive nuclei with SEM of astrocytes exposed to 2*g* (red) vs. 1*g* (grey) were counted after 6, 12, 24, and 48 hours of exposure. For every time point the two conditions were compared via t-test, as well as both curves compared via Mann-Whitney test and found to be not significantly different. Sample size n is 3 individual astrocyte cultures derived from 3 gravid mice. Scale bar represents 100 µm.

Astrocytes are glial cells that in their native state usually proliferate very slowly but are increasingly proliferative upon induction of a reactive state. To measure the percentage of proliferating astrocytes in each sample the cells were stained with an antibody specifically recognizing the protein Ki67, a well-established marker protein exclusively expressed in nuclei of replicating cells. Astrocytes with a Ki67-positive stained nucleus were classified as proliferating cells and the ratio to non-proliferating cells that were visualized only by DAPI staining, was calculated (see Figure 17A, B). Astrocytes exposed to 2*g* hypergravity and 1*g* control cells showed similar percentages of proliferating cells that declined slightly over time.

Highest proliferation rates were measured after 6 hours (2*g*: 4.60% ± 1.10%; 1*g*: 4.20% ± 1.20%) and a minimum was reached after 48 hours (2*g*: 3.40% ± 2.00%; 1*g*: 3.50% ± 1.20%). Comparison of the control and hypergravity samples did not show any significant changes in proliferation between those conditions. In both the 2*g* hypergravity exposed cells as well as the 1*g* control, over time, a slight decrease in in the number of proliferating cells was observed, which did not correlate with hypergravity exposure.

2.2 Astrocyte reactivity marker expression under hypergravity

One of the hallmarks of astrocytic reactivity is a change in gene expression levels, which manifests in increasing amounts of e.g., GFAP, vimentin, nestin and leucine-zipper kinase (LZK). Since other astrocyte properties related to astrocyte reactivity and further to glial scar formation such as spreading rates and cell polarization were influenced by 2*g* hypergravity exposure (see 2.1.1), the reactivity state of primary murine astrocytes was analyzed using high-resolution fluorescence microscopy.

2.2.1 GFAP expression in astrocytes under hypergravity

Glial fibrillary acidic protein (GFAP) is an intermediate filament expressed in the brain mainly by astrocytes. Studies have confirmed that astrocytes expressing high levels of GFAP are in a reactive state compared to the basal expression levels of GFAP in native astrocytes. Primary murine astrocytes were exposed to 2*g* hypergravity in the MuSIC incubator centrifuge for five days on glass coverslips and fixed at several time points. The cells were then fluorescently stained with a specific antibody against GFAP. Cells expressing the protein were determined and their percentage compared to total cell numbers was calculated in order to examine if hypergravity exposure modulates the number of GFAP positive, reactive cells. These values were compared to time-matched 1*g* control samples. Three biological replicates derived from individual gravid mice with two technical replicates each were imaged.

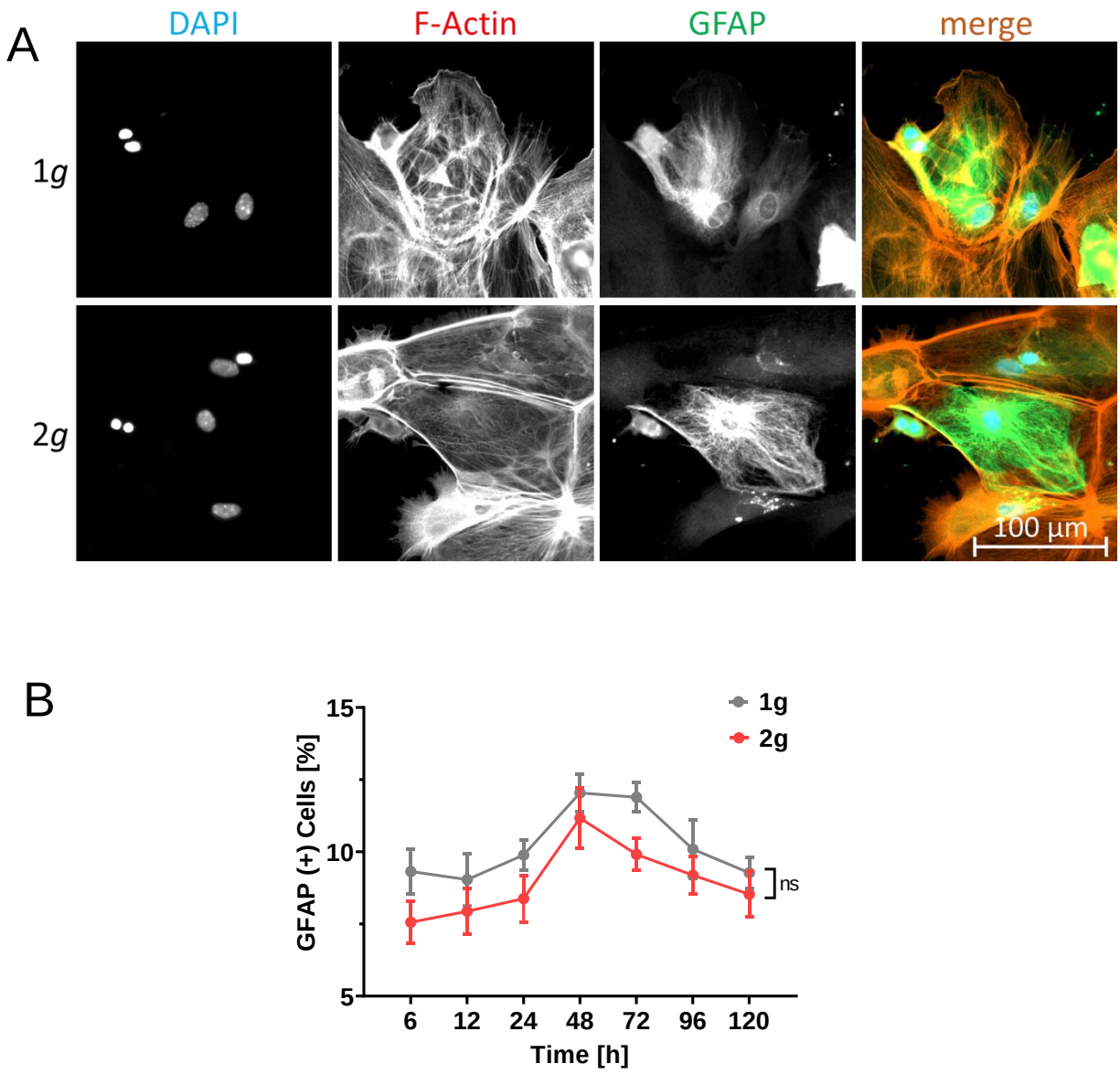

Figure 18: GFAP expression in primary murine astrocytes. (A) Exemplary immunofluorescence image of astrocytes stained with DAPI, Phalloidin as an F-actin marker and an anti-GFAP antibody, with the 1*g* control in the top row and the 2*g* hypergravity sample in the bottom row. **(B)** Line graph depicting the mean percentage of GFAP expressing astrocytes (± SEM) of a 1*g* control sample (grey) and of cells exposed to 2*g* hypergravity (red), compared via Mann-Whitney test. Sample size n is 3 individual astrocyte cultures derived from 3 gravid mice. Scale bar represents 100 µm.

In primary murine astrocyte culture, cells expressing high levels of GFAP can be clearly distinguished from basally expressing cells using epifluorescence microscopy (see Figure 18A). After six hours of hypergravity exposure 7.56% ± 1.25% of cells showed a GFAP signal in contrast to 9.32% ± 1.32% of the control which translated to 18% reduction in 2*g* compared to 1*g*. In both conditions the GFAP expression increased steadily with a peak being reached after 48 hours. At this time point 12.04% ± 1.12% of cells in the control were expressing GFAP and a fraction of 11.17% ± 1.82% GFAP positive cells was detected under hypergravity exposure. Over the next three days the GFAP expression in the 1*g* control as well as the hypergravity exposed cells decreased again, reaching 9.27% ± 0.92% in the control and 8.53%

± 1.37% in the hypergravity sample at the end of the experiment. At each investigated time point the hypergravity exposed cells had a lower percentage of GFAP expressing cells than the 1*g* control sample. However, a Mann-Whitney test did not reveal a significant difference.

2.2.2 LZK, GFAP, vimentin, and nestin fluorescence intensity in astrocytes under hypergravity

Not only GFAP, but also other proteins are suspected to be involved in astrocyte reactivity on a cellular level. Proteins analyzed were leucine zipper Kinase (LZK), and the intermediate filaments GFAP, vimentin, and nestin. Here, fluorescence intensities were measured as arbitrary units rather than counting individual positive cells.

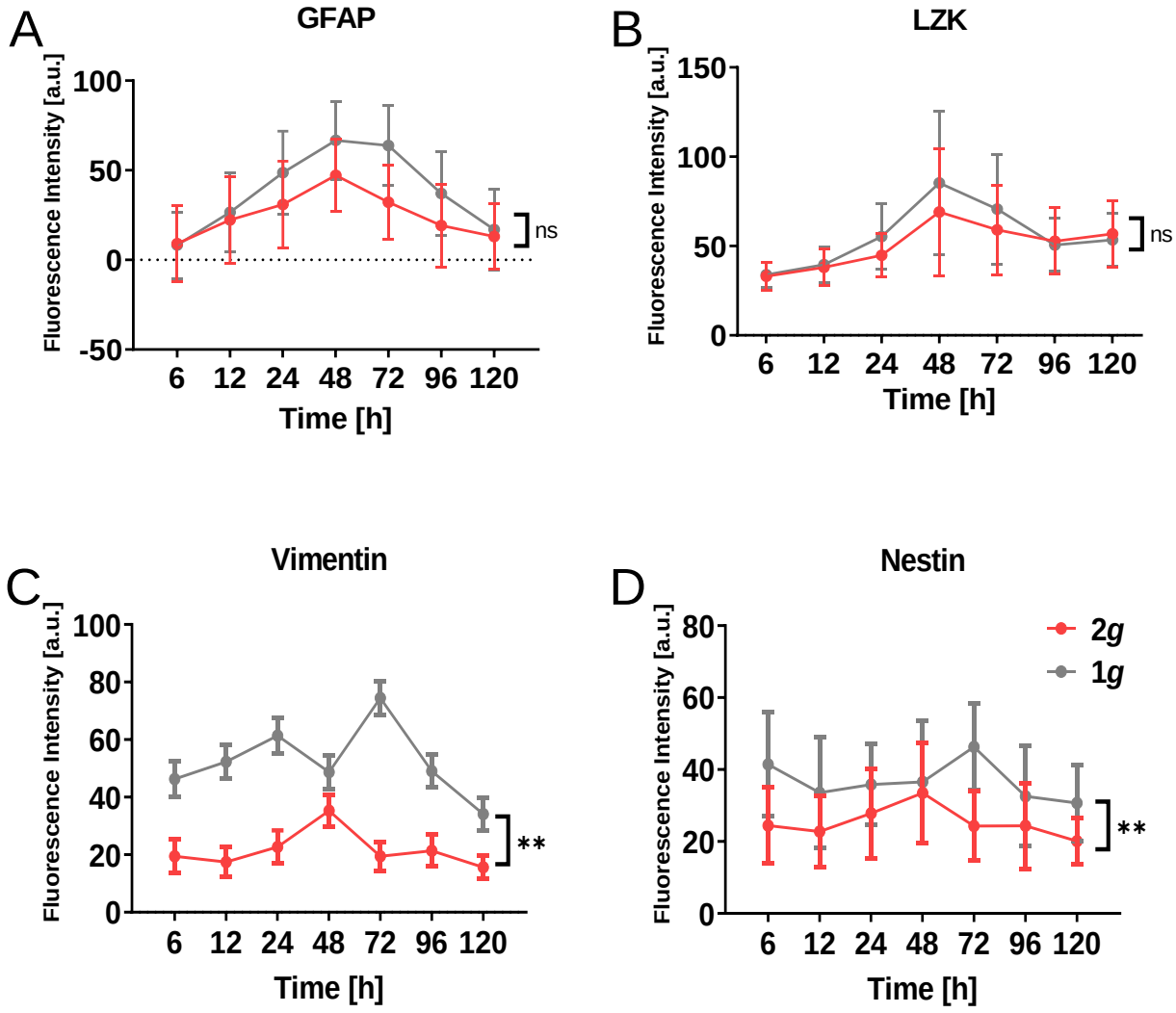

Figure 19: Fluorescence intensity of glial reactivity markers after hypergravity exposure. Depicted is the mean fluorescence intensity (±SEM) of cells stained with specific antibodies against GFAP **(A)**, LZK **(B)**, vimentin **(C)**, and nestin **(D)** in arbitrary units (a.u.). Mean values for the 1*g* sample (grey) and 2*g* hypergravity sample (red) are shown with SEM. The 1*g* and 2*g* samples were compared via Mann-Whitney test, the p-values were 0.3176 for GFAP, 0.7104 for LZK, 0.0012 for vimentin and 0.0023 for nestin. The sample size n was 20,159 cells (GFAP),19,777 cells (LZK), 20,821 cells (nestin),

and 21,426 cells (vimentin) each derived from 3 individual astrocyte cultures derived from 3 gravid mice Representative fluorescence microscopy images for all markers see Supplementary Figure 1 and Supplementary Figure 2.

The mean fluorescence intensity for GFAP increased nearly linearly from six hours to 48 hours where it reached a peak in both the control and the hypergravity sample (see Figure 19A). In the 1*g* sample the 48 hours intensity value was 606% of the starting intensity measured at the six-hour time point. In comparison, hypergravity exposed cells only increased their GFAP fluorescence intensity by 317% after 48 hours which was not significantly lower. Over the following three days both the 1*g* control and the 2*g* sample showed a reduction in GFAP fluorescence intensity, reaching a 5% increased intensity after 120 hours compared to the six-hour starting time point for the 1*g* sample and a 2% increase for the hypergravity sample, respectively. The divergence between the two conditions increased steadily up to the 48-hour time point and decreased steadily from 48 hours to 120 hours. However, there was a high standard error in each sample reaching from 1.7x to 3.9x of the measured fluorescence value.

LZK fluorescence intensity showed an increase from six hours to a maximum at 48 hours, analogous to GFAP (see Figure 19B). The control sample increased by 152% in fluorescence from six hours to 48 hours, whereas the hypergravity exposed cells had a 109% increase over the same time. The LZK fluorescence decreased in both samples from 48 hours to 96 hours, reaching 49% increase for the 1*g* sample and 60% increase for the 2*g* sample as compared to the six-hour values. From 96 hours to 120 hours LZK fluorescence intensity again appeared to increase slightly in both samples.

For the vimentin fluorescence analysis, the 2*g* hypergravity sample exhibited an on average far lower value compared to the normal gravity sample, starting at six hours with a 58% lower value compared to the control (see Figure 19C). Under 2*g*, the vimentin fluorescence peaked after 48 hours of exposure, with an 81% increase compared to the six-hour time point. After 72 hours of hypergravity exposure, the vimentin fluorescence reached a similar intensity as in the start of the experiment, with a slightly decreasing trend from 72 hours to 120 hours. The control sample, in comparison, exhibited an increase in fluorescence from six hours to 24 hours by 32%, then after 48 hours, a temporary low point of only 5% increase was reached. At 72 hours, the vimentin fluorescence reached its maximum of 60% increase compared to the six-hour time point. From 72 hours to 120 hours a steady decrease was measured, reaching a 26% reduction at the last measured time point as compared to the six-hour time point. The hypergravity sample was significantly different from the control sample as confirmed by a Mann-Whitney test with $p = 0.0012$.

The nestin fluorescence intensity was comparable to the observations made in the vimentin sample. Also, here the hypergravity sample displayed generally lower values compared to the control, starting at six hours with a 41% decreased fluorescence intensity compared to the control at the same time (see Figure 19D). The nestin fluorescence intensity peaked after 48

hours in the hypergravity sample with a 37% increase. From 72 hours to 120 hours a declining trend in the fluorescence was observed, ending with an 18% reduction compared to the starting value. In the 1*g* control, the fluorescence first decreased by 19% from six hours to 12 hours. It then increased again until a maximum of 12% increased fluorescence was reached after 72 hours. From this time point on, the nestin fluorescence decreased steadily, reaching a low point of 26% reduction compared to the starting point at six hours. This lowest value was the only data point in the control sample which was lower than the maximum of the values in the hypergravity sample. The hypergravity sample was significantly different from the control sample as confirmed by a Mann-Whitney test with $p = 0.0023$.

2.3 Nuclear morphology influenced by hypergravity exposure

The cell nucleus is a plastic structure and coupled to actin and intermediate filaments of the cell. Any changes in gravity exerted on a cell can be transmitted to the nucleus by those load-bearing elements of the cytoskeleton and in addition, changes in gene expression of a cell will also affect the nuclear morphology. Nuclear morphology was shown to be affected in reactive astrocytes depicting irregular and lobed nuclei (Liddelow, Guttenplan et al. 2017, Schiweck, Eickholt et al. 2018). Astrocytes in culture tend to fuse into syncytia, leading to multinuclear cells plainly visible in fluorescence microscopy with a DNA-binding staining. To investigate if 2*g* hypergravity exposure leads to changes in nuclear morphology or the number of nuclei per cell, primary murine astrocytes were exposed to hypergravity for one and two days in the MuSIC incubator centrifuge, afterwards fixed and stained with DAPI to be imaged at highest-possible resolution with an epifluorescence microscope. Using the Zeiss Zen image analysis tools, nuclei were semiautomatically detected in the microscopic images and their number, as well as several morphological parameters were analyzed (see Figure 20).

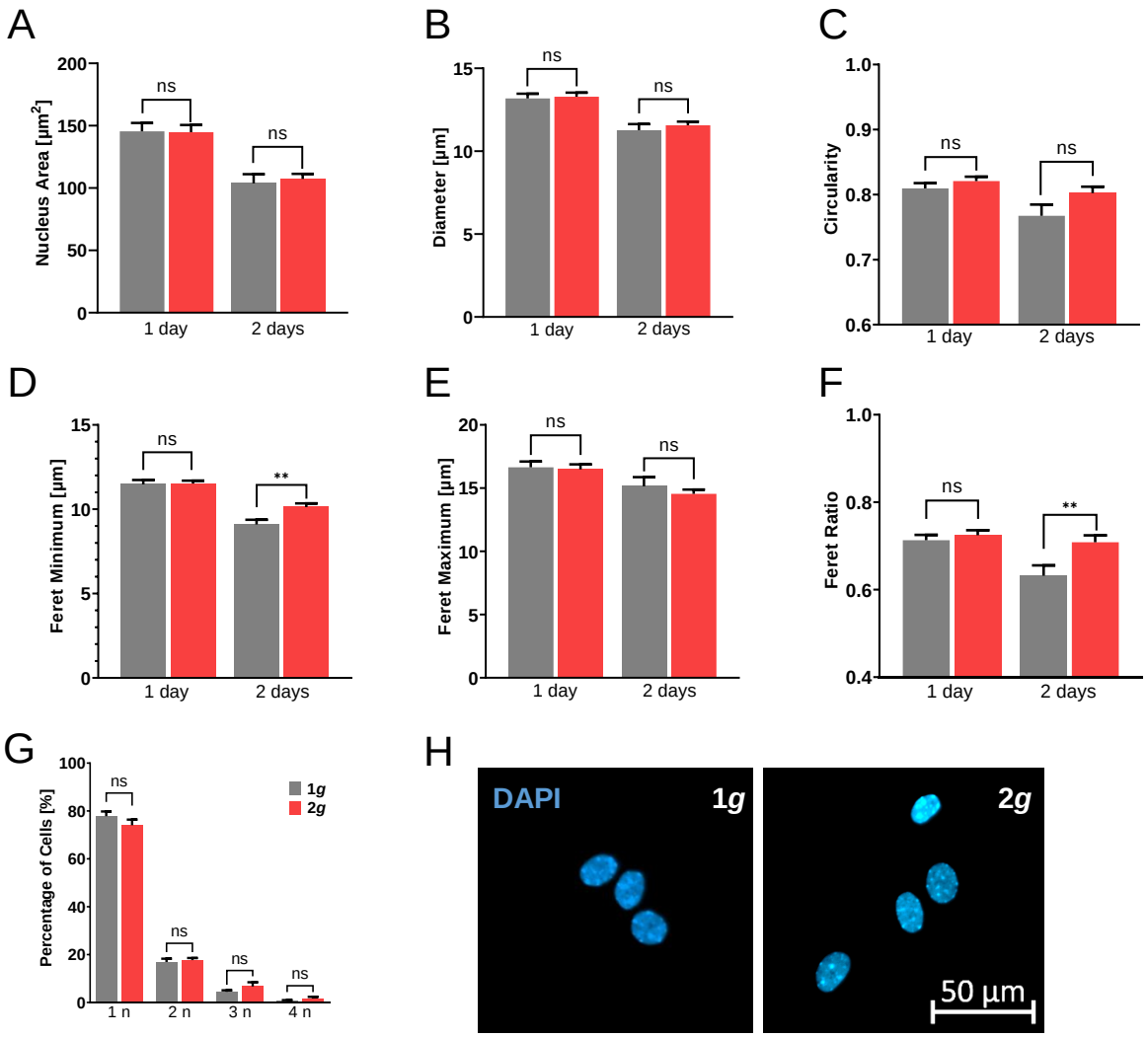

Figure 20: Nucleus morphology and count in astrocytes exposed to 2*g* hypergravity. (A) Mean area with SEM of nuclei after one day in the 1*g* control group (grey, 145.5 µm² ± 6.7 µm²) and under 2*g* hypergravity (red, 144.8 µm² ± 5.8 µm², p = 0.9372), and after two days in 1*g* (103.8 µm² ± 7.4 µm²) and 2*g* (107.3 µm² ± 4.1 µm², p = 0.6533). **(B)** Mean diameter with SEM of nuclei after one day in the 1*g* control group (grey, 13.2 µm ± 0.3 µm) and under 2*g* hypergravity (red, 13.3 µm ± 0.2 µm, p = 0.7866), and after two days in 1*g* (11.3 µm ± 0.4 µm) and 2*g* (11.6 µm ± 0.2 µm, p = 0.4638). **(C)** Mean circularity with SEM of nuclei after one day in the 1*g* control group (grey, 0.81 ± 0.01) and under 2*g* hypergravity (red, 0.83 ± 0.01, p = 0.2907), and after two days in 1*g* (0.76 ± 0.01) and 2*g* (0.8 ± 0.01, p = 0.0633). **(D)** Mean Feret minimum with SEM of nuclei after one day in the 1*g* control group (grey, 11,5 µm ± 0.3 µm) and under 2*g* hypergravity (red, 11.5 µm ± 0.2 µm, p = 0.8834), and after two days 1*g* (9.1 µm ± 0.3 µm) and 2*g* (10.1 µm ± 0.2 µm, p = 0.0044). **(E)** Mean Feret maximum with SEM of nuclei after one day in the 1*g* control group (grey, 16.6 µm ± 0.5 µm) and under 2*g* hypergravity (red, 16.5 µm ± 0.4 µm, p = 0.7895), and after two days in 1*g* (15.1 µm ± 0.7 µm) and in 2*g* (14.5 µm ± 0.3 µm, p = 0.4048). **(F)** Mean Feret ratio with SEM of nuclei after one day in the 1*g* control group (grey, 0.71 ± 0.01) and under 2*g* hypergravity (red, 0.73 ± 0.01, p = 0.4951), and after two days 1*g* (0.63 ± 0.02) and 2*g* (0.71 ± 0.01, p = 0.0063). Sample size n is (1 day: 1*g*=140; 2*g*=131; 2 days: 1*g*=39; 2*g*=61) cells from 1 individual astrocyte culture derived from 1 gravid mouse. **(G)** Average percentage with SEM of nuclei per cell of astrocytes exposed to 1*g* control conditions (grey, n = 844) and 2*g* hypergravity (red, n = 680) for up to two days. One nucleus was observed in 77.8% ± 2.0% of 1*g* and in 74.1% ± 2.3% (p = 0.2364) of 2*g* cells. Two nuclei were observed in 16.9% ± 1.4% of 1*g* and in 17.7% ± 0.9% (p = 0.6417) of 2*g* cells. Three nuclei were observed in 4.5% ± 0.6% of 1*g* and in 6.7% ± 1.7% (p = 0.2141) of 2*g* cells. Four nuclei were observed in 0.8% ± 0.2% of 1*g* cells and in 1.6% ± 0.8% (p = 0.2664) of 2*g* cells. The sample size n is 1*g*=844; 2*g*=680 cells from 2 individual astrocyte cultures derived from 2 gravid mice. **(H)** Immunofluorescence image of astrocyte nuclei stained with DAPI, under normal 1*g* gravity (left) and 2*g* hypergravity (right). Scale bar represents 50 µm.

The size of astrocyte nuclei measured in µm² did not differ between cells exposed to 2*g* hypergravity and the 1*g* control after one day of exposure. After two days in culture, the average area of nuclei in the control group decreased by 29%, whereas the average nuclear area of astrocytes exposed to two days of hypergravity decreased by 26%. This led to an average of 3% larger nuclei in the hypergravity sample, compared to the control at the same time point. This difference in nuclear area was not significant as confirmed by t-test. The average diameter of the nuclei followed the same trend as the area (see Figure 20B). After one day, both the control and hypergravity samples had similar nucleus diameters, with an average of 15% decrease in the control group after two days and a 13% decrease seen in the hypergravity sample. This led to a slightly but not significantly higher nucleus diameter in the 2*g* sample compared to the control.

Astrocyte nuclei were slightly more circular after one day of hypergravity exposure (see Figure 20C). After two days in culture the nuclear circularity in both conditions decreased. The average circularity of nuclei in the control sample decreased by 5%, whereas in the hypergravity sample roughly 2% of decrease in circularity was observed. The increase in circularity in the hypergravity exposed sample increased from 1% after one day of exposure to 3% after two days. This trend was not significant.

The Feret minima of both conditions were similar after one day (see Figure 20D). After two days, the average Feret minimum of the control cells was 20% lower than after one day. The nuclear Feret minima of the 2*g* cultured astrocytes only decreased by 12% over the same time, leading to a significant increase compared to the 1*g* sample. The Feret maxima behaved differently than the minima in the way that they were similar after one day, but after two days of exposure the control cells showed an on average 4% increased Feret maximum compared to the 2*g* sample at the same time (see Figure 20E). From one day to two days, the average Feret maximum on nuclei in the control group decreased by 9%, whereas in the hypergravity group a larger decrease of 12% was observed. These diverging trends regarding the Feret values led to a slightly higher Feret ratio in the hypergravity sample after one day of exposure (see Figure 20F). This 1.6% increase of the Feret ratio in the 2*g* sample was not significant. After two days of exposure, the Feret ratio of nuclei from the hypergravity group did only decrease slightly from the one-day time point. In contrast to this, in the control group a large decrease of the Feret ratio by 12% was observed. This led to a significantly higher Feret ratio of the hypergravity exposed nuclei after two days of exposure in comparison to the 1*g* control group at the same time point.

Counting the number of nuclei per astrocyte in cells exposed to 2*g* hypergravity for two days and a time-matched control group did not show any significant changes in the number of multinucleated cells. There were 3.8% more cells with one nucleus in the control group compared to the 2*g* sample and 0.8% more cells with two nuclei in the hypergravity sample.

Three nuclei were counted in 2.2% more cells of the hypergravity sample than in the control and four nuclei were counted in 0.8% more 2*g* exposed cells compared to the 1*g* sample. All these differences were not significant as controlled via t-test.

2.4 Effects of hypergravity on astrocyte migration

One of the hallmarks of the central nervous systems response to injury is the infiltration of injured tissue with reactive astrocytes. This is in part facilitated by the migration of reactive astrocytes from the surrounding tissue into the area of the insult. Since hypergravity exposure had direct and immediate effects on astrocyte morphology and spreading dynamics (see 2.1) which are mediated by the cytoskeleton and associated force-transducing proteins, it is plausible that the migratory behavior of these cells might also be influenced by hypergravity exposure.

2.4.1 Astrocyte migration speed reduced after five days of hypergravity exposure

To measure cellular migration in culture, the wound-healing assay (“scratch assay”) was developed. Here, cells are grown until confluency and a cell-free region between the confluent cells is exposed to start migration. The migration of surrounding cells back into this area can then be observed and quantified. The basic scratch assay is flawed in the regard, that the scratch area is hard to standardize, and by scratching a lot of cells are damaged and destroyed, leading to apoptosis and inflammatory responses in the culture. To circumvent this, for the following experiments an Ibidi cell culture chamber was used (see 4.3). A silicone scaffold with three wells was placed in a 3.5 cm petri dish and primary murine astrocytes were seeded into each well. After the cells were grown to confluency, the scaffold was carefully removed, leaving a standardized, 500 µm broad cell-free area between each well and doing only minimal harm to surrounding cells. The cells would then migrate into the cell-free areas without being influenced by dead cells or apoptotic bodies in the culture vessel. This modified scratch assay also is closer to *in vivo* CNS conditions in for this reason, since migrating, reactive astrocytes are not directly damaged as they are situated at a distance from the injury.

Three primary astrocyte cultures taken from separate mice were then exposed to 2*g* hypergravity in the MuSIC incubator centrifuge for five days and the cell-free area was imaged daily. As cells migrated back into the cell-free area, this area decreased, and its area could be measured to compare to control cells at 1*g*.

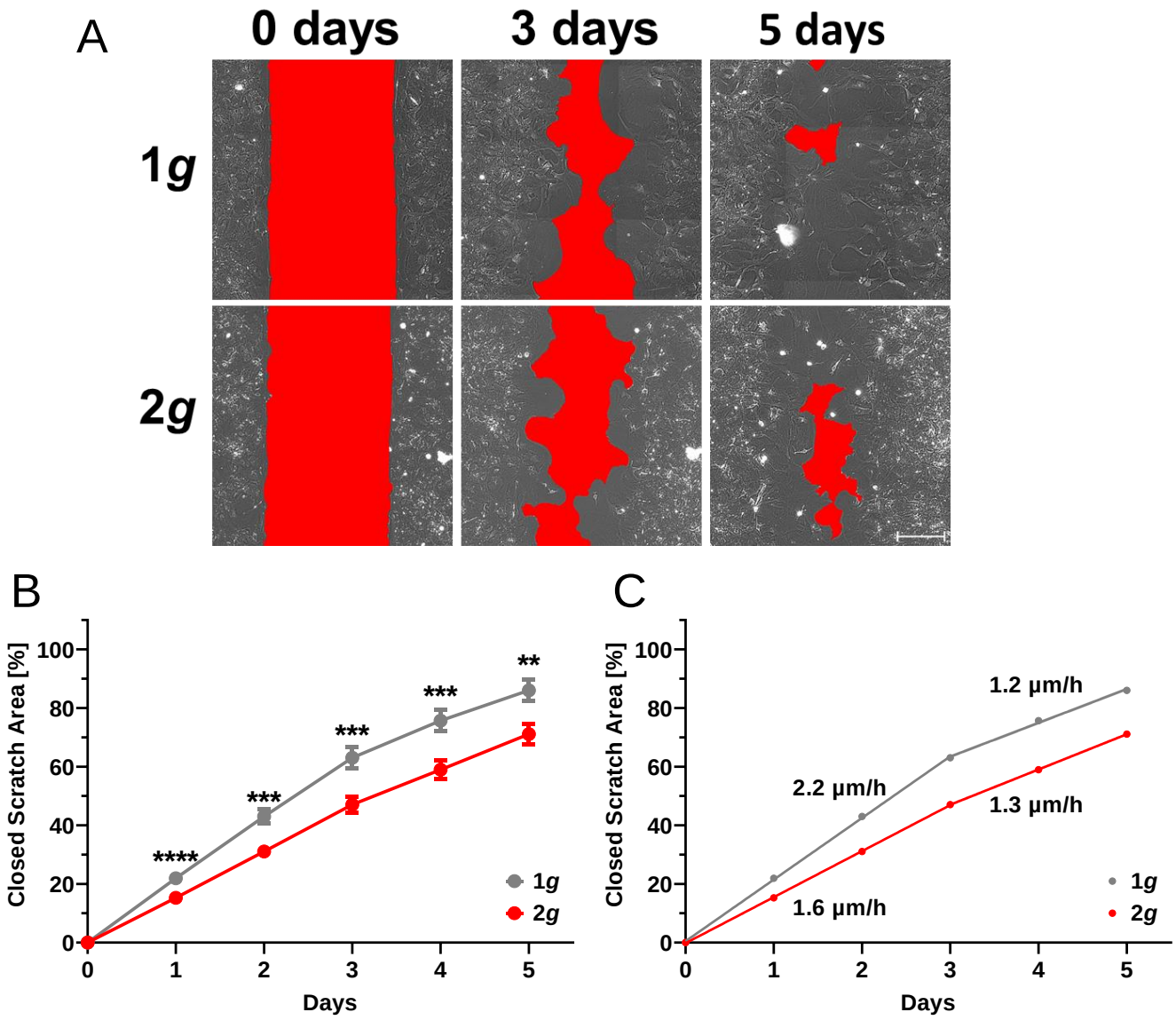

Figure 21: Astrocyte migration velocity determination by wound-healing assay. (A) Phase contrast microscopy images of an astrocyte wound-healing assay. Top row shows the 1*g* control sample after initiation, three, and five days of incubation, with the cell free scratch area marked in red. Bottom row shows the same time points of a scratch assay that was incubated under 2*g* hypergravity exposure in the MuSIC incubator centrifuge. Scale bar represents 200 µm. **(B)** Line graph showing the average closed scratch area and SEM of 2*g* hypergravity exposed astrocytes (red) and a 1*g* control (grey) over the time of five days. For each time point, a t-test was performed (day 1: $p < 0.001$; day 2: $p = 0.002$; day 3: $p = 0.008$; day 4: $p = 0.008$; day 5: $p = 0.0049$). **(C)** Regression lines and average migration speeds for the 1*g* (grey) and 2*g* (red) data, split into the time from 0 days to 3 days (1*g* = 2.2 µm/h; 2*g* = 1.6 µm/h) and the time from 3 days to 5 days (1*g* = 1.2 µm/h; 2*g* = 1.3 µm/h). Sample size n is 1*g* = 28; 2*g* = 32 with a dimension of 4 mm x 0.5 mm each from 3 individual astrocyte cultures derived from 3 gravid mice.

The migration speed of primary murine astrocytes, as measured by the reduction of cell-free area during the wound-healing assay, was significantly reduced by 2*g* hypergravity exposure (see Figure 21). At the first measured time point, after one day of hypergravity exposure, the closed cell-free area was closed on average 15.3% ± 1.0% which was significantly lower than in the 1*g* control (22.0 % ± 1.2%). The closed cell-free area increased for each sample linearly

with diverging slopes for exposure at 1*g* and 2*g*. On day 2 average cell-free area was closed at 2*g* 31.1% ± 1.9% and at 1*g* 43.0% ± 2.4% and on day 3 average 47.1% ± 2.8% for 2*g* and 63.0% ± 3.6% for 1*g*. With the beginning of day 4, both curves started to flatten slightly (average 2*g*: 59.0% ± 3.0%; 1*g*: 75.7% ± 3.7%), at this point, 15% of the measured 1*g* scratches were closed completely versus none in the hypergravity sample. After five days, which was the last time point measured in the experiment, the remaining cell-free areas began to converge (average 2*g*: 71.1% ± 3.5%; 1*g*: 86.0% ± 3.7%). In the control sample, 56% of the cell-free areas were closed, versus only 15% of closed areas in the 2*g* hypergravity sample. Over the course of the experiment, a steadily decreased migration velocity was observed at 2*g* hypergravity compared to cells migrating under normal gravity. By fitting regression lines onto the data, the average migration speed of the cells at different intervals could be calculated (see Figure 21C). The slopes of the regression lines could be seen as the cell-free area closing speed with the unit %/day. The observed cell free area had a width of 500 µm set to 100% of the cell-free area, and the cell fronts migrated from both sides of the ”wound”. For this reason, cell migration speeds in this assay could be calculated with the following equation $Speed^{Migration}\,[\mu m/h] = \left(\frac{Slope * 5}{2}\right) : 24$

In the first three days, the migration speed of hypergravity-exposed astrocytes was with 1.6 µm/h significantly lower than the migration speed of the control cells of 2.2 µm/h. After the third day of the wound-healing assay, the migration speed of the control decreased by nearly 50% to 1.2 µm/h. The migration speed of the 2*g* cells also decreased to 1.3 µm/h which was only an app. 20% reduction. Remarkably, from day 3 to 5 the migration speeds in both samples were similar with only a small difference of 0.1 µm/h, from which can be concluded that hypergravity exposure has a stronger effect on migration speed in the first three days. After this time, an adaptation of the astrocyte migration to hypergravity appears to happen.

2.4.2 Astrocyte migration strongly impaired in the first 22 hours of hypergravity exposure, hinting to adaptation dynamics

The wound healing assay performed using the MuSIC incubator centrifuge (see 2.4.1) showed a significant decrease of astrocyte migration speed due to 2*g* hypergravity exposure. One weak point of the used experimental protocol was that for imaging of the scratch area, the samples had to be taken out of the centrifuge and imaged in a 1*g* environment. For that reason, the measured effect of hypergravity (10% - 15% reduction of migration rate) might be underreported since the samples had time to readapt to normal gravity whilst outside of the incubator centrifuge for imaging. This time amounted to approximately one hour per day of the assay. To ameliorate this confounding factor and to get a better insight into fast acting dynamics in astrocyte migration behavior, a similar Ibidi cell culture chamber-based approach scratch assay was performed on the Hyperscope platform (see 4.1.2). This comprises a live-cell epifluorescence microscope mounted on a swing-out platform on the short-arm human centrifuge at the DLR :envihab. On the Hyperscope, living cells can be microscopically imaged under hypergravity conditions of up to 2*g* and otherwise unchanged standard cell culture incubation environments (i.e., 37°C, 5% CO_2, >95% relative humidity). Three Hyperscope experiment runs with three independent primary astrocyte cultures were performed for 22 hours each with the whole scratch area being imaged every 30 minutes. The same regimen was then repeated with the centrifuge standing still to record the migration behavior of the 1*g* control.

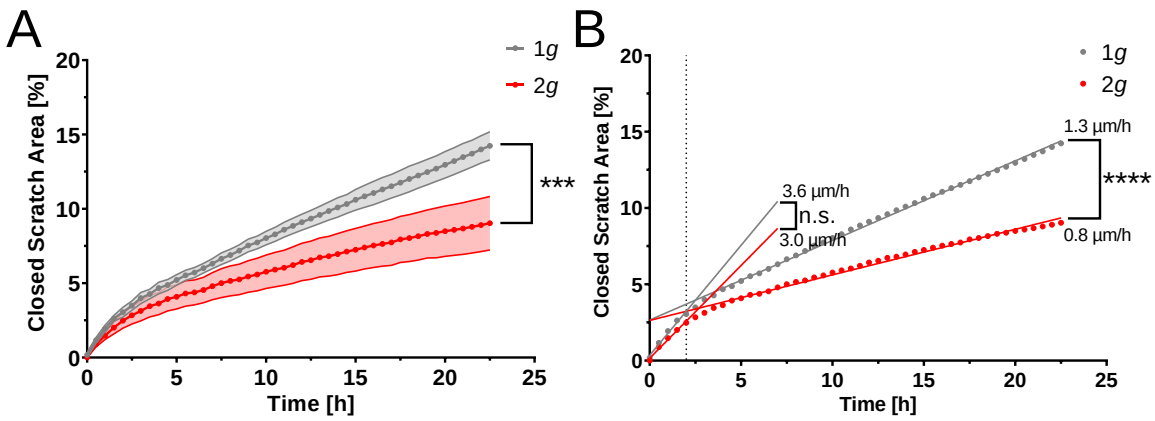

Figure 22: Acute migration effects of astrocytes imaged live during centrifugation on the Hyperscope platform. (A) Line graph showing the average closed cell-free area and SEM of astrocytes exposed to 2*g* hypergravity (red) and 1*g* control cells (grey) over 22 hours of exposure. The two curves were compared with a Mann-Whitney test (p = 0.005). **(B)** Linear regression for the time points 0h - 2.5h and 2.5h - 22h with the migration speeds of each sample, calculated from the slope, marked on the graph. The migration speeds of the 2*g* and 1*g* samples between 0h and 2.5h are not significantly different, whereas the speeds of the 2*g* and 1*g* samples from 2.5h to 22h are significantly different (p < 0.0001). The sample size n was 1*g* = 6 and 2*g* = 6 separate wound-healing areas each with a dimension of 4 mm x 0.5 mm from 3 individual astrocyte cultures derived from 3 gravid mice.

The 22-hour long live wound-healing assay on the Hyperscope confirmed the observations made with the long-term wound-healing assay on the MuSIC (see 2.4.1). After 22 hours of 2*g* hypergravity exposure on the centrifuge with an image frequency of 30 minutes, the hypergravity-exposed astrocytes migrated significantly less than the 1*g* control cells (see Figure 22A). At the end of this experiment the hypergravity samples had an average closed cell-free area of 9.0% ± 0.3% compared to 14.2% ± 0.6% in the control sample, translating to a 35% reduction of migration speed under 2*g* hypergravity. Furthermore, when examining the migration velocities, a lag phase of 2.5h at the start of the experiment became apparent, where the cells in hypergravity had a similar, hyperbolic migration speed as the control cells and only following this lag phase, the migration speed of the cells in hypergravity tapered out and the cells migrated slower into the cell free area. To confirm this observation, linear regression lines were fitted for the 2*g* and 1*g* samples for the time from 0h to 2.5h and from 2.5h to the end of the experiment at 22h (see Figure 22B). The slopes of the regression lines could be seen as the cell-free area closing speed with the unit %/h. The observed cell free area had a width of 500 µm set to 100% of the cell-free area, and the cell fronts migrated from both sides of the ”wound”. For this reason, cell migration speeds in this assay could be calculated as $Speed^{Migration}[\mu m/h] = \frac{Slope * 5}{2}$. This resulted in the following values with the unit µm/h: up to 2.5h into the assay, the linear regression line of the 1*g* sample had a migration speed of 3.6 µm/h, compared to 3.0 µm/h for the 2*g* sample. Those velocities were not significantly different from each other, confirming the observation that the cells migrated with similar speed during this “lag” period. After 2.5 h until 22 h, the hypergravity sample had an average migration speed of 0.8 µm/h which was significantly lower than the migration speed of the 1*g* control at 1.3 µm/h. In the first 2.5 hours the scratch closing rate followed a hyperbolic curve, which at later time points approached a linear scratch closing rate in both samples.

2.4.3 Live-cell imaging of astrocyte migration in a 1*g* to 2*g* to 1*g* centrifugation protocol shows adaptation and re-adaptation of cell behavior to changing gravity conditions

In preceding experiments, it was shown that primary murine astrocytes react to 2*g* hypergravity exposure with an inhibition of cellular migration as measured by a wound-healing assay. Over the course of five days hypergravity exposure, the cells showed a decrease of 10 – 15% in closed scratch area compared to control cells (see 2.4.1). When investigating the dynamics of the inhibitory effect of hypergravity on astrocyte migration using live-cell microscopy on the Hyperscope, a 35% decrease in closed scratch area was observed after the initial 22 hours of migration (see 2.4.2). Furthermore, this setup allowed insight into the

temporal dynamics of the reduced migration speed, as there seemed to be a lag-phase of about 2.5h until the hypergravity-exposed cells showed a significant reduction of their migration speed.

To investigate what dynamics are at play in the adaptation of astrocyte migration to hypergravity and how the cells react to readaptation from hypergravity back to normal gravity, an intermittent centrifugation profile was devised to be executed on the Hyperscope. After starting the scratch assay, the sample was imaged on the Hyperscope microscope platform on the resting centrifuge at 1*g* for 12 hours in 30-minute intervals. Then the centrifuge was accelerated to 2*g* with a ramp up time of 2 minutes, and the imaging continued for another 12 hours. After this hypergravity phase, the centrifuge was stopped again, and the scratch assay was continued for a further 12 hours until the end of the experiment.

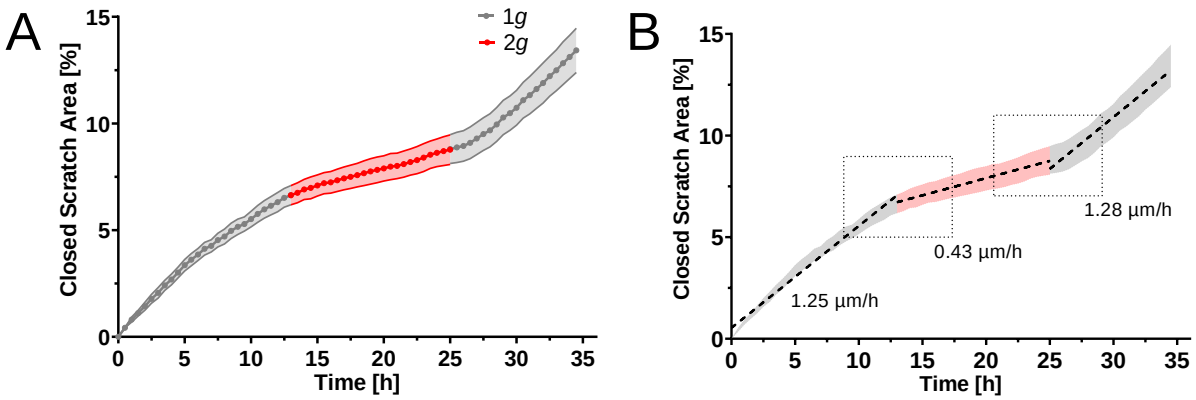

Figure 23: Astrocyte scratch hypergravity adaptation/readaptation assay on the Hyperscope. **(A)** Line graph showing the increase in average closed cell-free area with SEM over the time course of the experiment. The scratch was imaged under 1*g* normal gravity for 12 hours (grey) and then for 12 hours in 2*g* hypergravity (red). The last 12 hours the cells were again exposed to 1*g* normal gravity (grey). **(B)** Linear regression lines fitted to each segment of the experiment (striped lines) with the corresponding migration speed for each *g* phase below. Dotted boxes signify lag phases. Sample size n is 1*g*=8; 2*g*=8 separate cell-free areas each with a dimension of 4 mm x 0.5 mm from 2 individual astrocyte cultures derived from 2 gravid mice.

Employing this alternating gravity regimen, the adaptation as well as re-adaptation to altered gravity stimuli could be observed live with high precision. Astrocyte migration could efficiently be reduced by 2*g* hypergravity exposure in a time-dependent and reversible manner (see Figure 23A). The fitting of linear regression lines for each gravity phase revealed that for the first 12 hours in normal gravity the astrocytes migrated with an average speed of 1.25 µm/h which was similar to earlier experiments (see 2.4.2). With the start of 2*g* hypergravity exposure, a strong, linear effect was observed as a reduction of the migration speed to 0.43 µm/h over the 12 hours of hypergravity exposure. Compared to the normal gravity phase before hypergravity exposure, the migration speed was reduced by 76% through hypergravity exposure. After readaptation from 2*g* hypergravity back to 1*g* normal gravity, astrocytes migrated with a speed of 1.3 µm/h, very close to the initial migration speed at the start of the

experiment. From the observed samples, the migration speed appeared to be linear when not influenced by changes in gravitational loading.

At the start of the 2g exposure at 12 hours, the migration speed did not change instantaneously and seemed to lag behind approximately 1 h, visible in a misalignment of the linear regression lines (see Figure 23B). The same effect appeared to happen at the change from 2*g* hypergravity back to normal gravity at the 24 h time point, with an even more pronounced lag phase of 2 h and resulting misalignment of the two linear regression curves. Those adaptation and readaptation periods were more closely investigated to confirm the suspected lag phases in the response of astrocyte migration speed to changes in gravity loading.

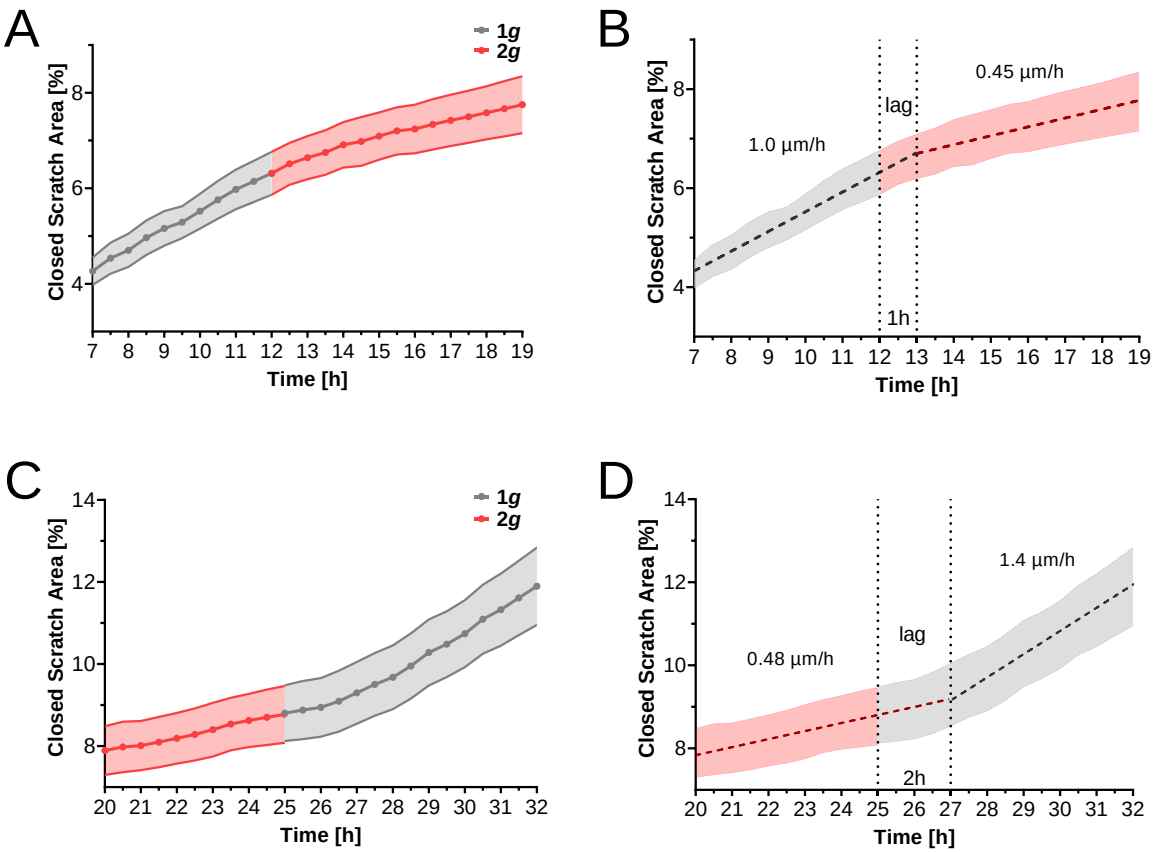

Figure 24: Adaptation to hypergravity and readaptation to normal gravity results in lag phases of astrocyte migration. (A) Zoomed in line graph showing a twelve-hour period between 7 and 19 hours of an astrocyte scratch assay on the Hyperscope platform. Cells were cultured in 1*g* normal gravity (grey) and then exposed to 2*g* hypergravity (red), with their migration speed being measured by live cell imaging as described before. Depicted is the average migration speed and SEM. **(B)** Linear regression lines for the 1*g* phase, including a 1-hour lag phase (black striped line) and for the 2*g* period (red striped line) with the respective migration velocities noted above both lines in µm/h. The lag phase needed for adaptation of the migration speed to 2*g* is shown between the vertical dotted lines. **(C)** Similar line graph as in (A) showing the period of readaptation from 2*g* (red) to 1*g* (grey). **(D)** Regression lines of the 2*g* period including a 2-hour lag phase (red striped line) and of the 1*g* period (black striped line), with their velocities noted above the lines. The 2-hour readaptation lag phase is shown between the vertical dotted lines. Sample size n is 1*g* = 8; 2*g* = 8 separate cell-free areas each with a dimension of 4 mm x 0.5 mm from 2 individual astrocyte cultures derived from 2 gravid mice.

At a closer inspection of the astrocyte migration speed when changing from 1*g* to 2*g* the suspected lag phase became apparent (see Figure 24A). The linear regression was computed from x = 7 h to x = 13 h, instead of up to x = 12 h, thus including one hour of potential re-adaptation lag phase (see Figure 24B). This led to a much better alignment of the two regression lines, confirming that the change in migration speed upon hypergravity exposure was not instantaneous. The same procedure was applied for the phase of re-adaptation to normal gravity after hypergravity exposure at the 24-hour time point (see Figure 24C). Here a lag phase of two hours was observed, with the linear regression line extended by two hours from x = 25 h to x = 27 h (see Figure 24D).

2.5 Qualitative examination of the astrocyte cytoskeleton after hypergravity exposure using super resolution microscopy

Changes in shape, localization, expression level, and distribution of cytoskeletal elements related to the tubulin- and actin-cytoskeleton are suspected to be caused by increased mechanical loading on astrocytes and could explain the observed defects in cell spreading and migration. Such cytoskeletal alterations are still notoriously difficult to quantify and are often analyzed qualitatively. Here, primary murine astrocytes were exposed for one 24h to 2*g* and 10*g* hypergravity inside the MuSIC incubator centrifuge compared to a 1*g* control. We performed super-resolution microscopy employing the STED (STimulated Emission Depletion, see 4.6.2) methodology to be able to detect fine architectural changes in the actin filament and microtubule network of astrocytes that have been exposed to altered mechanical loading with a resolution of up to 100 nm in the xy-plane. This facilitated the mapping of nearly the complete microtubule network inside these cells as well as many pronounced features of the actin and tubulin cytoskeleton.

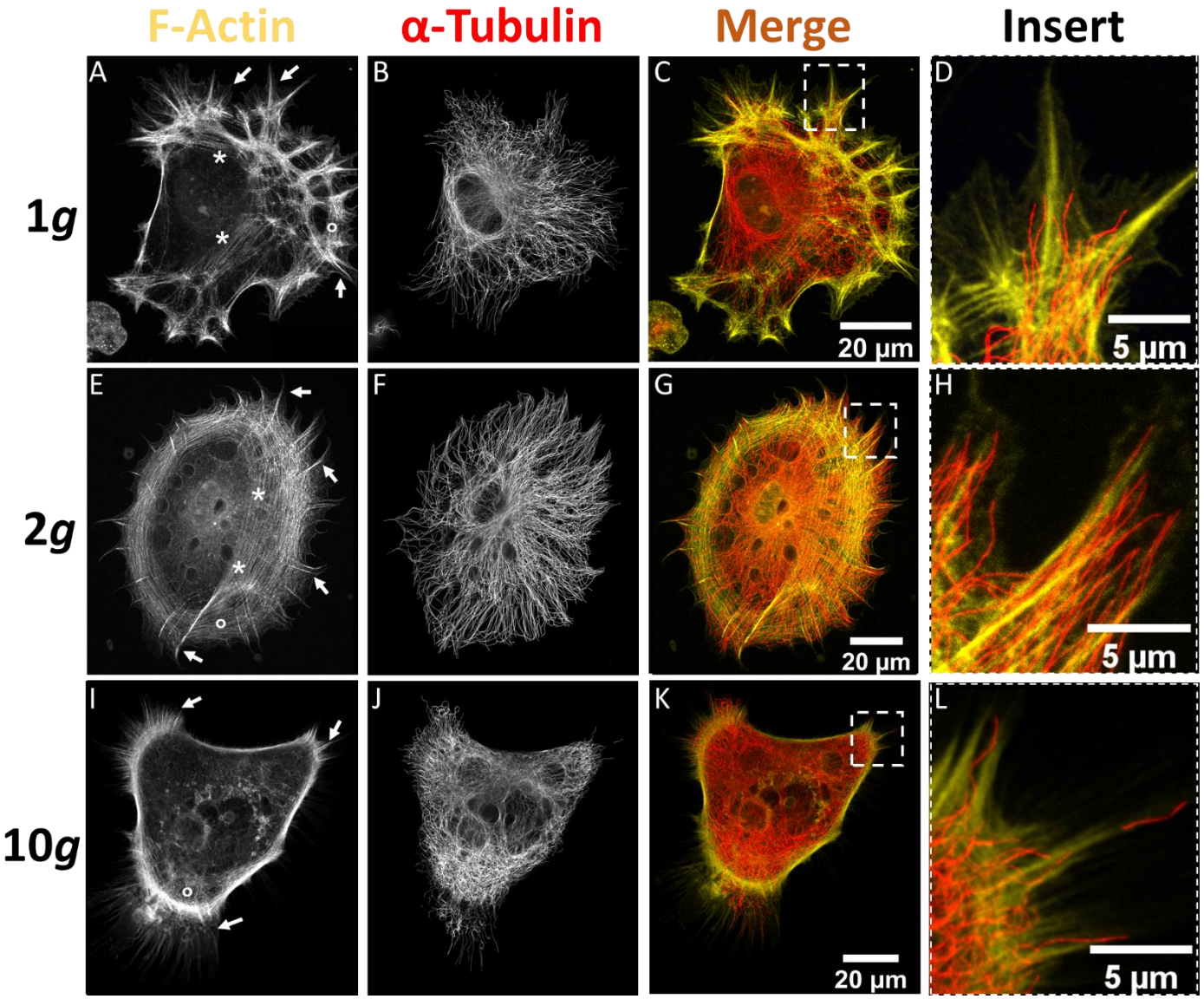

Figure 25: STED microscopy images of primary murine astrocytes cultured under 1*g*, 2*g*, and 10*g*. Shown are representative images of astrocytes exposed to 2g and 10g hypergravity as well as 1g normal gravity as a control. (A, E, I) The F-actin cytoskeleton was labelled using fluorescently conjugated Phalloidin. (B, F, J) The microtubule network is visualized by using an anti-alpha-tubulin antibody labeling. (C, G, K) The merged image of the actin (yellow) and tubulin (red) channels. (D, H, L) Checkered boxes indicate magnifications of lamellipodial and filopodial structures. Arrows mark lamellipodia with additional filopodia extruded from the cell membrane at various points. Asterisks mark bundles of transverse stress fibers reaching throughout the cell. The actin cortex including a strongly stained dendritic actin filament network close to the cell membrane are exemplary marked with rings (°) and is found throughout the cell perimeter. Scale bar represents 20 µm (C, G, K) and 5 µm (D, H, L).

A qualitative analysis of the actin cytoskeleton in 1*g* control cells (see Figure 25A) revealed the expected actin filament structures. The cells appeared to be polarized and protruded several large lamellipodia, rich in actin, with fine filopodia extruding at several locations from the lamellipodia. The actin cortex near the cell perimeter was rich in filamentous actin and a dendritic network was visible. Closer to the center of the cell, actin stress fiber bundles could be seen, spanning the cell from the retracting end to the direction of the filopodia. The astrocytes exposed to 2*g* for one day were less polarized, so several lamellipodia and filopodia

were visible on all sides of the cell (see Figure 25E). The actin cortex appeared to be very pronounced and many parallel stress fibers were stained inside the cell. Comparing this to the cells exposed to 10*g* hypergravity, several large lamellipodia were visible on either side of the cells, with many filopodia reaching further out (see Figure 25I). No intracellular or perinuclear stress fibers were observed, with the actin cortex easily visible on the sides of the lamellipodia, but much less pronounced on the less-polarized cells' perimeter. The microtubule network in all observed cells was densely packed and well-structured (see Figure 25B, F, J). In the control cells, the microtubules were aligned mostly around the perinuclear space, with the network thinning out towards the perimeter. Microtubules did not extend to the cell membrane and never reached the cell boundary (see Figure 25C, D). In the astrocytes exposed to 2*g*, the microtubule network was more evenly distributed from the cell center to the perimeter with only a slight increase in microtubule density in the perinuclear area. Microtubules could be observed reaching into the finest ends of lamellipodia and filopodia (see Figure 25G, H). After one day of 10*g* hypergravity exposure, the microtubule network inside the imaged astrocytes showed an increased density towards the cell perimeter, on the bases of the lamellipodia, with less density in the cell center (see Figure 25K, L). Altogether it seemed that there were more microtubules compared to the 2*g* and control cells. As in the samples exposed to 2*g*, microtubules could be observed reaching into fine lamellipodial extensions and reaching the cell membrane.

2.6 Employing the LifeAct-GFP mouse line to investigate actin dynamics under hypergravity

Cellular migration and spreading, as well as a multitude of other cell behaviors rely on actin fibers and associated molecules to generate protrusive and contractile forces. Actin fibers are needed for the generation of lamellipodia and filopodia or for the formation of actin stress fibers. Stress fibers are contractile bundles of actin filaments which are anchoring the cell body to its growth substrate via focal adhesions. They are essential in amoeboid cellular migration, as they can contract and drag the rear of the cell forward. In addition to actin stress fibers, other actin-driven cellular structures are important for cell motility, such as lamellipodia, as these protrusions will be formed by the actin cytoskeleton in the direction of the movement of the cell, nucleating at the actin-rich cortex. Since actin related processes in astrocytes have been shown to be modulated by hypergravity exposure (see 2.1, 2.4), a transgenic LifeAct-GFP (LAGFP) mouse line was utilized to investigate actin dynamics live in primary astrocytes in hypergravity and an optimized imaging regimen was developed for long-term LAGFP live cell microscopy (see 4.6.4). For these experiments the Hyperscope system was employed as it enables fluorescent live-cell microscopy under hypergravity conditions (see 4.6.4). Primary murine LAGFP transgenic astrocytes were seeded on Ibidi 3.5 cm microscopy dishes and then

imaged in normal gravity and for two hours of 2*g* hypergravity. A time-lapse acquisition with 30-minute intervals of the GFP fluorescence channel enabled an analysis of actin dynamics under hypergravity and a comparison identical individual cells during the alternation in mechanical loading from 1*g* to 2*g*.

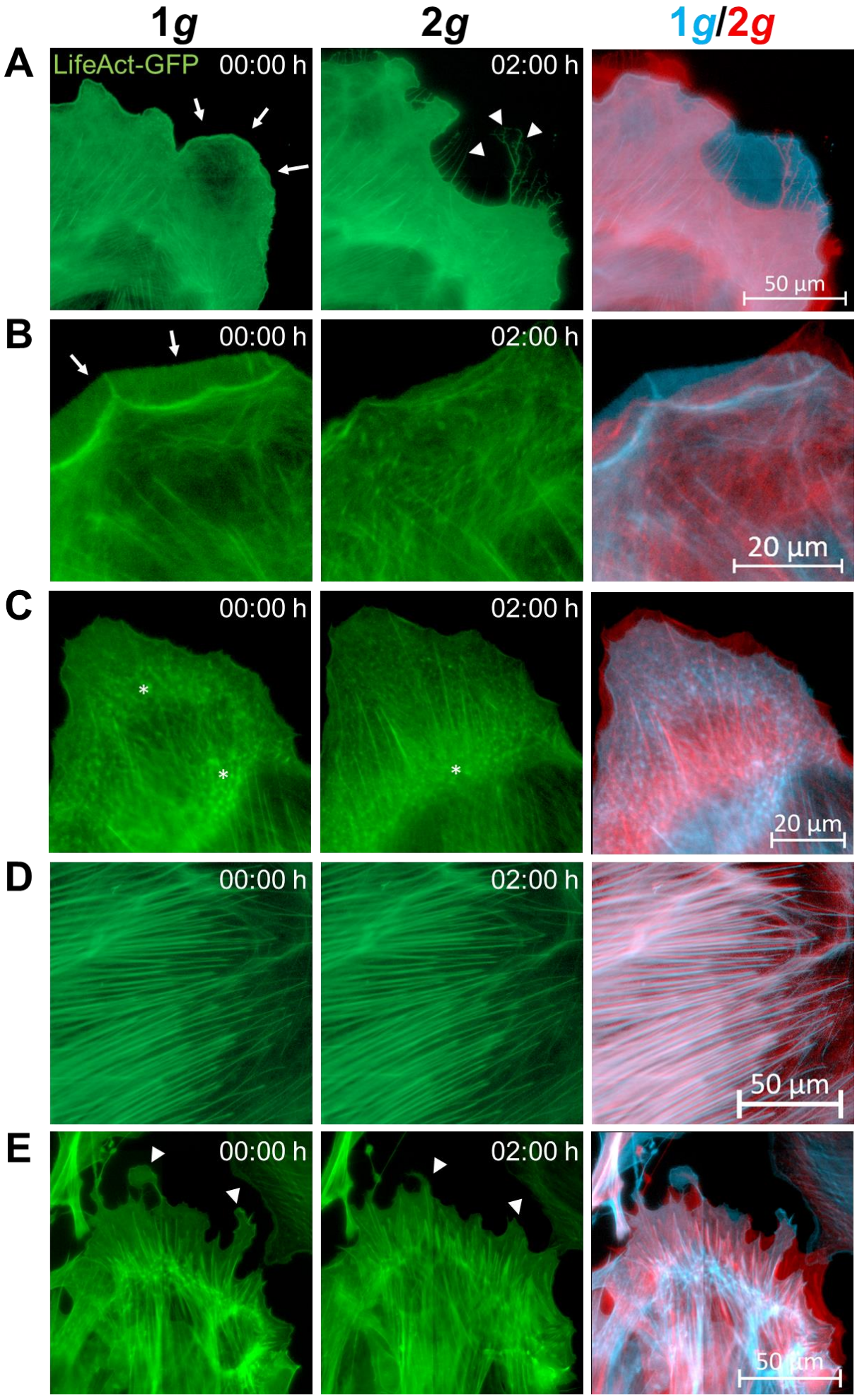
1g
2g
1g/2g
A
LifeAct-GFP
00:00 h
02:00 h
50 µm
B
00:00 h
02:00 h
20 µm
C
00:00 h
02:00 h
20 µm
D
00:00 h
02:00 h
50 µm
E
00:00 h
02:00 h
50 µm

Figure 26: Dynamic changes in F-actin related features in LifeAct-GFP astrocytes due to hypergravity exposure. Shown are several different ROIs of primary murine LAGFP-astrocytes at the start of the experiment in 1*g* (left column) and the identical cell after two hours of hypergravity exposure on the Hyperscope (middle column). Both time points are overlaid with the 1*g* frame in blue and the 2*g* frame in red to compare the structural changes over time (right column). The images in each row show the same ROI with identical settings to be able to evaluate the changes caused by hypergravity exposure. **(A)** A lamellipodium which was clearly visible in 1*g* (arrows) was retracted upon hypergravity exposure, leaving back several retraction fibers (arrowheads). **(B)** Membrane ruffles (arrows) can be seen in 1*g* but not in hypergravity, as the lamellipodium retracted. **(C)** Focal adhesions (asterisks) can be observed in normal- and hypergravity, but in different positions. Further, the actin cortex seemed more pronounced under hypergravity. **(D)** Actin stress fibers were not affected in their number, thickness or parallelism by 2*g* hypergravity. **(E)** Cellular protrusions (arrowheads) retracted during 2*g* hypergravity exposure. Scale bar represents 50 µm (A, D, E) or 20 µm (B, C).

When primary LifeAct-GFP astrocytes were exposed to 2*g* hypergravity for two hours, the retraction of lamellipodia could be observed (see Figure 26A). This phenotype is associated with the general decrease in size and spreading defects ascertained earlier (see 2.1.1). Instead of lamellipodia, retraction fibers were left behind by the fast retraction of the lamellipodial protrusion. Plasma membrane ruffles occurring in normal gravity were seen less often under hypergravity, going hand in hand with the retraction and reorganization of lamellipodia and other cell membrane protrusions (see Figure 26B). Focal adhesions were observed in normal- and hypergravity in and near the actin cortex (see Figure 26C). The change to hypergravity led to a change in the intracellular position of the actin cortex and the focal adhesions, but did not have obvious effects on e.g. focal adhesion number or size. An optical examination of the actin stress fibers in LifeAct-GFP astrocytes in 1*g* and 2*g* did not show any obvious changes between the two gravity levels (see Figure 26D). The number of fibers, the thickness, or parallelism of stress fibers did not visibly change after two hours of hypergravity exposure on the Hyperscope as compared to the same field of view in normal gravity. At several places at the cell perimeter, protrusions could be seen to be retracted upon 2*g* exposure, leading to smoother cell boundaries, and also impacting the total cell area (see Figure 26E).

2.7 Biochemical analysis of reactivity- and migration-related proteins in hypergravity-exposed astrocytes

To more accurately assess the underlying mechanisms of reactivity and migration dynamics of astrocytes influenced by 2*g* hypergravity, the expression of several proteins was analyzed via Western blotting. Primary murine astrocytes from three individual gravid mice were cultured under 2*g* hypergravity conditions inside the MuSIC incubator-centrifuge for up to three days. Every day, samples were retrieved to produce cytoplasmic protein lysates for Western blotting. The relative protein expression between similarly treated 1*g* control samples and the hypergravity sample was compared for each day. For reactivity, antibodies against the intermediate filaments GFAP and vimentin were used. These two intermediate filaments are upregulated in reactive astrocytes, and vimentin also upregulated in scar-forming astrocytes (Nathan and Li 2017). Glial scar formation was shown to be impaired in mice lacking the genes for these two proteins (Pekny, Johansson et al. 1999). To analyze migrational dynamics, RhoA and RhoG were investigated. These RhoA facilitates stress fiber formation which is essential for cellular contractility (Burridge and Guilluy 2016), whereas RhoG is responsible for the formation of lamellipodia and filopodia (Cecile Gauthier-Rouviere 1998). Focal adhesion density was analyzed with an antibody against focal adhesion kinase (FAK).

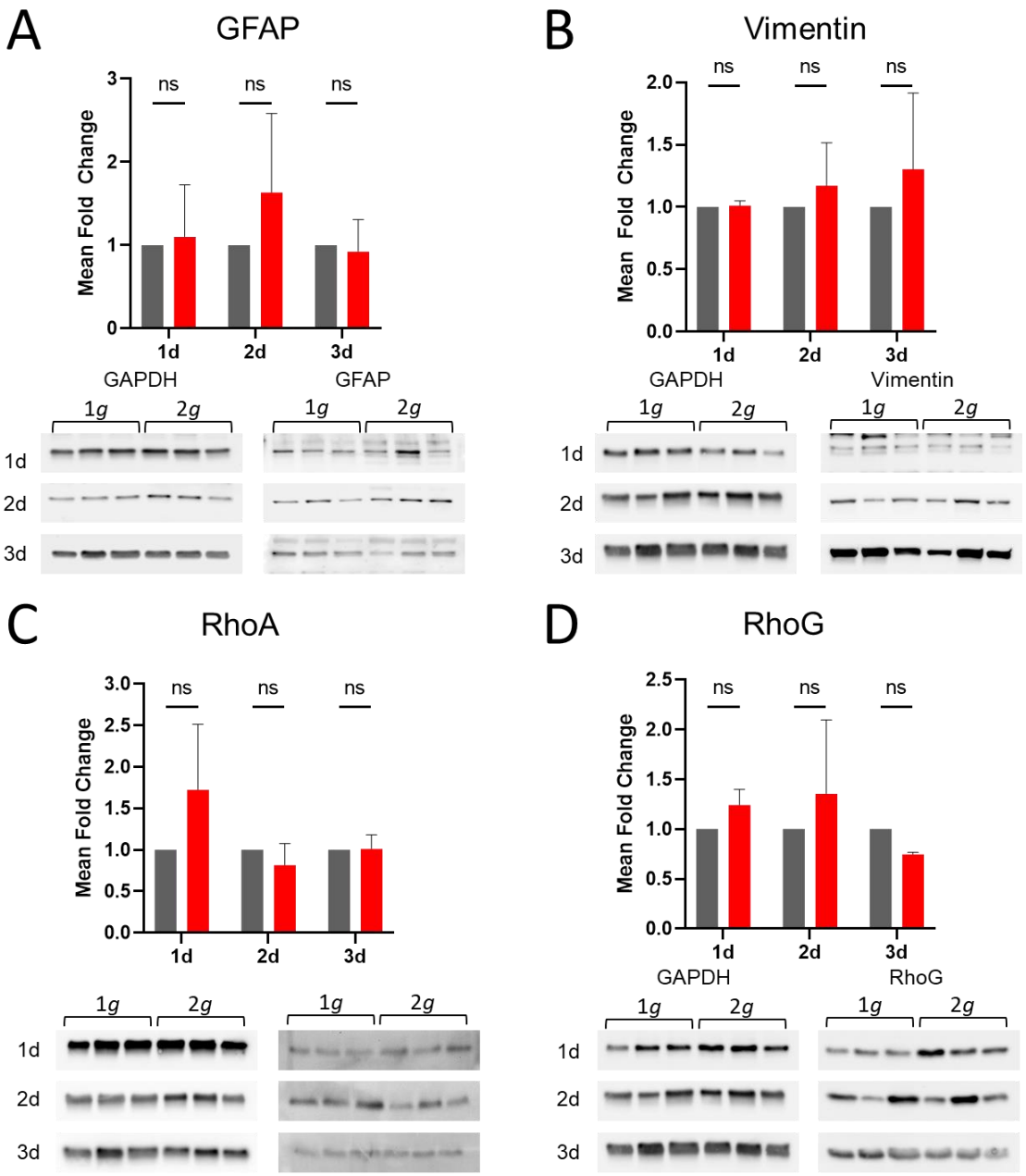
A
GFAP
ns
ns
ns
Mean Fold Change
3
2
1
0
1d
2d
3d
GAPDH
GFAP
1g
2g
1d
2d
3d
B
Vimentin
ns
ns
ns
Mean Fold Change
2.0
1.5
1.0
0.5
0.0
1d
2d
3d
GAPDH
Vimentin
1g
2g
1d
2d
3d
C
RhoA
ns
ns
ns
Mean Fold Change
3.0
2.5
2.0
1.5
1.0
0.5
0.0
1d
2d
3d
1g
2g
1d
2d
3d
D
RhoG
ns
ns
ns
Mean Fold Change
2.5
2.0
1.5
1.0
0.5
0.0
1d
2d
3d
GAPDH
RhoG
1g
2g
1d
2d
3d
E
FAK
ns
ns
ns
1g
2g
Mean Fold Change
1.5
1.0
0.5
0.0
1d
2d
3d
GAPDH
FAK
1g
2g
1d
2d
3d

Figure 27: Western blots of reactivity and migration-related proteins in astrocytes exposed to up to three days of 2*g* hypergravity. Relative protein expression from a densitometric band analysis in 1*g* control samples (grey) and 2*g* hypergravity exposed samples (red). Values depicted in fold-change with SEM from 1*g* to 2*g* after one, two, and three days of exposure for vimentin **(A)**, GFAP **(B)**, RhoA **(C)**, RhoG **(D)**, and FAK **(E).** All values were normalized for the signal intensity of the housekeeping control protein GAPDH. Below each graph the corresponding bands for the measured protein as well as the GAPDH loading control are shown. Sample size n is 3 lysates from 3 individual astrocyte cultures derived from 3 gravid mice. Samples on each day were compared via t-test.

The investigated protein expression levels as analyzed by Western blot were not significantly altered due to 2*g* hypergravity. Individual cultures showed markedly different expression patterns, thus complicating quantitative analysis based on the number of samples.

GFAP has been mentioned before as the most frequently investigated gene to assess astrocyte reactivity state. GFAP protein expression was only slightly and non-significantly increased after the first day of incubation under hypergravity with a fold change of 1.1 ± 0.62 compared to the 1*g* control (see Figure 27A). After two days in hypergravity, GFAP protein expression in the exposed astrocytes was increased non-significantly 1.64 ± 0.95-fold compared to the time matched 1*g* control, but after three days constantly under 2g hypergravity, the expression of GFAP protein was slightly and non-significantly reduced by 0.93 ± 0.38-fold compared to the 1*g* control.

Vimentin is a type IV intermediate filament important for initiation of cell migration, e.g. during reactive astrogliosis and is thus also a marker for reactivity of astrocytes. The expression of vimentin under hypergravity showed a non-significant increase over the three days of exposure (see Figure 27B). After one day of hypergravity exposure, vimentin expression was not increased with a 1.01 ± 0.04-fold change as compared to the 1*g* control. After two days of hypergravity exposure, vimentin protein expression was increased by 1.17 ± 0.35. After three days the fold change nearly doubled the value of the preceding day with a 1.3 ± 0.61-fold increase compared to the time-matched 1*g* control.

Protein levels of the small Rho-GTPase RhoA, which is a central regulator of cytoskeletal rearrangements, were increased non-significantly by 1.72 ± 0.79 after one day of 2*g* hypergravity exposure (see Figure 27C). This increase was only temporary as after two days a 0.82 ± 0.26-fold change in the hypergravity samples was measured and after three days of hypergravity exposure, RhoA expression was close to the 1*g* baseline again with a 1.01 ± 0.17-fold change. Another investigated Rho-GTPase involved in cytoskeletal remodeling is RhoG (see Figure 27D). RhoG protein levels were increased by 1.24 ± 0.16-fold after one day of 2*g* hypergravity exposure. After two days, RhoG was increased by 1.36 ± 0.74-fold. After three days of hypergravity exposure, RhoG protein levels were reduced by 0.75 ± 0.02-fold compared to the 1*g* control at the same day.

Focal adhesions are necessary structures anchoring cells to the substrate and provide the generation of force necessary for cell migration. A central hub in focal adhesion is the focal adhesion kinase (FAK). FAK protein levels were increased by 1.13 ± 0.08-fold after one day

of hypergravity exposure, whereas after two days they were reduced with a 0.84 ± 0.04-fold change compared to the 1*g* control (Fig. 27E). After three days of 2*g* hypergravity exposure, FAK protein expression was increased by 1.32 ± 0.09-fold as compared to the 1*g* control.

2.8 Exposing astrocytes to simulated microgravity on the slide flask clinostat

So far, the current study revealed several important mechanisms involved in increased mechanical loading conditions via hypergravity exposure. One unique form of mechanical unloading or de-coupling is microgravity. Mechanical de-loading is thus required to investigate all aspects of the underlying mechanisms responsible for gravity-sensing.

Reactions to either form of altered gravity are extremely cell type specific and should never be generalized. Assuming the behavior of a model system in microgravity just from observations in hypergravity or the other way around, will most probably lead to misconceptions. Since real microgravity experimental conditions are extremely rare as well as cost and work intensive to achieve, initial studies should be performed in simulated microgravity (s-µg). For adherent cells such as astrocytes, the 2D fast-rotating slide flask clinostat presents a good device to simulate microgravity conditions inside standard incubation environment over several days (see 4.1.3).

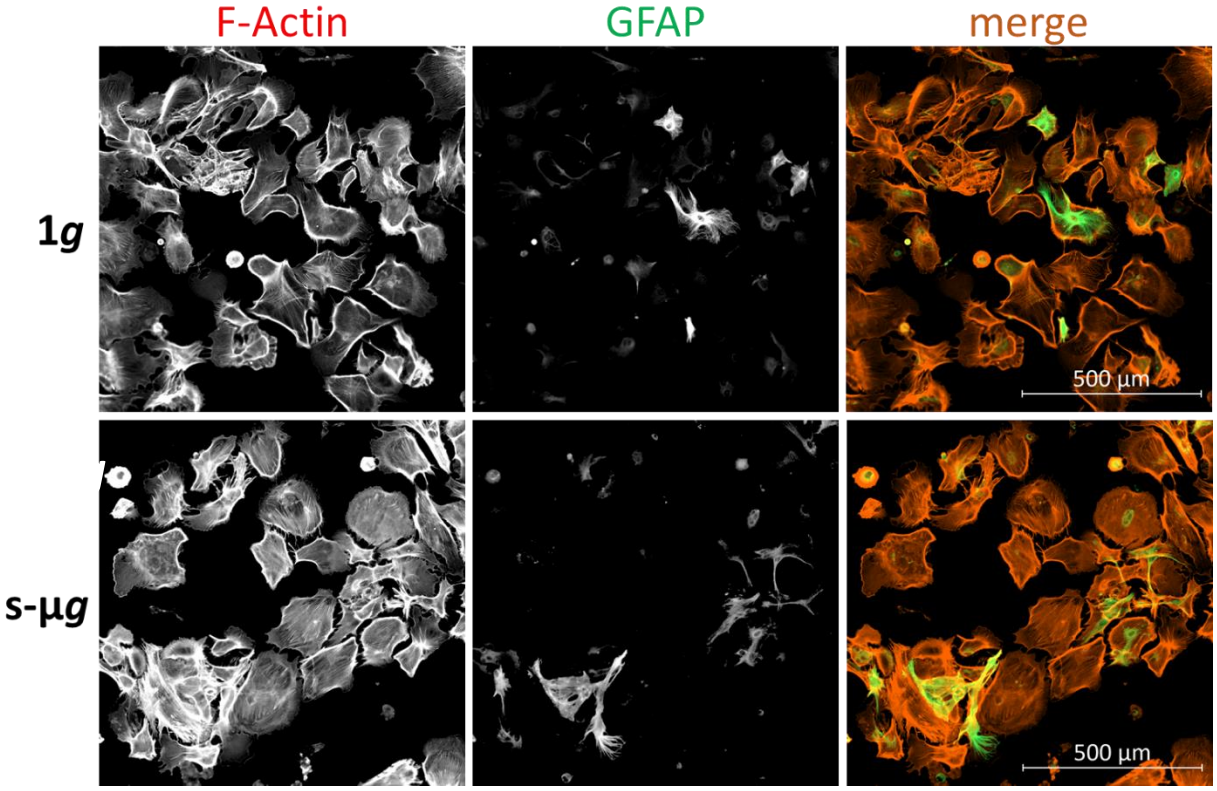

Figure 28: Representative epifluorescence images of primary murine astrocytes after two days of clinorotation (bottom) and the control group at 1*g* (top). Overview of primary astrocytes in vitro after exposure to simulated microgravity compared to 1g control samples. F-actin labelled by fluorescently conjugated Phalloidin is shown in orange and GFAP in green. Scale bar represents 500 µm.

Primary murine astrocytes were seeded in slide flasks, which were filled bubble-free with medium and placed on the slide flask clinostat inside a cell culture incubator. The cells were then exposed to simulated microgravity for up to three days and fixed in 4% PFA at different

time points for analysis. Microscopic image acquisition and therefore also analysis was only done with a 1.6 mm broad region at the center of each slide flask, directly on the rotational axis of the clinostat, as only in this region the highest quality of simulated microgravity can be achieved. Astrocytes exposed to simulated microgravity for two days *in vitro* exhibited similar morphology, growth, and GFAP expression to cells grown in normal gravity (see Figure 28).

2.8.1 Simulated microgravity can modulate astrocyte cell size

Exposing primary murine astrocytes to moderate, physiological levels of hypergravity (2*g*) led to significant decreases in single cell area which can be related to defects in cell spreading and were associated with altered cytoskeletal remodeling (see 2.1.1.1 and 2.1.1.2). To investigate if mechanical unloading has similar or contrary effects on cell morphology, astrocytes were seeded in slide flasks and exposed to simulated microgravity on a slide flask clinostat for three days. At several time points, samples were fixed with 4% PFA and cellular actin was stained using fluorophore-conjugated phalloidin. The slides were then scanned using an epifluorescence microscope and the images were analyzed regarding various morphological parameters. The experiment was repeated three times with independent cell cultures derived from individual mice.

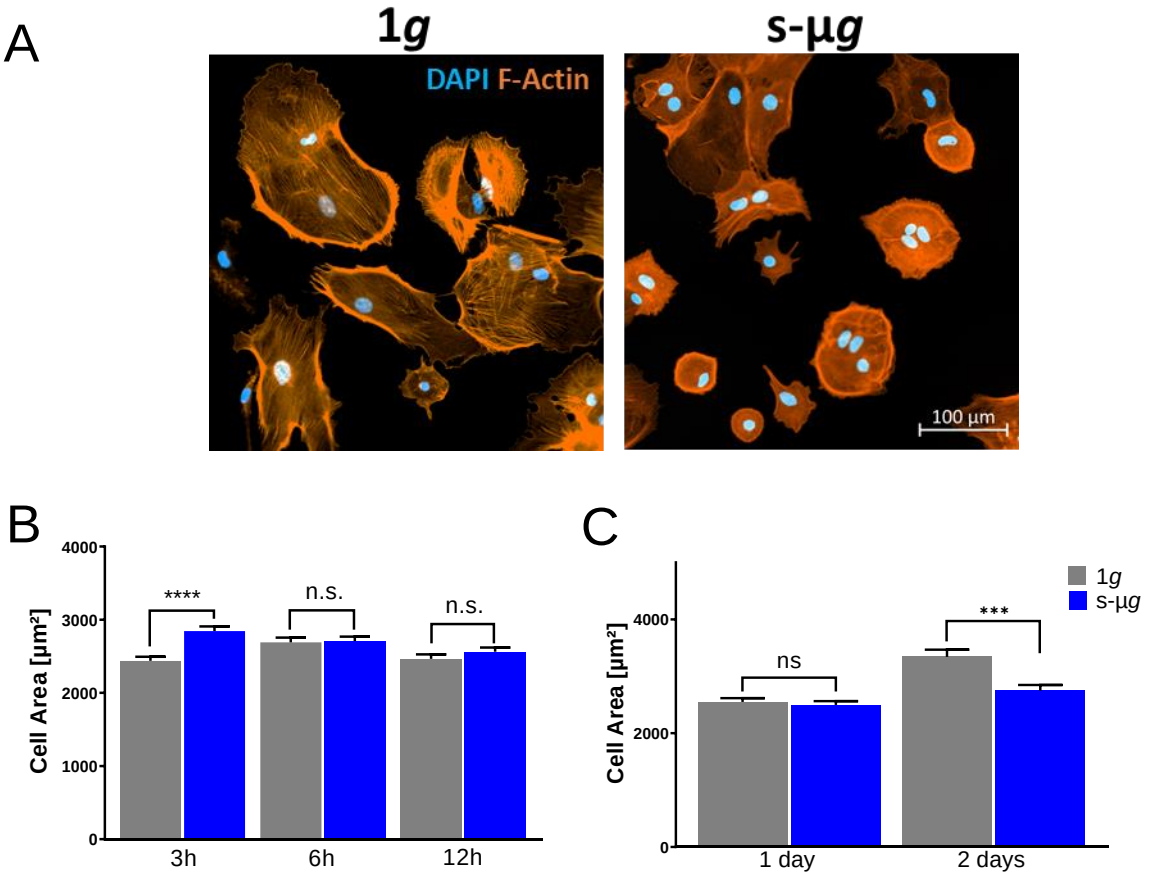

Figure 29: Changes in primary murine astrocyte spreading after simulated microgravity exposure. (A) Representative epifluorescence microscopy images of primary murine astrocytes exposed to two days of simulated microgravity (right) and the 1g control (left). The nuclear DNA dye

DAPI is shown in blue, and F-actin is shown in orange. **(B)** Mean cell area is shown in µm² of astrocytes exposed to 1*g* (grey) and simulated microgravity (blue) for 3h (1*g*: 2438 µm² ± 55 µm², s-µ*g*: 2846 µm² ± 63 µm², $p < 0.0001$), 6h (1*g*: 2690 µm² ± 65 µm², s-µ*g*: 2708 µm² ± 61 µm², $p = 0.8425$), and 12h (1*g*: 2465 µm² ± 60 µm², s-µ*g*: 2562 µm² ± 58 µm², $p = 0.2496$). **(C)** Mean cell area in µm² and SEM of astrocytes exposed to 1*g* (grey) and simulated microgravity (blue) for 1 day (1*g*: 2549 µm² ± 65 µm², s-µ*g*: 2494 µm² ± 67 µm², $p = 0.5758$), and two days (1*g*: 3341 µm² ± 128 µm², s-µ*g*: 1843 µm² ± 100 µm², $p = 0.0004$). Values are shown as SEM. Sample size n is 3h: 1*g*= 604; s-µ*g*= 509, 6h: 1*g*= 463; s-µ*g*= 561, 12h: 1*g*= 485; s-µ*g*= 526, 1 day: 1*g*= 628; s-µ*g*= 644, 2 days: 1*g*= 386; s-µ*g*= 337 cells from 3 individual astrocyte cultures derived from 3 gravid mice.

After exposing primary murine astrocytes to simulated microgravity in a slide flask clinostat for a short duration of three hours, a significant increase in single cell area could be observed in the samples exposed to s-µ*g*, compared to the 1*g* control cells (see Figure 29B). The cell area of astrocytes exposed to simulated microgravity was on average 15% higher (s-µ*g*: 2846 µm² ± 63 µm² vs. 1*g*: 2438 µm² ± 55 µm²). This disparity in cell area between the clinostat and control samples could not be observed after six hours or 12 hours of exposure to simulated microgravity, where no significant difference between the samples was observed. The average cell area of the 1*g* control cells did not significantly change from between three hours and 12 hours, whereas the cells exposed on the clinostat got slightly smaller (3h: 2846 ± 63 µm² to 12h: 2562 µm² ± 58 µm²).

Upon exposure of longer time frames, simulated microgravity exposure had no significant effects on cell size when compared to a 1*g* control after 24h (see Figure 29C). However, after two days of culture on a slide flask clinostat the astrocytes were on average 18% less spread than the 1*g* control cells (1*g*: 3341 µm² ± 128 µm² vs. s-µ*g*: 1843 µm² ± 100 µm²). Both the control as well as the cells cultured on the clinostat showed an increase in average cell area over the two days of the experiment, although the growth or spreading rate of the control cells was higher than that of the s-µ*g* samples. The 1*g* control cells increased their average cell size by 31% from the first to the second day of exposure in contrast to the clinorotated cells which only increased their area by 10% over the same time.

2.8.2 Simulated microgravity exposure leads to changes in Feret ratio of astrocytes

Analogous to previous morphology analyses under hypergravity (see 2.1.1.3), the immunofluorescence microscopy images were used to generate the Feret ratio and measurements of the astrocytes exposed to simulated microgravity. Astrocytes are glial cells that are known to change into a reactive phenotype upon certain, mostly pathological stimuli. One key feature of astrocyte reactivity is their polarization that can be measured by morphological alterations towards a more polarized and stellar appearance. The Feret ratio, calculated from $\frac{FeretMin}{FeretMax}$ gives information about the elongation, i.e. polarization, or compactness of a cell. A Feret ratio approaching 1 means the cell is very compact as the Feret

minimum and maximum are equal, whereas with a decreasing Feret ratio cells get more elongated and polar.

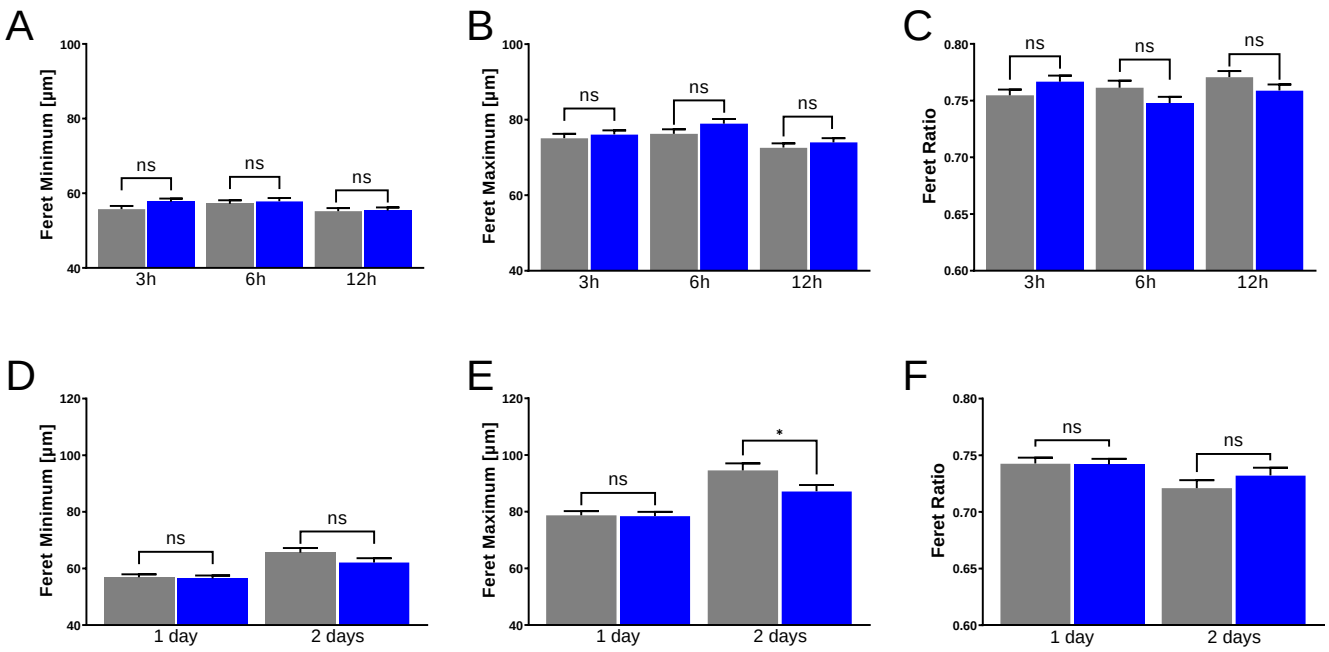

Figure 30: Feret values of primary murine astrocytes after simulated microgravity exposure. Mean Feret minima, maxima and ratios of astrocytes exposed to 1*g* are shown in grey and exposed to simulated microgravity in blue. **(A)** Mean Feret minimum after 3 hours (1*g*: 56 µm ± 0.9 µm, s-µ*g*: 58 µm ± 0.8 µm, p = 0.0931), 6 hours (1*g*: 57 µm ± 0.9 µm, s-µ*g*: 58 µm ± 0.9 µm, p = 0.6002), and 12 hours (1*g*: 55 µm ± 0.9 µm, s-µ*g*: 55 µm ± 0.8 µm, p = 0.8724). **(B)** Mean Feret maximum after 3 hours (1*g*: 75 µm ± 1.1 µm, s-µ*g*: 76 µm ± 1.1 µm, p = 0.5361), 6 hours (1*g*: 76 µm ± 1.2 µm, s-µ*g*: 79 µm ± 1.2 µm, p = 0.1166), and 12 hours (1*g*: 73 µm ± 1.1 µm, s-µ*g*: 74 µm ± 1.1 µm, p = 0.3887). **(C)** Mean Feret ratio after 3 hours (1*g*: 0.76 ± 0.01, s-µ*g*: 0.77 ± 0.01, p = 0.1046), 6 hours (1*g*: 0.76 ± 0.01, s-µ*g*: 0.75 ± 0.01, p = 0.1031), and 12 hours (1*g*: 0.77 ± 0.01, s-µ*g*: 0.76 ± 0.01, p = 0.1205). **(D)** Mean Feret minimum after 1 day (1*g*: 57 µm ± 1 µm, s-µ*g*: 57 µm ± 1 µm, p = 0.7648), and 2 days (1*g*: 66 µm ± 1.6 µm, s-µ*g*: 62 µm ± 1.5 µm, p = 0.1257). **(E)** Mean Feret maximum after 1 day (1*g*: 79 µm ± 1.5 µm, s-µ*g*: 78 µm ± 1.5 µm, p = 0.8902), and 2 days (1*g*: 95 µm ± 2.5 µm, s-µ*g*: 87 µm ± 2.3 µm, p = 0.0285). **(F)** Mean Feret ratio after 1 day (1*g*: 0.74 ± 0.01, s-µ*g*: 0.74 ± 0.01, p = 0.9194), and 2 days (1*g*: 0.72 ± 0.01, s-µ*g*: 0.73 ± 0.01, p = 0.2468). Values are shown as SEM. The sample size n is 3h: 1*g*= 604; s-µ*g*= 509, 6h: 1*g*= 463; s-µ*g*= 561, 12h: 1*g*= 485; s-µ*g*= 526, 1 day: 1*g*= 628; s-µ*g*= 644, 2 days: 1*g*= 386; s-µ*g*= 337 cells from 3 individual astrocyte cultures derived from 3 gravid mice.

When primary murine astrocytes were exposed to simulated microgravity on a slide flask clinostat for 3 - 12 hours, no significant changes in Feret minimum, maximum, or ratio were observed at any time point (see Figure 30A, B, C). A trend was visible, that after three hours of clinorotation, the s-µ*g* exposed cells had a slightly higher Feret ratio, which reversed at the six and 12-hour time point, where the clinorotated cells presented a slightly lower Feret ratio. Over longer periods of clinorotation, the Feret values increasingly diverged from the 1*g* controls. While after one day of s-µ*g* exposure, the Feret minimum, maximum and thus also the ratio were similar to the 1*g* control (see Figure 30D, E, F), after two days of clinorotation the astrocytes displayed a decrease of 6% in average Feret minimum and a significantly lower Feret maximum (- 8%) compared to the normal gravity control. This resulted in a slightly higher

Feret ratio after two days of clinorotation. Both the Feret ratios of 1*g* and s-µ*g* samples decreased steadily from one day to two days in culture.

2.8.3 Slight modulation of cellular circularity by simulated microgravity exposure

The area and polarization of astrocytes changed especially at very early (3h, see 2.8.1) and following prolonged time frames (48h, see 2.8.1, 2.8.2) of exposure to simulated microgravity. To clarify if these phenotypes could potentially be derived from induction of a reactive state, the circularity of the cells was considered as a measure for elongation and polarization induction.

The circularity of a cell is calculated using the Feret maximum and area with the formula $\sqrt{\frac{4 * Area}{\pi * Feret\ Max^2}}$ and was already introduced in a similar protocol with cells under hypergravity (see 2.1.1.4). Hypergravity exposure led to increased circularity after one day, but decreased circularity after two days of exposure, when compared to normal gravity controls. A circularity approaching 1 means the cell has the shape of a circle, and upon decreasing circularity the cells are shaped coarser or more elongated.

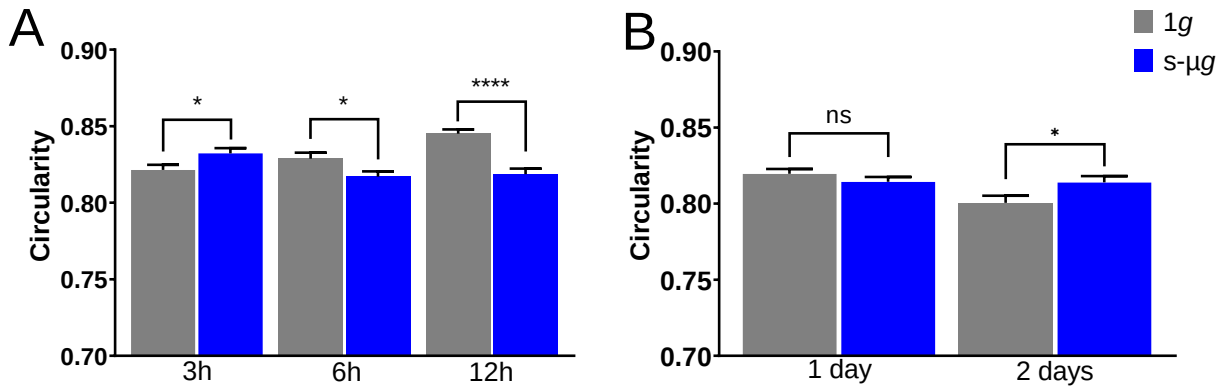

Figure 31: Average circularity of primary murine astrocyte after simulated microgravity exposure. (A) Mean circularity of astrocytes exposed to 1*g* (grey) and simulated microgravity (blue) for 3h (1*g*: 0.82 ± 0.01, s-µ*g*: 0.83 ± 0.01, p = 0.0272), 6h (1*g*: 0.83 ± 0.01, s-µ*g*: 0.82 ± 0.01, p = 0.0237), and 12h (1*g*: 0.80 ± 0.01, s-µ*g*: 0.76 ± 0.01, p < 0.0001). **(B)** Mean circularity and SEM of astrocytes exposed to 1*g* (grey) and simulated microgravity (blue) for 1 day (1*g*: 0.82 ± 0.01, s-µ*g*: 0.81 ± 0.01, p = 0.24), and 2 days (1*g*: 0.80 ± 0.01, s-µ*g*: 0.81 ± 0.01, p = 0.0343). Values are shown with SEM. The sample size n is 3h: 1*g* = 604; s-µ*g* = 509, 6h: 1*g* = 463; s-µ*g* = 561, 12h: 1*g* = 485; s-µ*g* = 526, 1 day: 1*g* = 628; s-µ*g* = 644, 2 days: 1*g* = 386; s-µ*g* = 337cells from 3 individual astrocyte cultures derived from 3 gravid mice.

After exposure to simulated microgravity on a clinostat for up to 48h, primary murine astrocytes showed significant changes in their average circularity compared to 1*g* controls (Figure 31). At the first time point, after three hours of s-µ*g* exposure, there was a small, but significant increase in circularity of the clinostat sample (1*g*: 0.82 ± 0.01, s-µ*g*: 0.83 ± 0.01).

On the contrary, after six hours of s-µ*g*, the cells displayed a lower circularity than the control (1*g*: 0.83 ± 0.01, s-µ*g*: 0.82 ± 0.01) that was more pronounced after 12 hours (1*g*: 0.80 ± 0.01, s-µ*g*: 0.76 ± 0.01). At longer s-µ*g* exposure times, significant changes in cell circularity were less pronounced. After one day both samples had an approximately equal average circularity (see Figure 31B). Two days of simulated microgravity exposure led do a slightly but significantly increased circularity of the clinostat sample, compared to the 1*g* control (1*g*: 0.80 ± 0.01 vs. s-µ*g*: 0.81 ± 0.01). In both conditions, circularity tended to decrease over time. The 1*g* sample had an average circularity of 0.82 ± 0.01 after three hours which decreased to 0.80 ± 0.01 after two days. For the clinostat sample a similar trend was visible, starting with a circularity of 0.83 ± 0.01 at three hours and decreasing to 0.81 ± 0.01 after two days.

2.8.4 Simulated microgravity does not affect astrocyte proliferation

Since a significant reduction in cell size of primary murine astrocytes after one to three days of simulated microgravity exposure was observed (see 2.8.1), it was important to evaluate the proliferation rate of these cells, as a reduction in average cell size could be a sign of decreased cell viability or apoptosis. As stated above, astrocytes have a low proliferative potential. The slide flask clinostat exposed cells were fluorescently stained with an antibody against the antigen Ki67 that exclusively stains the nuclei of proliferating cells. The number of proliferating (KI67-positive) cells was counted and compared in both mechanical loading conditions.

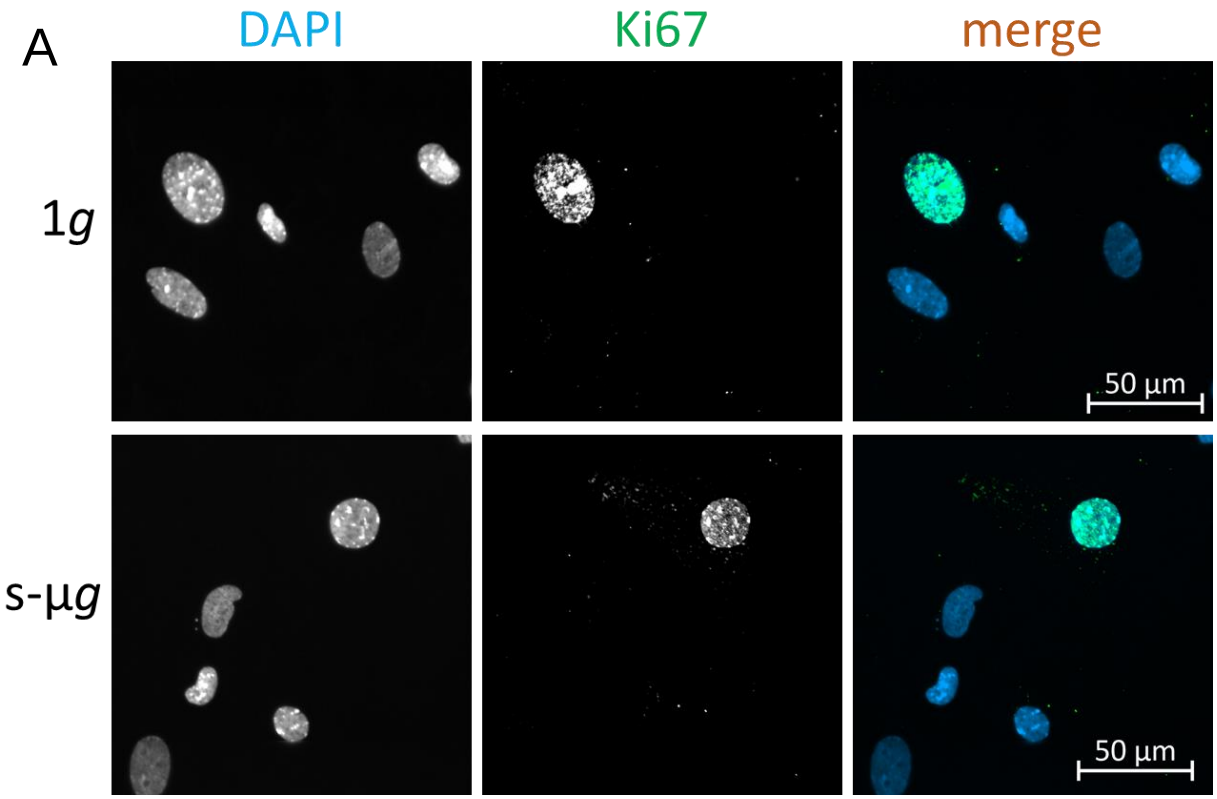

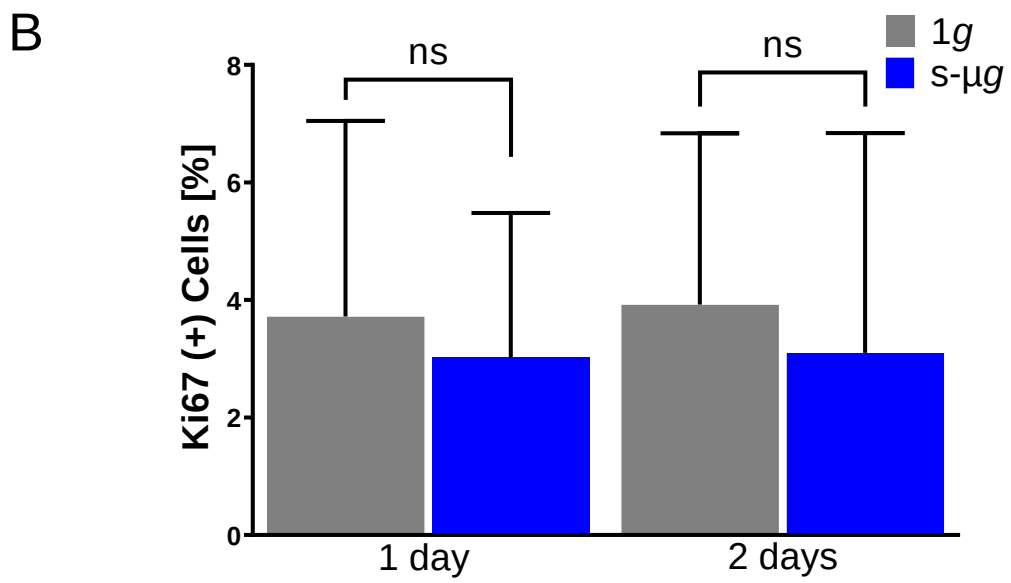

Figure 32: Proliferative astrocytes in simulated microgravity and normal gravity (A) Representative epifluorescence microscopy image of primary murine astrocyte nuclei exposed to two days of simulated microgravity (bottom) and the 1g control (top). **(B)** Shown is the average percentage of Ki67-positive cells for the 1*g* control (grey) and cells exposed to simulated microgravity (blue). Samples were fixated and analyzed after one day (1*g*: 3.72% ± 3.32%, s-µ*g*: 3.02% ± 2.46%, p = 0.8738), and two days (1*g*: 3.92% ± 1.73%, s-µ*g*: 3.10% ± 3.74%, p = 0.8711). For each time point the groups were compared via t-test. Values are shown as SEM. Sample size is n = 3 individual astrocyte cultures derived from 3 gravid mice.

The proliferation rate, as measured by the number of Ki67-positive cells did not show significant changes when exposing primary murine astrocytes to simulated microgravity on the slide flask clinostat (see Figure 32). At all-time points between one and two days of exposure, there was a slight, but not significant decrease of Ki67-positive nuclei following exposure to simulated microgravity compared to the 1*g* control samples.

2.8.5 No changes in GFAP expression after simulated microgravity exposure

The observed modulation of astrocyte size (see 2.8.1), the Feret ratio (see 2.8.2), and circularity (see 2.8.3) after being exposed to simulated microgravity on a slide-flask clinostat could suggest the change to a reactive phenotype induced by decreased mechanical loading. To assert the reactive state of the primary astrocytes, an immunofluorescence staining using an antibody against GFAP was performed. As stated above, GFAP is ubiquitously expressed in astrocytes with highly increased levels in their reactive state. After setting a threshold with the fluorescence intensity scale, GFAP high-expressing and thus reactive cells were counted. Astrocytes were exposed to simulated microgravity and 1*g* normal gravity as a control for 3, 6, 12, 24 and 48h.

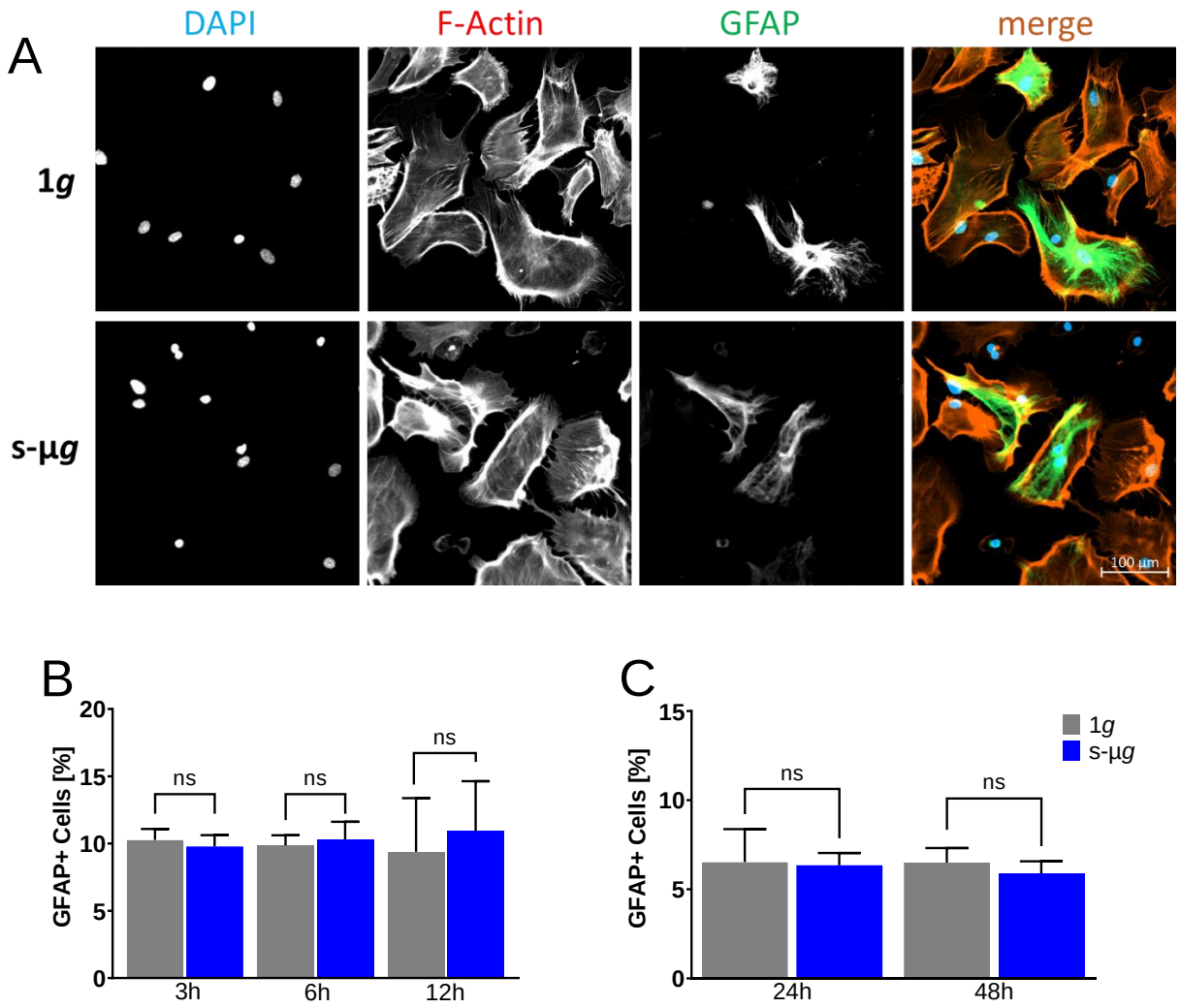

Figure 33: GFAP high-expressing astrocytes after simulated microgravity exposure. (A) Representative epifluorescence microscopy image of astrocytes of the 1*g* control group (top) and after 2 days of simulated microgravity exposure (bottom). Only few cells express a high level of GFAP indicated by a fluorescence signal above the threshold**. (B)** The percentage of cells with a GFAP immunofluorescence signal above threshold and a pronounced intermediate filament network. Shown is the average percentage of reactive cells in the 1*g* control (grey) and the simulated microgravity sample (blue). Samples were analyzed after three hours (1*g*: 10.27% ± 0.8%, s-µ*g*: 9.78% ± 0.8%, p = 0.6988), six hours (1*g*: 9.87% ± 0.7%, s-µ*g*: 10.29% ± 1.3%, p = 0.8075), and 12 hours (1*g*: 9.39% ± 4%, s-µ*g*: 10.93% ± 3.7%, p = 0.8042). **(C)** Identical analysis following longer duration incubations at 1*g* normal gravity or simulated microgravity. Shown are the results after 24 hours (1*g*: 6.53% ± 1.6%, s-µ*g*: 6.35% ± 0.6%, p = 0.9316), and 48 hours (1*g*: 6.50% ± 0.7%, s-µ*g*: 5.90% ± 0.6%, p = 0.6042). All time points for both conditions were compared via t-test. The sample size is n = 3 individual astrocyte cultures derived from 3 gravid mice.

The reactivity state of primary murine astrocytes after simulated microgravity exposure was analyzed by GFAP immunostaining (see Figure 33, 4.5.2). No significant change in the number of GFAP positive cells could be detected at any time point between three hours and two days of clinorotation. During the first 12 hours of the experiment, between 9.39% ± 4% at s-µ*g* and 10.29% ± 1.3% at 1*g* of cells were counted as GFAP positive, whereas after one to two days the average percentage of GFAP positive cells dropped to numbers between 5.90% ± 0.6% at s-µ*g* and 6.53% ± 1.6% at 1*g*. The cells which were exposed to mechanical unloading on the

clinostat displayed a slightly increasing number of GFAP-positive cells from 3h to 12h (see Figure 33B). The control cells grown in 1*g* exhibited a slightly decreasing number of GFAP-positive cells over the same time frame. However, when exposed to simulated microgravity on the clinostat for longer times of 24 and 48 hours, astrocytes displayed slightly decreased numbers of GFAP-upregulated cells as compared to 1*g* controls, with a declining trend visible (see Figure 33C). Astrocytes in both conditions became less reactive from 3h to 48h.

2.8.6 Microtubule stability is not impaired by short-term simulated microgravity

Different investigators found the intracellular microtubule network to be disrupted in mammalian cells after simulated or real microgravity exposure (Marian Lewis 1998, Schatten, Lewis et al. 2001, Xue, Li et al. 2017, Nassef, Kopp et al. 2019). To find out if the tubulin cytoskeleton is compromised in primary murine astrocytes exposed to simulated microgravity, cells were clinorotated in slide flasks for three to 12 hours and immunostained with an antibody against α-tubulin. The samples were then imaged with an epifluorescence microscope and the state of the tubulin network inside single cells was grouped into three distinct categories, depending on if the stained microtubules presented a well-defined network, only a few well-defined microtubules were visible, or only a diffuse cloud was visible in the immunostaining (see Figure 34, 4.8.9).

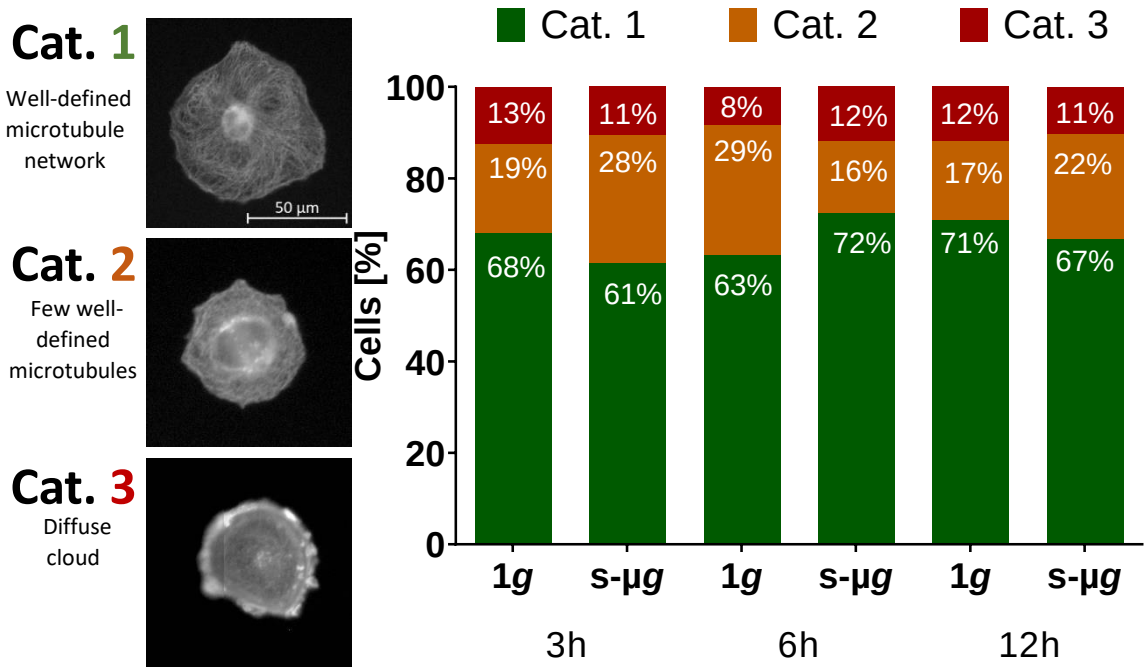

Figure 34: Categorization of microtubule network state in primary murine astrocytes exposed to simulated microgravity. Primary murine astrocytes were stained with an α-tubulin antibody and imaged on an epifluorescence microscope. Cells exposed to simulated microgravity for three, six and 12 hours were compared to 1*g* control cells and grouped into three categories (Cat. 1 – 3) depending on the state of their intracellular microtubule networks. Between 50 and 100 single cells per time point and replicate were assigned to one of the three categories. Samples were analyzed after three hours,

six hours, and 12 hours of simulated microgravity exposure and compared to a 1*g* control (**3h:** 1*g*: Cat. 1 = 68% ± 7%, Cat. 2 = 19% ± 4%, Cat. 3 = 12% ± 3%; s-µ*g*: Cat. 1 = 61% ± 13%, Cat. 2 = 28% ± 8%, Cat. 3 = 11% ± 5%; **6h:** 1*g*: Cat. 1 = 63% ± 10%, Cat. 2 = 29% ± 7%, Cat. 3 = 8% ± 3%; s-µ*g*: Cat. 1 = 72% ± 14%, Cat. 2 = 16% ± 7%, Cat. 3 = 12% ± 7%; **12h:** 1*g*: Cat. 1 = 71% ± 11%, Cat. 2 = 17% ± 1%, Cat. 3 = 12% ± 10%; s-µ*g*: Cat. 1 = 67% ± 1%, Cat. 2 = 22% ± 1%, Cat. 3 = 11% ± 3%). Sample size is n = 3 individual astrocyte cultures derived from 3 gravid mice.

Cytoskeletal network states of all categories could be observed in both conditions. Dystrophic microtubule networks were equally present (8-13%) in murine astrocytes exposed to three to 12 hours of simulated microgravity compared to time-matched 1*g* controls (see Figure 34). Astrocytes with only a few well-defined microtubules (assigned to category two) were increased after three hours of clinorotation (28% ± 8%) in comparison to the 1*g* control sample after the same time (19% ± 4%). This difference was inverted in cells assigned to category two. Astrocytes control cells showed the highest rate of any sample (29% ± 7%) after 6h in comparison to the simulated microgravity sample which had the lowest measured fraction of category two cells in this experiment (16% ± 7%). This difference in cells assigned to category two with a certain degree of undefined networks properties was not stable. After 12h the fraction of cells with undefined microtubules was inverted compared to the 6h time point with 17% ± 1% at 1*g* and 22% ± 1% in s-µ*g*.

3. Discussion

In this thesis, primary embryonal murine astrocytes were exposed to altered gravity, ranging from simulated microgravity to 10*g* hypergravity, and their cytoskeletal dynamics, reactivity state, as well as migratory behavior and viability were analyzed and compared to normal gravity (1*g*) controls. Astrocytes have a multitude of functions in the healthy CNS, including formation of the blood-brain barrier, nutrient supply to neurons and neurotransmitter clearance as well as synaptic regulation. In case of an injury (e.g., traumatic brain injury, spinal cord injury) or disease (e.g., neurodegenerative diseases, stroke, or epileptic seizures) in the neuronal tissue, astrocytes become reactive and, through a process called astrogliosis, form the glial scar. This scar tissue is crucial for wound closure and isolation of damaged tissue but is often persistent and prevents neuronal regeneration in the area of the scarring which leads to permanent impairments of the patient.

Here, primary astrocytes were used as a physiologically relevant model system for astrocyte reactivity, as they exist in a naive state and can also become reactive. This is in contrast to glioma-derived astrocyte cell lines such as U373 which do not exhibit clearly defined naive or reactive states and are often unusually proliferative, expressing high amounts of reactivity marker proteins such as the intermediate filament GFAP, rendering these cells unsuitable for studies of processes which would be relevant *in vivo*. Primary astrocytes were exposed to altered gravity conditions by various centrifugation profiles as well as clinorotation regimens. It is known that cellular mechanisms, such as cytoskeletal dynamics and gene expression can be modulated by mechanical loading through hypergravity and mechanical unloading by simulated microgravity exposure. As shown in this thesis, the reactivity state of primary astrocytes could be influenced by the applied non-invasive stimuli of gravitational loading alterations. Thus, it might be possible to attenuate but not fully prevent astrocyte reactivity and possibly further even glial scar formation. If the underlying pathway of this mechanism can be unraveled, it could be used as novel target for the therapy of CNS injuries and diseases.

3.1 Hypergravity exposure affects astrocyte spreading and morphology related to astrogliosis

Primary murine cortical astrocytes were exposed to 2*g* of hypergravity to investigate their reaction to physiological levels of hypergravity, which means levels easily tolerated by humans and other mammals such as mice. These forces are also endured by astronauts during the launch into orbit to the International Space Station, where they experience g-loads of 2*g* to 4*g* for 5 minutes (arianespace 2012, Frett, Petrat et al. 2015, Tominari, Ichimaru et al. 2019).

The first step in the characterization of effects of increased gravitational loading on an astrocyte cell culture was to observe the cells in normal and hypergravity and compare their

morphology. In contrast to their finely branched, star-like shape *in vivo*, astrocytes in a standard 2D *in vitro* cell culture appear as flat and thinly spread cells with varying shapes, sometimes polarized or more circular (Schildge, Bohrer et al. 2013). This observation also held true when exposing astrocytes on glass coverslips to 2*g* hypergravity, as the cells did not become severely morphologically altered or even dystrophic after prolonged periods of hypergravity exposure, compared to the 1*g* control (see Figure 13A). In addition, the intermediate filament GFAP has been stained as a well-established astrocyte marker protein (Sofroniew and Vinters 2010). Hence, the employed culturing methods produced a very pure and viable population of murine astrocytes.

Astrocyte spreading was investigated in detail since cultured astrocytes are known to show majorly enlarged cell somata compared to stellate and star-shaped astrocytes *in vivo* in nervous tissues. This spreading phenotype is a prerequisite for the establishment of e.g., cell-cell or cell-substrate contacts and further to initiate migratory movements. Therefore, both initial as well as consistent and long-term spreading were taken into account. Cytoskeletal mechanisms associated with spreading and migration are also important for astrocyte reactivity, as astrocytes *in vivo* show hypertrophic phenotypes and increased migration in astrogliosis.

Live assessment of dynamic processes, such as cell spreading, cytoskeletal rearrangements or migratory behavior required a specialized microscope setup that was developed and established during the course of this thesis. The Hyperscope is a fully automated epifluorescent live-cell imaging microscope installed on the short-arm human centrifuge within the DLR :envihab facility (Cologne, Germany). It can be controlled, and live-feedback be acquired while the centrifugation regimen is running, to record live-cell microscopy images in hypergravity (see Figure 2).

For the initial spreading analysis, astrocytes were trypsinized and seeded on an Ibidi 8-well slide (see 4.2.3.1). Images were acquired with the Hyperscope at 30-minute intervals for 5h and analyzed with the image analysis suite of the Zeiss Zen software. With this method, the speed of the initial spreading in normal and hypergravity could be determined (see 2.1.1.1). As a result, the spreading rate in the first five hours after seeding was significantly impaired in astrocytes when they were exposed to 2*g* hypergravity. Interestingly, both the 1*g* and 2*g* growth curves matched a linear regression, indicating that the cell spreading, at least in the observed timeframe, is a linear process of cell area increase. After five hours, astrocytes exposed to hypergravity were on average 45% less spread than the 1*g* control cells. The first time points of the 2*g* sample in the graph were lower than those of the 1*g* control, which leads to the question why the cells were potentially already smaller at the start of the experiment. This is most probably an artefact related to the imaging procedure, as the hypergravity exposure on the centrifuge led to a focus shift, through which the cell perimeter could have

been slightly out of focus, especially when the cells were still largely globular. This effect can also be seen in Figure 12A, but does not affect the calculation of the spreading velocity.

To observe, if the reduction in spreading under hypergravity was only apparent in the initial spreading or also in later life cycles of the cells, astrocytes were further exposed to 2*g* hypergravity for one day, two days, and longer inside the incubator centrifuge MuSIC (see 2.1.1.2). Changes in spreading rates only observed in initial phases would point towards effects related to cell attachment to the substrate rather than to cell intrinsic mechanisms that would be affected also during later phases of continuous exposure to altered mechanical loading. After one and two days, samples were removed from the centrifuge and immediately chemically fixated. A staining with fluorophore-conjugated Phalloidin to visualize F-actin was performed to identify cells and further epifluorescence microscopy and analysis with Zeiss Zen resulted in a dataset with several morphological parameters for every single cell in the samples. Cell size analysis revealed a hypergravity-reduced spreading samples exposed for one- and two-day periods, as the cell size of the hypergravity samples was significantly reduced by 21% after one day and by 18% after two days of exposure.

It is to note, that even under hypergravity exposure, the astrocytes continued to grow over the course of the experiment. Both the control as well as the hypergravity sample showed an increase in cell size from one day to two days by 46% and 50% respectively. Thus, the exposure of already spread cells as performed in 2.1.1.2 seemed to lead to a reduction of cell size in the first day of exposure which persisted afterwards but did not further increase in its effect over time. This could have been caused by an adaptation of astrocytes to hypergravity and will be further discussed in 3.5. The reduction in cell area persisted for up to five days of hypergravity exposure, which was the longest hypergravity exposure experiment done with this readout. Intriguingly, the initial cell spreading was much more strongly affected by hypergravity exposure (45% reduction after five hours), compared to the reduction seen when cells that had already adhered and spread to an extent were exposed to hypergravity for one and two days (21% and 18% reduction respectively). This might hint to dynamic processes of adaptation to hypergravity after some time of exposure, but could also in part be caused by the different methods used to generate this data: after five hours of initial spreading in normal gravity the astrocytes reached an average cell area of 3518 µm² and the 2*g* hypergravity sample reached an average cell size of 1576 µm² (see Figure 12C). In contrast to this, after 24 hours of cultivation the astrocytes of the control sample measured on average 2320 µm² and the cells that were exposed to hypergravity measured 1839 µm² (see Figure 13C). Logically, the cells should have a larger average cell size after 24 hours of cultivation than after the five hours of initial spreading. The explanation for this discrepancy in measured cell sizes lies in the different acquisition and analysis methods used to generate these two data sets. For the initial spreading analysis, astrocytes were hand-picked because only cells that adhered

and started to spread right at the beginning of the experiment could be counted, and their spreading be analyzed for the full five-hour duration. This led to the selection of especially quickly spreading cells, since cells that adhered at later time points and started to spread later in the experiment, thus inhibiting a slower spreading speed, were not analyzed. In contrast to this, for the 24- and 48-hour time points, all cells on the coverslip were analyzed (down to a cut-off of 200 µm² to exclude debris and dead cells). For this reason, the inherent variability in spreading states and cell sizes was far larger for this experiment and caused a lower average cell size to be reported for the 24-hour time point both in the control and in the hypergravity sample. Due to this fact, the stronger effect of hypergravity on the initial spreading compared to the long-term effects after one and two days might be overrepresented, suggesting that the initial and long-term spreading reduction due to hypergravity is more alike than it is suggested by the data. Another factor to keep in mind is that all of the performed analyses were done by observing a two-dimensional image of the cells. A reduction in cell area might be caused either by a decrease in total cell area and thus cell size, or it might be caused by the cells becoming more spherical in a three-dimensional view, thereby decreasing their footprint but keeping an equal cell volume. Further volumetric analyses such as z-stacking in a laser scanning microscope might be necessary to account for these potential effects.

From the dataset generated in 2.1.1.2, not only cell size but also several other morphological parameters regarding the cell shape could be derived. This was possible because the staining for F-actin made it possible to accurately map the cell perimeter where F-actin is naturally enriched in structures such as lamellipodia, filopodia and the actin cortex. The first features that were analyzed were the Feret measurements (see 2.1.1.3). The analysis of these values indicated that the Feret minimum and maximum were both significantly reduced after one- and two-day hypergravity exposure. The Feret ratio on the other hand was not significantly reduced in astrocytes exposed to hypergravity; after one day of hypergravity exposure a slight increase in the Feret ratio of the hypergravity sample and after two days of exposure a small decrease was observed. This discrepancy between the Feret values and ratio can be explained by the general reduction in cell size under hypergravity established in 2.1.1.2. Since the same dataset was used, the Feret minimum and maximum decreased in the same magnitude as the general cell size, leading to equal Feret ratios in the control and hypergravity samples. From these results one can conclude that no measurable elongation or increase in cell compactness was caused by hypergravity exposure.

Cell circularity (see 2.1.1.4) analysis showed a small but significant increase in circularity by 1.3% after one day of hypergravity exposure. After two days of hypergravity, the exposed cells exhibited a significantly decreased circularity by 1.1%. Both samples, the control and the hypergravity sample, showed a decrease in circularity from one to two days. This can be attributed to an increase in cell polarization by the protrusion of lamellipodia or also more

filopodia or other membrane processes that have been extruded in this time, since the cells tend to settle in over several days after seeding and after adhering start to e.g. migrate and proliferate. In the fluorescence images, such incremental changes in the amount of either filopodia or lamellipodia could not be observed, which is why the exact reason for the changes in circularity are still unclear.

The observed changes are critical for future treatments of glial scarring and CNS-injury, since hypertrophy and spreading of reactive and scar forming astrocytes are some of the main mechanisms in astrogliosis. A decrease in astrocyte cell size by about 20%, as seen after 2*g* exposure, could have a significant impact on the severity of the astrocyte reactivity and reduce negative outcomes and permanent CNS scarring when replicated *in vivo*. Key players in cell spreading are the different components of the cytoskeleton, mainly actin fibers and motor proteins. The observed impairment of cell spreading might therefore be caused by an influence of hypergravity on these cytoskeletal proteins and was further investigated by means of STED and live-cell microscopy as well as biochemical analyses.

3.2 Cell viability and proliferation are not affected by hypergravity exposure

When exposing cells to a new stimulus, it is important to control for unwanted effects that might harm the cells or the organism on a physiological level, especially since hypergravity exposure can be seen as a stress factor for cells. Primary murine astrocytes were exposed to 2*g* hypergravity in the MuSIC for up to two days with samples taken at several time points for proliferation and apoptosis assays (see 2.1.1.5). The programmed cell death apoptosis is an important factor in every multicellular organism or tissue. Unhealthy or damaged cells are disassembled in a controlled manner, preventing the release of harmful cytokines or other cell debris and ensuring tissue homeostasis. Low, but steady levels of apoptosis are thus expected in most tissues. Pure astrocyte cultures typically exhibit low levels of apoptosis, stemming from an equally low rate of cell proliferation. Necrotic cells which did not undergo the strictly controlled apoptosis pathway but died as a result of mechanic injuries or other harmful environmental factors are expected to be present in even fewer numbers. Apoptosis and necrosis levels were evaluated by Annexin V / PI staining and resulted in no difference in cell viability between the hypergravity sample and the static 1*g* control (see Figure 16). The fraction of apoptotic cells in both conditions was below 3%, and the part of necrotic cells was below 0.9%. Consequently, hypergravity exposure of 2*g* does not harm astrocytes in a way which would decrease cell viability.

Cellular proliferation is the process of mitosis in which a eukaryotic cell replicates their DNA and splits into two daughter cells. Proliferation and apoptosis are balanced in healthy tissue to retain tissue homeostasis. Astrocytes in cell culture are proliferating very slowly in contrast to

other cell lines, which nicely represents the situation of astrocytes in the CNS *in vivo.* Astrocyte proliferation was assessed using a Ki67 fluorescence staining, which stains the nuclei of cells that are in an active phase of the cell cycle. As a result, between 4.6% and 4.2% of astrocyte nuclei were stained positively for Ki67 at the 6-hour time point, and between 3.5% and 3.4% after 48 hours, with no significant difference between the hypergravity sample and the control group. The fraction of proliferating cells decreased under both conditions from the start of the experiment until the 48-hour time point, which was caused by growth medium depletion over time and a general aging of the cell culture.

These results prove that there is no harm for astrocytes in culture and potentially for mice and humans when exposing them to moderate intensities of hypergravity. An elevation in cell death would have been critical since this could lead to tissue damage or elevated astrocyte reactivity in the brain and CNS. A decrease in astrocyte proliferation could equally lead to tissue atrophy, whereas an increase in proliferative signaling, as well as a resistance to cell death are both hallmarks of cancer (Hanahan and Weinberg 2011). In correlation with astrogliosis *in vivo*, where reactive astrocytes have hyperproliferative properties that further increase when forming the scar tissue, the attained results that astrocytes under hypergravity do not increase baseline proliferation rates are promising for future therapeutic approaches. In future experiments, it will be interesting to see how strongly reactive astrocytes react to hypergravity and if their increased proliferation could be reduced by hypergravity exposure. Controlling of cell viability also ensures that the following experiments are not influenced by altered apoptosis or proliferation and all findings are caused due to hypergravity exposure.

3.3 Astrocyte reactivity reduced by hypergravity exposure

Astrocytes in the healthy CNS change their phenotype and become reactive in case of an injury or illness (see 1.2.2). This reactive phenotype is accompanied by morphological and behavioral changes such as hypertrophy, hyperproliferation and increased migration and is usually identified by the upregulation of various molecular markers such as GFAP (Sofroniew and Vinters 2010). A clear distinction between reactive and non-reactive astrocytes is not possible since different reactive astrocyte populations express varying markers and astrocyte reactivity encompasses many different states and severities (Sofroniew 2009). Here, antibodies against the intermediate filaments GFAP, nestin and vimentin and against Leucin Zipper Kinase (LZK) were used in a fluorescence microscopy assay to determine the relative protein quantity in up to 120 hours hypergravity exposed cells and control cells (see 2.2). GFAP, the most established astrocyte marker is known to be generally expressed in astrocytes, but its expression is highly increased in reactive astrocytes. In the astrocyte culture used here, two general phenotypes of GFAP expression could be seen. Most cells expressed GFAP in a weak baseline intensity, and some cells presented an intense, clearly structured

intracellular GFAP filament network (see Figure 18A). These two populations represented normal naive astrocytes and reactive astrocytes respectively. As a first assay, the number of reactive cells which expressed a clearly defined GFAP filament network (GFAP (+) cells) were counted and compared to the fraction of naive, baseline-GFAP expressing cells. At the first time point, 7.7% of cells in the hypergravity sample were GFAP (+), versus 9.3% of cells in the control group. At all time points, the control group contained more GFAP (+) cells than the hypergravity samples, and both groups showed a peak in GFAP (+) cells after 48 hours in the assay, after which the fraction of GFAP expressing cells decreased again. These are promising results, since they demonstrate that hypergravity exposure does not increase the amount of GFAP-positive, and thus reactive cells, and might even be responsible for a generally lower reactivity in the cell culture. This finding corroborates prior observations in pregnant rats, where GFAP expression of the embryonic brain was reduced after six and up to 21 days of 1.5*g* hypergravity exposure *in utero* (Sulkowski, Li et al. 2004). In this thesis, the peaking of GFAP (+) cells around the 48-hour time point in both the 2*g*, as well as the 1*g* condition might be attributed to a depletion of nutrients in the growth medium since no medium exchange could be performed inside the MuSIC-centrifuge, which might lead to environmental stress on the astrocytes.

The average fluorescence intensity for GFAP, LZK, vimentin and nestin in astrocytes was compared between hypergravity and 1*g* control samples (see Figure 19 and Supplementary Figure 1 and Supplementary Figure 2) and revealed no difference between both conditions at the start of the experiment, in contrast to the preceding binary analysis of GFAP (+) cells. GFAP fluorescence intensity peaked at the 48-hour time point and was generally decreased in the hypergravity exposed samples between the 12- and 96-hour time points. However, a Mann-Whitney comparison in the complete course of both conditions did not show a significant divergence of the two curves, as both the start and endpoints showed very similar expression levels and the divergence was most prominent following 48h of exposure. At this time, the GFAP fluorescence in the hypergravity samples was app. 29% lower than in the 1*g* controls.

The LZK fluorescence intensity behaved similarly to GFAP, with slightly lower values for the hypergravity sample and a peak after 48 hours but no significant difference. Vimentin fluorescence was always significantly lower in the hypergravity exposed cells, as well as Nestin fluorescence intensities were also lower at any time point, although in this case the samples had a large standard error of the mean which overlapped at all time points.

All investigated reactivity markers showed a decreased fluorescence intensity under hypergravity exposure. Thus, it can be speculated, that 2*g* exposure lowers the naive reactivity of cultured astrocytes.

3.4 Nuclear morphology unchanged by hypergravity exposure

The transcription of DNA in the cell nucleus and the downstream translation of mRNA into proteins relies on dynamic reorganization of the nuclear DNA for gene expression. Accordingly, the nucleus is a plastic structure that can be subjected to dynamic changes in form and shape. Especially in the context of widespread changes in gene expression and protein synthesis that are associated with astrocytes becoming reactive, nucleus morphology should be taken into account, coming either from within the nucleus itself or mediated by its surroundings (Skinner and Johnson 2017). The nucleus is considered to be a candidate functioning as a mechanosensory structure in mammalian cells, since it is connected to perinuclear actin fibers and intermediate filaments. Mechanical forces exerted on the cell are known to cause changes in the structure of the nuclear lamina and chromatin organization (Kirby and Lammerding 2018). Indeed, in real microgravity conditions where cells are subjected to mechanical unloading, an elongation of cell nuclei was observed in C2C12 myocytes, hinting to its role as a mechanosensor (Hughes-Fulford 2003).

Astrocyte nuclei of 1*g* controls and of samples after one and two days of 2*g* centrifugation in the MuSIC were stained with DAPI and analyzed using the Zeiss Zen image processing suite (see 2.3). No significant alterations in nuclear area and diameter were observed between the conditions (see Figure 20A, B). Both the hypergravity exposed and the control nuclei became smaller between the first and second day of observation by 26% and 29% respectively, confirming that hypergravity exposure does not cause nuclear hypertrophy in astrocytes. The circularity of the nuclei was not affected by hypergravity exposure either (see Figure 20C). After one day of hypergravity exposure, no changes in the Feret measurements were recorded. However, at the second day, the hypergravity exposed cells exhibited nuclei with a higher Feret minimum than the control group, which subsequently led to a higher Feret ratio in the exposed cells' nuclei (see Figure 20D, E, F). This means that astrocyte nuclei exposed to 2*g* hypergravity for two days were less elongated than the controls, whereas real microgravity exposure caused elongated nuclei in C2C12 cells (Hughes-Fulford 2003). This observation could potentially be connected to experiments done with mesenchymal stem cells, which were grown on stiff and soft matrices, causing cytoskeletal tension which is transmitted to the nucleus and thus modulates lamin phosphorylation status (Buxboim, Swift et al. 2014). This in turn leads to a softening of the nucleus through changes in the lamin turnover rate, resulting in rounder nuclei. In correlation, hypergravity exposure might cause an increased cytoskeletal tension in astrocytes and subsequently change their nuclear shape through altered lamin dynamics. On the other hand, the observed changes in astrocyte nucleus morphology might have also been caused by changes in gene expression inside the nucleus, mediated by changes in chromatin distribution (Biedzinski, Agsu et al. 2020). Elongated nuclei are connected to higher migration rates in mesenchymal tumor cells (Grosser, Lippoldt et al. 2021).

Since the nuclei of astrocytes under hypergravity were less elongated, migration behavior might be compromised (see 3.5). Another factor at play could be the amount of DNA itself, since the DNA polymerase was also seen to be stimulated by 4*g* hypergravity (Takemura and Yoshida 2001).

Astrocytes in a standard cell culture are to some degree multinucleated, due to incomplete cell divisions along with the formation of syncytia from several cells. An increase in this phenotype is also connected to abnormal mitosis in reactive astrocytes (Sosunov, Wu et al. 2020). Cells that were exposed to 2*g* hypergravity for up to two days were multinucleated to a similar extend as the control cells (see Figure 20G), confirming that cell mitosis was not influenced by hypergravity. Hypergravity exposure had no effect on astrocyte nucleus morphology and number, which further indicates that 2*g* hypergravity has no adverse effects on astrocytes and does not cause an increase of reactivity *in vitro*.

3.5 Hypergravity dynamically reduces astrocyte migration speed

The migration of reactive astrocytes to the region of injury is a crucial part of astrogliosis induction, and if influenced will alter the dynamics of astrogliosis induction and further glial scar formation (Okada, Nakamura et al. 2006, Okada, Hara et al. 2018). It was shown that 2*g* hypergravity exposure impacts cell spreading and morphology in the short and long term (see 3.1). Since the functioning of these processes depends on the interaction of various cytoskeletal elements of the actin cytoskeleton and its associated motorproteins and cofactors, an effect of hypergravity on cellular migration could be expected. Amoeboid movement of astrocytes relies on rapid actin polymerization at the leading edge of the cell and retraction of the trailing edge mediated by actin stress fibers and myosin contraction. Previous research on cellular migration under hypergravity in other cell types had inconclusive results. HeLa cells exhibited decreased migration under 10*g* hypergravity (A. Tschopp 1983), whereas T-lymphocytes started migrating earlier than under normal gravity (Galimberti, Tolic-Norrelykke et al. 2006).

Astrocyte migration was measured by means of a wound healing assay (or scratch assay), using Ibidi cell culture inserts (see 4.3 and 4.4). For the first experiment, the wound healing assays were exposed to 2*g* hypergravity in the MuSIC for five days (see 2.4.1). Every day the samples were removed from the incubator centrifuge and imaged using phase contrast microscopy, before returning to centrifugation till the next day. Control samples were treated similarly but were not centrifuged. As a result, the percentage of the cell free area into which astrocytes had migrated, thus closing the “wound”, was already significantly lower after one day of hypergravity when compared to the 1*g* control samples. An approximately 32% reduction in cell migration under hypergravity was calculated for the first day of the experiment. After two days of centrifugation, approximately 28% reduction in closed area compared to the

control was measured and after three days still 26% reduction of astrocyte migration was seen. After four days, 15% of the scratches from the control group were completely closed but none of the hypergravity exposed samples. For every day of the experiment, there was a significant reduction in cell migration calculated via t-test. Both the 1*g* control and the 2*g* hypergravity samples exhibited a roughly linear migration speed over five days. These results point to a solid inhibition of astrocyte migration speed by hypergravity over time. This is confirmed by the results from 2.1.1.5 which showed no changes in astrocyte proliferation or apoptosis under hypergravity. One confounding factor of the MuSIC wound healing experiments was that for the daily imaging the centrifuge had to be stopped for one hour, which might cause a potential readaptation of the cells to normal gravity. This might also have led to an underreporting of the effects of hypergravity. Furthermore, as stated before (see 3.1), hypergravity exposure had stronger impairing effects on cell spreading in the first five hours of exposure compared to long-time exposure in the range of days (see 3.1). Since the first data point was only measured after 24 hours of centrifugation, potential early effects of hypergravity on migration speed could not be represented in these datasets.

Therefore, to investigate the cellular dynamics of early hypergravity exposure further, and to circumvent the problems of potential readaptation when the centrifuge was stopped, a new gravity research platform was introduced. Analogous to the MuSIC wound-healing experiments, 22-hour scratch assays were performed using live cell microscopy under 2*g* hypergravity on the Hyperscope (see 2.4.2). With the scratches being imaged every 30 minutes, astrocyte migration dynamics of the first day could be mapped with a 48-times higher resolution than before. The closed scratch area was significantly lower in the hypergravity sample than in the control, with a 35% reduction measured at the end of the experiment. Both the control and the 2*g* sample exhibited approximately hyperbolic migration curves during the first two and a half hours of the experiment with the hypergravity samples running slightly slower than the control. Calculating the regression lines for this time frame confirmed that the slopes for this time, which can be equated with the cellular migration speed, were not significantly different, indicating a lag phase in which the hypergravity sample did not yet react with a reduction in migration speed to the new stimulus. The control cells had an average migration speed of 3.6 µm/h, whereas the 2*g* sample migrated with a speed of 3.1 µm/h in the first two and a half hours. After this time the decreasing effect of hypergravity on the migration speed became more apparent and the curves clearly diverged. Regression analysis of the time frame from 2.5 to 22 hours resulted in a migration speed of 1.3 µm/h of the 1*g* control and a significantly lower speed of 0.8 µm/h of the 2*g* sample. Continuous centrifugation and live-cell imaging in hypergravity demonstrated a stronger inhibiting effect on astrocyte migration than observed in the preceding MuSIC experiment where the centrifuge had to be stopped for one hour daily and imaging was done under 1*g*. The fast, hyperbolic migration speed at the start

of the scratch assays could have been caused by different phenomena. On the one hand it is possible that the confluent astrocytes inside the cell culture inserts were accumulating at the edges of the wells before removal of the inserts and start of the experiment. After removal of the scaffold, the built-up cells then moved into the scratch area. This then would have not been a directed cellular migration but just a redistribution of cell mass. On the other hand, astrocytes might react in a time-delayed manner to hypergravity because the intracellular mechanisms responsible for cellular migration adapted to the increased mechanical loading following a temporal delay, causing the observed lag phase. Since the hyperbolic trend was seen also under normal gravity, the phenomenon was probably caused mainly by cellular accumulation and the following removal of cell contact inhibition.

A follow-up experiment was designed to elucidate the adaptation to 2*g* hypergravity and readaptation to 1*g* normal gravity after hypergravity exposure of astrocytes with regard to migration speed (see 2.4.3). Analogous to the preceding Hyperscope scratch assay, scratches with confluent astrocytes were prepared. The imaging was started with 12 hours of 1*g*, followed by 12 hours of 2*g* hypergravity exposure and finally again 12 hours of imaging in normal gravity. Using this approach, the confounding factors introduced with the removal of the scratch insert at the start of the experiment could be avoided and separated from the hypergravity adaptation phase. As a result, in the first 12 hours the migration speed was with 1.25 µm/h similar to the control values in the previous experiment running 22 hours, again cross validating this value as a baseline migration speed for astrocytes. The following 12 hours of 2*g* hypergravity led to a clearly visible reduction of migration speed to 0.42 µm/h, which was even lower than the speed that was measured under hypergravity exposure in the 22-hour experiment. This discrepancy might stem from not using the entire dataset for the previous experiment to calculate the linear regression curve from which the speed was derived. At the end of the 12 hours of hypergravity exposure the astrocytes' migration speed increased again to 1.27 µm/h, which was nearly identical to the 1*g* speed at the start of the experiment. This observation confirms that astrocytes can readapt to normal gravity after hypergravity exposure without any long-term impacts on their ability to migrate. The linear regression lines calculated for each 12-hour time frame did not perfectly align with the subsequent line corresponding to the change from 1*g* to 2*g* and also following the switch from 2*g* to 1*g*. Upon closer inspection of these time frames, lag phases became obvious in which the migration speed did not yet reduce although the cells were already exposed to increased mechanical loading under hypergravity or to reduced loading when changing back to normal gravity. At the point of adaptation from normal to hypergravity, an approximately one-hour lag phase was apparent, where the migration speed was still near the 1*g* value even though the centrifuge was already spun up to 2*g*. The reduction in migration speed during hypergravity did similarly lag behind when the centrifuge

was stopped, and the cells again exposed to normal gravity. In this case, a lag phase of two hours was observed.

It can be concluded that 2*g* hypergravity exposure led to a significant reduction of astrocyte migration speed in 22 and 12 hours of hypergravity exposure and to a slightly lower but still significant reduction of migration speed over five days. The observed decrease was mostly linear and appeared to have a lag phase of one to two and a half hours in which the intracellular mechanisms adapted to hypergravity. Likewise, the readaptation from hypergravity to normal gravity exhibited a longer lag phase of two hours. The astrocytes completely recovered from 12 hours of hypergravity exposure with regards to their migration speed. The shorter migration speed lag phase when adapting to hypergravity compared to the longer lag phase of normal gravity readaptation allow for speculation of the involved cellular mechanisms. Since migration and spreading are strongly depending on the actin cytoskeleton, integrins and motorproteins as well as the restructuring of the plasma membrane, the longer readaptation phase to normal gravity could be explained by the need of the cell to synthesize the required proteins. The rearrangement of the plasma membrane and creation of a leading lamellipodium with help of the actin cortex and the formation of stress fibers also require time. The shorter lag phase observed until migration speed reduction under hypergravity exposure commenced, could equally be explained because in this case no new cytoskeletal structures had to be synthesized by the cells. In this context, a follow-up experiment with an even longer hypergravity phase could be devised, to allow the cells more time for the disassembly of unnecessary cytoskeletal components and the degradation of surplus migration related proteins. If this model held true, then the longer hypergravity exposure would lead to an even longer lag phase of the migration speed when readapting to normal gravity.

Conclusively, a reduction of astrocyte migration through hypergravity will, if targeted at specific time points, reduce the number of astrocytes entering a reactive state, will therefore inhibit astrogliosis induction and will this potentially limit the severity of persistent glial scar tissue which would inhibit neuronal regeneration, but still allow for the immediate inflammatory response of reactive astrocytes to acute injury or illness. The results of lag phases in the astrocyte migration response are interesting with future applications for the therapy of astrogliosis and further glial scarring in mind, as effective windows for therapy need to be found to not unnecessarily stress patients.

3.6 Alterations of the actin and tubulin cytoskeleton caused by hypergravity exposure

Cytoskeletal rearrangements caused by hypergravity have previously been reported in various cell types. In one study, actin reorganization was observed in HUVECs after centrifugation at 3*g* for 24-48h (Maier, Cialdai et al. 2015), whereas in another study no changes of the

cytoskeleton of this cell type were seen after 16 hours of 3*g* and 10*g* exposure (Costa-Almeida, Carvalho et al. 2016). In MDA-MB-13 breast cancer cells, 3x 20 min of 10*g* centrifugation led to visible degradation of the actin cytoskeleton (Lee, Kim et al. 2021). Thus, there might be cell-type specific cytoskeletal reactions to hypergravity which can be significant but also subtle, and thus must be imaged with high-resolution microscopy to detect also small changes. Indeed, no obvious changes of the cytoskeleton were spotted in preliminary experiments using epifluorescence microscopy which has an on average 10 times worse resolution compared to super resolution STED microscopy. Since the measured decrease in astrocyte area and spreading (see 3.1), as well as the strong decrease of migration speed (see 3.5) through hypergravity exposure suggest an involvement of the astrocyte cytoskeleton, super-resolution STED microscopy and fluorescent live-cell microscopy were employed to more closely examine the two main cytoskeletal elements of astrocytes, actin and tubulin filaments, which were exposed to hypergravity and compared to 1*g* control cells.

The first experiment was performed with astrocytes grown on cover slips and exposed to 2*g* and 10*g* for one day in the MuSIC, including a 1*g* control group. These cells were stained with Phalloidin for F-actin and tubulin and imaged using a super-resolution STED microscope (see 2.5). By using the STED capabilities, the intracellular microtubule network could be resolved in finest detail with clearly visible microtubules. The F-actin staining revealed actin structures such as stress fibers, the actin cortex as well as lamellipodia and filopodia. Resulting from the complexity of the data, only a qualitative analysis of several cells could be performed.

Comparing the actin cytoskeleton of the 1*g* control cells to the 2*g* and 10*g* samples, certain features were visible across all samples. Filopodia could be seen in the control as well as in the hypergravity samples, as well as a clearly pronounced actin cortex and stress fibers. However, the 1*g* cell was strongly polarized with a large lamellipodium, whereas the cells exposed to hypergravity were less polarized and protruded smaller lamellipodia in many directions and seemed less irregular in their general cell shape. Although this cannot yet be generalized without the availability of a quantitative analysis program, a loss of cell polarization and reduced actin-related protrusions could be responsible for the observed reduction in cell migration speed under hypergravity (see 3.5). The microtubule network in the 1*g* control was well pronounced, localized perinuclearly with fewer microtubules closer to the cell perimeter. At higher gravitational loads, the perinuclear polarization was reduced, and microtubule concentration seemed to increase. The 10*g*-exposed astrocyte had a clearly reversed microtubule network polarization with fewer tubules located perinuclearly and more tubulin close to the cell membrane. When inspecting the actin and tubulin components of cellular protrusions, it became apparent that the hypergravity-exposed cells showed an unusual phenotype. Single microtubules and microtubule bundles reached into the tips of lamellipodial protrusions where normally only actin filaments, but no microtubules, are located. This

anomaly might be related to the increasing tubulin density at the cell perimeter and/or actin fiber instability, both exerted through the increase in mechanical loading. Areas with high cytoskeletal dynamic and increased turnover of both cytoskeletal components were affected by hypergravity exposure, while more static structures such as stress fibers did not change under hypergravity. These results point to alterations in the dynamic turnover of actin and tubulin through hypergravity exposure, with a minor effect on previously existing cytoskeletal structures. Structural changes of the cytoskeleton are extremely difficult to objectively quantify, and this investigation should be taken as a first start of STED-based cytoskeleton analysis of astrocytes which needs more data acquired and more intricate analysis algorithms to present a definite conclusion regarding cytoskeletal changes under hypergravity.

To further examine dynamic changes of the actin cytoskeleton, the LifeAct-GFP mouse line was employed (see 2.6) (Riedl, Crevenna et al. 2008). Primary cortical astrocytes generated from these mice exhibit a stable expression of the LifeAct peptide which binds to F-actin without disturbing actin polymerization and is tagged with a GFP fluorophore. After optimization of the imaging protocols to minimize phototoxicity and bleaching of the cells caused by epifluorescence microscopy (see 4.6.4), the actin cytoskeleton of astrocytes was fluorescently imaged on the Hyperscope using a time lapse of first normal and subsequently 2*g* hypergravity. Hereby, regions of interest in the same cells could be compared under both conditions (see Figure 26).

The most obvious reaction of astrocytes when the mechanical loading exerted on them was increased from 1*g* to 2*g* was observed at the cell perimeter. Lamellipodial retraction started less than an hour after the onset of hypergravity, leaving behind many actin-rich retraction fibers. The previously described smaller cell area of astrocytes exposed to hypergravity (see 3.1) and reduction of migration speed (see 3.5) could, among defects in cell spreading, also be caused by this retraction of cellular protrusions. Membrane ruffling, also playing a role in cellular migration, was observed less frequently in hypergravity. Inferring from actin-spots in the actin cortex near the cell perimeter, focal adhesions were present in both gravity conditions, although their general location seemed to shift more into the direction of the cell center. The creation of focal adhesions near the leading edge of the cell is equally important for cell migration, and if this process was impaired it would have a negative effect on cell motility. Actin stress fibers spanning the cell were clearly stained and identified in the LifeAct-GFP expressing astrocytes. As already established in STED microscopy, also in the experiments using the transgenic fluorescently labeled cells there were no obvious changes in stress fiber number, thickness or parallelity after two hours of hypergravity exposure when compared to their state in normal gravity. Concurring with the previously identified reduction of cell polarization, smaller cellular protrusions were seen to be retracted under hypergravity. Utilizing fluorescent live-cell microscopy, results of super-resolution microscopy could be cross-verified and more

assumptions about the underlying mechanisms responsible for the reduction of cellular migration as well as spreading defects could be made.

In general, existing F-actin structures of the cytoskeleton seem to be remarkably resistant to increased mechanical loading from 2*g* to 10*g*, while the dynamic processes of actin treadmilling and branching and microtubule elongation and disassembly are impacted to a greater extent by mechanical loading through hypergravity exposure. With the current state of cellular research under hypergravity, it is not yet known to which extend these results can be translated to other cell types, although it can be expected that the basic mechanisms of cytoskeletal dynamics would also be influenced in other mammalian cell types. Another factor coming into play here is, that astrocytes are remarkably adherent and thinly spread, which might give these cells an increased structural stability and resilience to mechanical loading as compared to more roundish and compact or even suspension cells such as cells of the immune system, which are known to be influenced by altered gravity exposure. A stabilization and thereby increase of microtubules and a destabilization of dynamic F-actin structures under hypergravity could explain the observed reduction in cell spreading (see 3.1) and slower cellular migration (see 3.5).

3.7 Western blotting of reactivity and migration proteins confirms microscopic observations

To verify the observations by live-cell and fluorescence microscopy that astrocyte reactivity is partially reduced by hypergravity, as well as the observed reduction of cell spreading and migration speed, key proteins of related processes were analyzed using Western blotting.

Astrocytes were cultured under 2*g* hypergravity in the MuSIC incubator centrifuge for up to three days and compared to time-matched 1*g* control samples. Western blots were used to compare the relative protein levels between the hypergravity samples and the controls at each day (see 2.7).

Astrocyte reactivity levels under hypergravity were previously measured using microscopy by quantification of fluorescence intensity of reactivity-associated intermediate filament proteins GFAP, vimentin and nestin, as well as LZK (see 2.2). The general observation regarding the levels of these markers was that reactivity is not elevated under hypergravity and according to certain markers astrocyte reactivity might even be reduced by 2*g* exposure (see 3.3). Consequently, the expression levels of vimentin and GFAP under hypergravity were compared to the 1*g* controls by Western blotting. After one day of hypergravity exposure, GFAP and vimentin levels show no significant changes compared to the control. Vimentin levels increased slightly after two and three days of hypergravity exposure compared to the control, and GFAP levels increased slightly after two days and were reduced after three days. These results confirm that intermediate filament expression in astrocytes is to some extend modulated by

hypergravity exposure but that it does not significantly increase the expression of these reactivity markers. In the fluorescence intensity measurements, GFAP intensity peaked after two days, similar to the Western blot results although the intensity in the control samples was always higher than in the hypergravity sample. Vimentin fluorescence intensity similarly peaked after two days of hypergravity exposure and was always lower than the control fluorescence intensity. It is open to speculation why the western blot samples exhibited higher intermediate filament expression in the hypergravity-exposed cells at some time points whereas the fluorescence intensity measurements reported otherwise.

The small GTPases of the Rho family control cytoskeletal dynamics and cell adhesion and are in part responsible for cell migration (see 1.3.5) (Blanchoin, Boujemaa-Paterski et al. 2014, Hodge and Ridley 2016). RhoA expression was increased after the first day of hypergravity exposure but remained unchanged afterwards, and RhoG expression was slightly increased after one and two days in hypergravity and slightly decreased after the third day. A dysregulation of the Rho GTPase system as observed here might play a role in the decreased migration speed and alterations in cytoskeletal structures of astrocytes under hypergravity. Since Rho GTPases are also partaking in actin reorganization, the actin related phenotypes seen in LifeAct-GFP live-cell imaging such as lamellipodial retraction and less membrane ruffles could in part be caused by Rho GTPase dysregulation. Indeed, Rho activation and actin reorganization was previously reported in endothelial cells after centrifugation at 3*g* (Koyama, Kimura et al. 2009). The process might also work in reverse where changes in actin treadmilling dynamics are directly caused by hypergravity and the changes in Rho expression are resulting from these changes.

Lastly, the expression of FAK, a protein associated with focal adhesions and cell spreading was measured. Slight but non-significant changes in FAK protein expression were measured. A strong reduction in FAK expression is known to decrease cellular motility (Yu, Gao et al.

2018). These results are in line with the observation made using LifeAct-GFP imaging that focal adhesion number is not significantly modulated by 2*g* hypergravity exposure.

In summary, due to the observed results, the following model is proposed (see Figure 35).

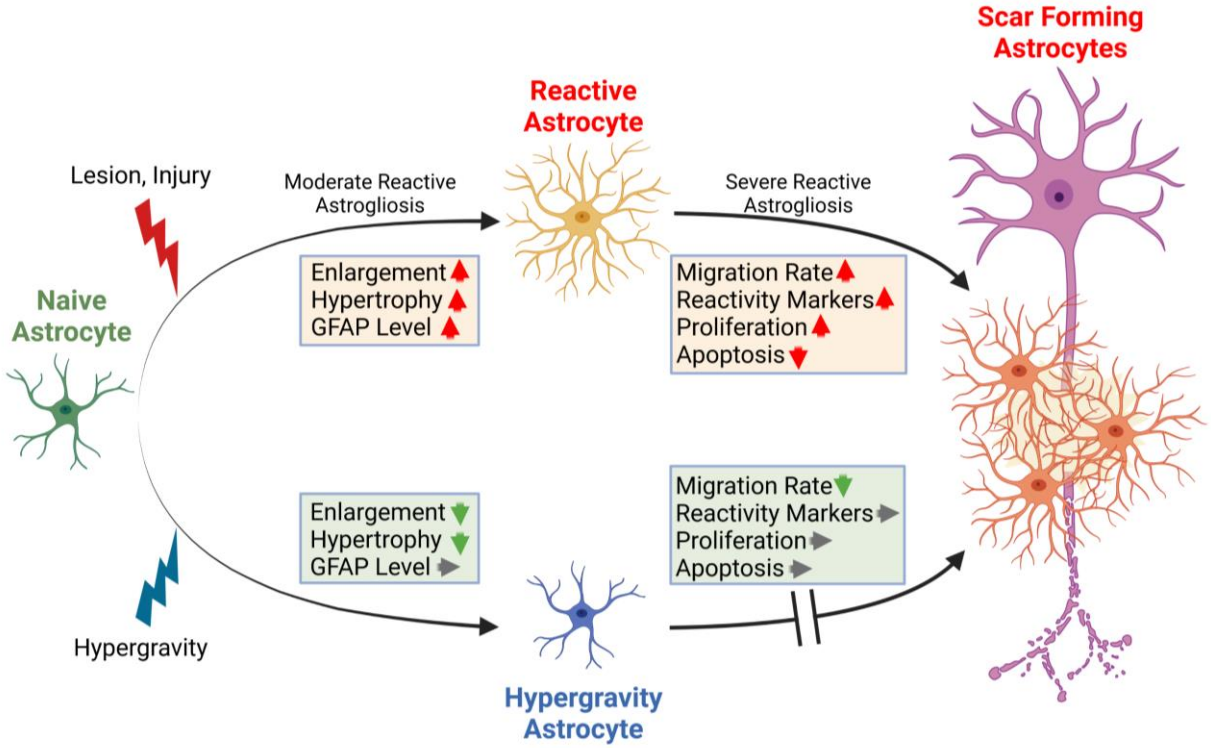

Figure 35: Effects of 2*g* hypergravity exposure on astrocyte reactivity and astrogliosis *in vivo*. Under normal gravity, astrocytes become reactive after injury, changing their molecular mark-up and behavior. Hypergravity exposure, that means increased mechanical loading, was shown to prevent or dampen characteristic reactivity phenotypes in astrocytes (created with Biorender).

Hypergravity exposure in the range of 2*g* attenuates changes in astrocytes which are connected to moderate reactive astrogliosis *in vivo*. These hypergravity-exposed astrocytes are smaller and less hypertrophic than controls in normal gravity. Consequentially fewer scar-forming astrocytes are developing and severe reactive astrogliosis could be inhibited.

3.8 Simulated microgravity exposure affects astrocyte morphology partially comparable to hypergravity

After discovering that hypergravity, which is essentially increased mechanical loading, affected astrocytes in their morphology (3.1), behavior (3.5) and reduced key parameters of astrocyte reactivity such as GFAP expression (3.7), the effects of simulated microgravity (s-µ*g*) achieved through mechanical unloading were investigated. When comparing the effects of different gravity levels on biological systems, it is always reasonable to check both hyper- and microgravity exposure and find out if there is a linear, hyperbolic, or other relation between gravity level and biological effect strength since from (simulated) 0*g* to 1*g* to 2*g* the cells are

theoretically subjected to a linear increase in mechanical loading. This sometimes., but not always translates to a linear increase in effect strength of observed phenotypes (van Loon 2016). Research into the effects of microgravity exposure on neuronal cells of course also has an intrinsic relevance for human space flight, as astronauts are subjected to this environment for months at a time and especially the brain and CNS of astronauts cannot be examined by invasive means such as biopsies. Astrocytes subjected to simulated but also real microgravity can thus serve as an analogue for brain health and injury response in astronauts.

Mechanical unloading through the use of a 2D slide flask clinostat was employed to simulate microgravity conditions for primary murine astrocytes. Several analyses that were performed under hypergravity were repeated under mechanical unloading by clinorotation. In this way it should be investigated if similar or contrary effects to the hypergravity-induced astrocyte phenotypes were revealed, which would further point to their underlying pathways. Firstly, astrocytes were exposed to s-µ*g* for three hours to two days, fixed at various time points and stained for F-actin and GFAP. The staining in both the 1*g* as well as the s-µ*g* samples was similar with regards to fluorescence intensity, the number of cells stained, and their general appearance, signifying a high-quality primary astrocyte culture (see Figure 28).

Analogous to the analyses performed in 2.1, several morphological parameters were measured and evaluated by semiautomatic cell recognition in Zeiss Zen. The cell area of single astrocytes exposed to simulated microgravity was measured and compared to 1*g* controls (see 2.8.1). After three hours, shortly after the start of clinorotation, astrocytes exposed to s-µ*g* were significantly larger by 15% than the control. This difference disappeared at the later time points of six hours, 12 hours and after one day, where no significant difference in cell size was measured. Only after two days of simulated microgravity exposure a significant reduction of cell spreading was measured in the s-µ*g* sample with a reduction of 18% in cell size compared to the 1*g* control.

Interestingly, simulated microgravity exposure seemed to have a delayed effect on cell spreading when compared to 2*g* hypergravity exposure, where spreading defects were seen already in the initial spreading and also after one and two days of exposure (see 3.1). The severity of the observed spreading reduction under simulated microgravity was similar to the effect of 2*g*, with the onset delayed by one day. This suggests a longer latency period for the astrocytes until clinorotation affects spreading, or that mechanical unloading has a weaker effect than increased mechanical loading. The significant increase in spreading or cell size at the first time point could imply an additional stress response towards mechanical unloading by clinorotation which the cells had already adapted to after six hours.

When further analyzing the cells' morphology, there were no significant changes in the minimum or maximum Feret values or the Feret ratios. Only after two days of simulated microgravity, there was a significantly larger Feret maximum measured in the 1*g* control (see

2.8.2). This again translates directly to the increased cell size at this time point. In both the clinorotated, as well as the control sample, the Feret ratio decreased from one to two days of exposure. This can be attributed to a further spreading and establishment of a two-dimensional adherent cell layer of the astrocytes, as cells that are adhering to a substrate after seeding tend to be very round, thus have a higher Feret ratio, and in the course of their growth, through spreading and cell division they become more diverse in their cell shapes, leading to a lower Feret ratio.

Whereas after three hours of clinorotation, astrocytes were significantly more circular than the control cells, this ratio inversed after six and 12 hours, where the control cells were more circular than the cells in s-µ*g* (see 2.8.3). Over the course of these 12 hours, the circularity in the control sample steadily increased, whereas the clinorotated sample showed a steady decrease in circularity. Although the measured differences in circularity were quite small, they could hint at a stress or adaptation response of the cells to simulated microgravity.

In conclusion, morphological alterations in simulated microgravity show no clear trend over time, but the cells rapidly respond and counterbalance the alterations over intermediate to long durations. In the future it will be interesting to see if the observed effects of simulated microgravity on cell spreading also translate to changes in behavior, e.g., cell migration as it was the case with hypergravity exposure.

3.9 Astrocyte reactivity, proliferation, and microtubule network unchanged by clinorotation

Hypergravity exposure reduced the number of reactive astrocytes. i.e. expressing high levels of the reactivity marker protein GFAP (see 3.3). To investigate the effect of mechanical unloading on astrocyte reactivity, primary murine astrocytes were exposed to simulated microgravity and percentages of GFAP-high expressing cells were compared to 1*g* controls. Clinorotation did not significantly change the ratio of GFAP-high expressing astrocytes compared to the 1*g* control at any time point between three hours and two days (see 2.8.5). Thus, clinorotation, in contrast to hypergravity exposure, did not reduce astrocyte reactivity. There could be different underlying reasons for this. Firstly, mechanical unloading, or simulated microgravity, might affect the cells differently than increased mechanical loading through hypergravity exposure. This was also evident in the slower effect and partially different phenotypes regarding cell spreading under s-µ*g* (see 3.8) as compared to 2*g* (see 3.1).

Also, under simulated microgravity, the viability of the cultured cells was controlled for by apoptosis and proliferation assays. Similar to the hypergravity experiments (see 3.2) it had to be verified that mechanical unloading produces no unwanted proliferation or increased cell death in the primary murine astrocytes as this would produce artifacts in the measurements and mask eventual effects of altered gravity exposure. Astrocytes in the healthy brain are

proliferating very slowly and exhibit low apoptosis rates, which leads to a stable tissue homeostasis. An increase of proliferation under simulated microgravity would in astrocytes mean increased reactivity and could the worst-case lead to cancerous cell growth, and an increase of apoptosis would result in tissue death.

A Ki67 fluorescence staining was used to measure the number of proliferating astrocytes when exposed to clinorotation and compared to the static 1*g* control (see 2.8.4). For clinorotation, the fraction of Ki67 positive cells was 0.7% but non-significantly lower than in the control group and after two days there was a non-significant reduction of 0.82% compared to the control. The measured reduction in cell area and spreading following clinorotation, thus, did not coincide with increased reactivity or decreased viability. Nevertheless, it must be kept in mind that fast clinorotation is a simulation approach assuming that the exposed systems (here astrocytes) do not perceive the rotating g-vector, otherwise they would be permanently mechanically stimulated. Therefore, a final validation is needed in real microgravity to quantify the chosen simulation approach (Herranz, Anken et al. 2013).

Real microgravity was shown to lead to disruptions of the tubulin cytoskeleton in adherent breast cancer cells (Nassef, Kopp et al. 2019). After staining primary murine astrocytes for tubulin and imaging the cells using an epifluorescence microscope, no qualitative changes in their intracellular tubulin network could be observed. To quantify the composition of the tubulin cytoskeleton and identify changes caused by clinorotation, a categorization approach, as used by Wuest et al., was applied (Wuest, Arnold et al. 2020). The tubulin cytoskeleton as imaged by epifluorescence microscopy and the astrocytic intracellular microtubule network was grouped into three distinct categories with the first having a well-defined microtubule network, the second having a few well-defined fibers and the third category having only a diffuse cloud of microtubules (see 4.8.9).

The percentage of cells with a completely diffuse microtubule network did not increase after three to 12 hours of clinorotation. However, after three hours, more cells in the s-µ*g* group were assigned to the second category compared to the 1*g* control, hinting at a slight disruption of the tubulin cytoskeleton. After six hours of exposure this ratio was inverted, with more cells of the control being classified as second category microtubule networks than the clinorotated samples at the same time point. After 12 hours again, more cells with only few well-defined microtubules were observed in the s-µ*g* exposed astrocytes than in the control. Cells with no discernible microtubule network were only detected after six hours exposure with an evident difference of 8% cells in the control versus 12% cells in the simulated microgravity sample. These results are in contrast to previous studies using different cell types, where obvious changes or disruptions in the microtubule cytoskeleton of adherent cells were reported after exposure to up to 48h of real microgravity (Marian Lewis 1998, Vassy and Irinopoulou 2001). Here, it has to be kept in mind, that simulations need a verification in real microgravity to

exclude non-gravitational effects induced by the simulation approach. Furthermore, also experiments in real microgravity on e.g., sounding rockets, parabolic flights, and on orbit on the ISS or capsules pose additional problems and stress factors (e.g., accelerations and vibrations during launch, ionizing radiation, temperature fluctuations, and operational limitations) which might influence cellular integrity and specifically the cytoskeleton. Thus, control experiments and comparison with data from ground-based simulations are necessary. Neuronal cells and especially astrocytes were very rarely investigated under simulated microgravity before. The astrocytes' phenotype is thinly spread and less prone to migration, in contrast to previously investigated cell types. Spreading and strong adherence to the substrate could in consequence lead to a more stable filament network in astrocytes which might be less sensitive to disruptions as it is more rigidly anchored to the growth substrate (via focal adhesions) than in other, smaller and more motile cells. Further studies using live-cell imaging of the different cytoskeletal elements in simulated and real microgravity are necessary to disentangle the effects of gravity and other environmental factors.

3.10 Altered gravity exposure reduced astrogliosis-related features *in vitro*

Astrocytes *in vivo* become reactive as a result of CNS tissue damage, neuronal diseases or inflammation. Reactive astrocytes exhibit phenotypes such as hypertrophy and increased GFAP expression levels (see 1.2.2, Sofroniew and Vinters 2010). Upon becoming reactive, astrocytes migrate to the region of the injury and proliferate there to form the glial scar. This process of increasing reactive astrogliosis is accompanied by the expression of various reactivity markers as well as enhanced cellular maintenance by reduction of apoptosis and induction of hyperproliferation (see Figure 35). By exposing primary murine astrocytes to 2*g* hypergravity *in vitro*, several aspects related to a reactive phenotype could be prevented or diminished.

Cell spreading and migration in a 2D primary astrocyte culture employ similar mechanisms and pathways as astrocytes *in vivo* when they become reactive. Astrocyte morphology changes with regards to hypertrophy of the cell body and astrocyte processes, which ultimately leads to overlapping of single astrocyte domains and formation of the glial scar tissue (see 1.2.4., Escartin, Galea et al. 2021). Through hypergravity exposure, initial cell spreading could be reduced by 45% and long-term spreading and cell size was reduced by 20% (see 3.1). Cell migration itself is a hallmark in astrogliosis as it is required for the infiltration of reactive astrocytes into the injured tissue and the following glial scar formation. The underlying mechanisms of cell migration such as cytoskeletal rearrangement and their corresponding motorproteins are also employed in cell spreading (Janmey, Hinz et al. 2021), and indeed, hypergravity exposure also strongly and reversibly diminished astrocyte migration speed *in*

vitro (see 3.5). Reactive and scar-forming astrocytes rely on an increased proliferation rate as well as reduced apoptosis, to increase their viability in case of an injury (see 1.2.2., (Zhan, Gao et al. 2017). Hypergravity exposure did not alter astrocyte viability parameters over several days of exposure (see 2.1.1.5). Super-resolution STED, as well as live cell fluorescence microscopy of F-actin structures and the microtubule network (see 3.6) revealed changes of cytoskeletal architecture due to increased mechanical loading. Cells cultivated in hypergravity appeared to have less polarized actin filament networks, with lamellipodia protruding in various directions. Live-cell imaging revealed that dynamic actin structures such as filopodia and lamellipodia were impacted by hypergravity exposure and pre-existing, stable actin filaments such as stress fibers or the actin cortex were not influenced. The microtubule network of astrocytes was polarized more into the direction of the cell perimeter under hypergravity. These observations hint to a destabilization of dynamic F-actin structures and a stabilization of microtubules through hypergravity, which could be one cause for the hitherto observed reductions in cell spreading and migration.

Another early reaction of astrocytes to CNS injury and the first step in becoming reactive is the upregulation of the intermediate filament GFAP. Astrocytes exposed to hypergravity expressed less GFAP compared to controls, indicating a lower reactivity state (see 3.3). Other reactivity related markers such as vimentin, nestin and LZK did also not increase in hypergravity and were partially reduced. The exact pathways which lead to the observed hypergravity phenotypes are still elusive, even though cytoskeletal structural proteins were regulated as shown before (see 3.6). Since reactive astrocytes increase the number and size of fine astrocyte processes which are reliant on coordinated actions of these cytoskeletal elements, one could expect a less finely branched astrocyte phenotype *in vivo* after hypergravity exposure. As a conclusion, hypergravity-exposed astrocytes exhibit a less-reactive phenotype *in vitro*.

Mechanical unloading under simulated microgravity evoked similar, but less pronounced phenotypes as hypergravity exposure in astrocytes. Primary murine astrocytes were exposed to simulated microgravity by clinorotation, leading to alterations in cell size and morphology. Analogous to the effects of 2*g* hypergravity exposure on astrocytes, spreading defects were measured although they were less severe and noticeable and occurred only after longer exposure in simulated microgravity (see 3.8). Astrocyte reactivity was not increased in simulated microgravity, as indicated by GFAP immunostaining (see 3.9), which was similar to the results after hypergravity exposure. The microtubule network showed only small and transient impacts of clinorotation (see 3.9). These observations suggest that mechanical unloading under simulated microgravity by clinorotation affects cells in a comparable, but less severe or slower-acting manner compared to increased mechanical loading through

hypergravity. Astrocyte reactivity might only be affected after longer times of (simulated) microgravity exposure.

In patients suffering from CNS injuries or neurodegenerative diseases, the glial scar remains in focus of therapeutic interventions. The possibility to attenuate glial scar formation in a time-sensitive process, to retain the immediate inflammatory response of reactive astrocytes but decrease the formation of persistent astrogliosis and further glial scar tissue would offer new approaches for the induction of neuronal regeneration. The results of this thesis have shown that in primary murine astrocytes features of reactivity and prerequisites of glial scar formation can be reduced on several levels *in vitro* by hypergravity exposure in a dynamic and reversible way while having no harmful side effects for the cells (see Figure 35). By targeting the key pathways and molecules responsible for those hypergravity-related changes in astrocyte reactivity in a controlled fashion using small molecules or novel pharmacological interventions, possibly pairing them with non-invasive hypergravity exposure to exploit synergistic effects, reactive astrogliosis could be reduced *in vitro* as well as *in vivo*. Reducing reactive astrogliosis will have in turn a long-term effect in promoting neuronal regeneration due to attenuated inhibitory environments that would otherwise be elicited by reactive astrocytes *in vivo*. The road towards novel patient treatments will be the subject of future studies based on this work to attenuate but not completely prevent astrocyte reactivity and thus counteract the observed excessive inhibition of neuronal regeneration.

3.11 Outlook

In the current study, astrocytes reacted to 2*g* hypergravity, as well as to simulated microgravity by clinorotation with similar defects in spreading, leading to reduced cell size. This reaction to the changes in their gravitational environment indicates their ability to “sense” gravity in a so far unknown manner. Indeed, astrocytes are known to be mechanosensitive and as an integral part of the blood-brain barrier can react to changes in blood pressure and brain perfusion. Candidate mechanosensitive proteins in astrocytes are the transient receptor cation channel TRPV4 and Connexin43 (Turovsky, Braga et al. 2020) and the mechano-gated ion channel Piezo1 (Shaopeng Chi 2022). It would therefore be interesting to repeat the hypergravity- and simulated microgravity experiments with inhibitors against or knock-out cell lines of these mechanosensitive channels. This would further bring to light how mammalian cells, and astrocytes in particular, sense gravitational cues in their environment. Viewing astrocytic cellular responses to hypergravity, the observed spreading defects as well as the decreased migration should be examined with the same assays but under increased hypergravity of 3*g* and more to find out if there is a dose-response curve with regards to the severity of the changes of cell morphology and behavior under hypergravity. When exposing cells to increased hypergravity regimen, viability needs again to be controlled for. To find out if the

decrease in cell spreading and cell area is going hand in hand with a decrease in cell volume, or if the measured spreading reduction is due to the cells becoming more spherical, but keeping their volume constant, astrocytes should be analyzed by cytosolic, or membrane staining and imaged in a confocal microscope using z-stacking. By this, a 3D model of each cell can be generated to calculate the cell volume. These volumes can then be compared between normal and hypergravity to see if the cell volume is reduced by increased gravitational loading.

It is still not clear if the observed reduction in astrocyte migration under hypergravity is solely caused by changes in cytoskeletal dynamics or if other cellular pathways which influence migration behavior play a part in this phenotype. To this end, more thorough biochemical and genetic analyses should be performed, taking into account other proteins which are implicated in astrocyte migration such as MMP-2 and MMP-13 (Verslegers, Lemmens et al. 2013) and other Rho-associated proteins (Hodge and Ridley 2016). RhoA for example is implicated in actin stress fiber and focal adhesion formation (Pellegrin and Mellor 2007), and a more than 1.5 times increase in RhoA protein expression was detected after one day of hypergravity exposure (see 2.7). More thorough analyses using protein mass spectrometry or RNA sequencing of astrocytes exposed to altered gravity conditions can be performed to yield more in-depth results of the cells' transcriptome and protein content. Indeed, using the experiment payload Cellfix on the sounding rocket MAPHEUS 13, primary murine astrocytes were exposed to six minutes of real microgravity and fixed to be retrieved for transcriptomic analysis. These samples will be compared to 1*g* ground controls and hypergravity-exposed cells with regards to the already identified proteins but also to find newly regulated targets.

Cellular migration should also be investigated not only in hypergravity, but also in (simulated) microgravity. Astrocyte reactivity is a complex and not yet thoroughly defined mechanism which could be defined by many more markers than investigated in this study. Studied by many researchers, novel markers are constantly found which will help to identify and further understand various reactivity phenotypes. Newly found targets can also be investigated in altered gravity exposed cells to learn more about astrocyte reactivity in hyper- and microgravity. A reactive phenotype in astrocytes could be chemically evoked by addition of e.g., pro-inflammatory cytokines such as IL-1β and TNF, or by the addition of medium from activated glia (Retamal, Froger et al. 2007, Lagos-Cabre, Alvarez et al. 2017).

Live-cell epifluorescence microscopy employing LifeAct-GFP astrocytes showed alterations of the actin cytoskeleton under hypergravity in a qualitative analysis. These experiments could also be repeated under increased hypergravity loading of 3*g* and more to see if the observed changes in actin dynamics increase in severity. In this regard, projects have been initiated to develop software solutions for artificial intelligence-supported recognition of cells and intracellular filaments such as actin, microtubules, and intermediate filaments. For accurate

machine learning algorithms, large training datasets with the features that shall be recognized (e.g., intracellular fibers) labeled must first be generated. This in itself of course is a high workload and has to be evaluated as a trade-off. Additionally, it is not yet clear how cell-type specific such a model will be. To have scientific merit, a potential automatic program for recognition of intracellular features needs to output discrete and objective data, where the "black box" paradigm of machine learning algorithms could prove problematic. With regards to these challenges, more classical approaches using mechanisms such as thresholding and watershed segmentation are also being evaluated. A functioning, and ideally universal program will ultimately help to not only qualitatively examine microscopy images, but also objectively quantify changes in cytoskeletal morphology after altered gravity exposure not only in epifluorescence but also in confocal and STED microscopy images. Live-cell microscopy on the Hyperscope is logically confined to hypergravity exposure, but a prototype clinostat microscope is being developed at the DLR which will enable live-cell microscopy also in simulated microgravity. Live-cell microscopy can be enhanced with further channels or fluorophores by employing live-staining solutions for other cytoskeletal elements, such as SiR-tubulin, Pkmito, or by using other transgenic mouse models to visualize GFAP or other intermediate filaments.

Live-cell microscopy in real microgravity will in the future be possible on the ISS by means of the FLUMIAS instrument which is being developed by the DLR. LifeAct-GFP astrocytes are part of a planned project (Live Assessment of Astrocytic Reactivity Adaptations under Space Conditions – LAARA) and shall be imaged in microgravity and increments up to 1*g* with added tubulin and calcium live stains to elucidate astrocyte adaptation to real microgravity and eventual changes in morphology, behavior, and reactivity. By imaging the cells while they are exposed to different centrifugation speeds between 0*g* and 1*g*, the thresholds of reaction to gravity will also be investigated and can be directly compared to the hypergravity and simulated microgravity data in this thesis.

Ground-based studies using simulated microgravity and mechanical unloading with clinostats started in this work (see 2.8) are planned to be continued in more detail. A clinostat that can hold Ibidi 3.5 cm dishes (see 4.2.3.4, 4.2.3.5) is in construction, so that migration assays in simulated microgravity can be performed to compare the astrocyte migration speed under various gravity conditions.

The employed methods of hypergravity exposure in the MuSIC for fluorescence and STED microscopy and live-cell microscopy under hypergravity of scratch assays and cell spreading or intracellular actin dynamics have been newly developed for this project and can be translated to many other cell types or model systems to enrich the field of research under altered gravity conditions.

Altogether, the findings of this work pave the way for new insights into cellular reactions to hypergravity and open up new avenues of research for the treatment of astrogliosis and resulting impairments of the CNS. The underlying pathways responsible for the observed hypergravity phenotypes could, when characterized in detail, be exploited to alter astrocyte reactivity *in vivo* and thus lead to new treatments for neurological disease or injury. For these aims, other model systems such as 3D cell culture, brain organoids, *ex vivo* techniques such as acute brain slices and *in vivo* mouse models need to be employed to move closer to the level of the whole organism.

The timed attenuation but not complete ablation of astrocyte reactivity through hypergravity exposure may possibly be established as a non-invasive means of reducing the negative effects of astrogliosis and enhance neuronal regeneration. This approach can be combined with classical drug-based therapies to selectively diminish the adverse effects of glial scarring *in vivo* but retain the positive properties of reactive astrocytes and astrogliosis.

4. Methods

4.1 Devices for altered gravity exposure

At the DLR Institute for Aerospace Medicine, specialized devices are built to expose biological samples to altered gravity conditions. With regards to hypergravity, centrifuges are used on which cells and other biological material can be subjected to increased gravitational loading under otherwise unchanged culture conditions. Simulated microgravity experiments are performed on clinostats. The machines which have been used in this work were all designed and built in-house and are described in the following chapters. The MuSIC and Hyperscope were developed and established in the course of this thesis.

4.1.1 The multi-sample incubator centrifuge (MuSIC)

The Multi-sample incubator centrifuge consists of a Binder C170 cell culture incubator with a built-in centrifuge (see Figure 36). With this device, biological samples can be exposed to constant and long-term hypergravity under controlled conditions.

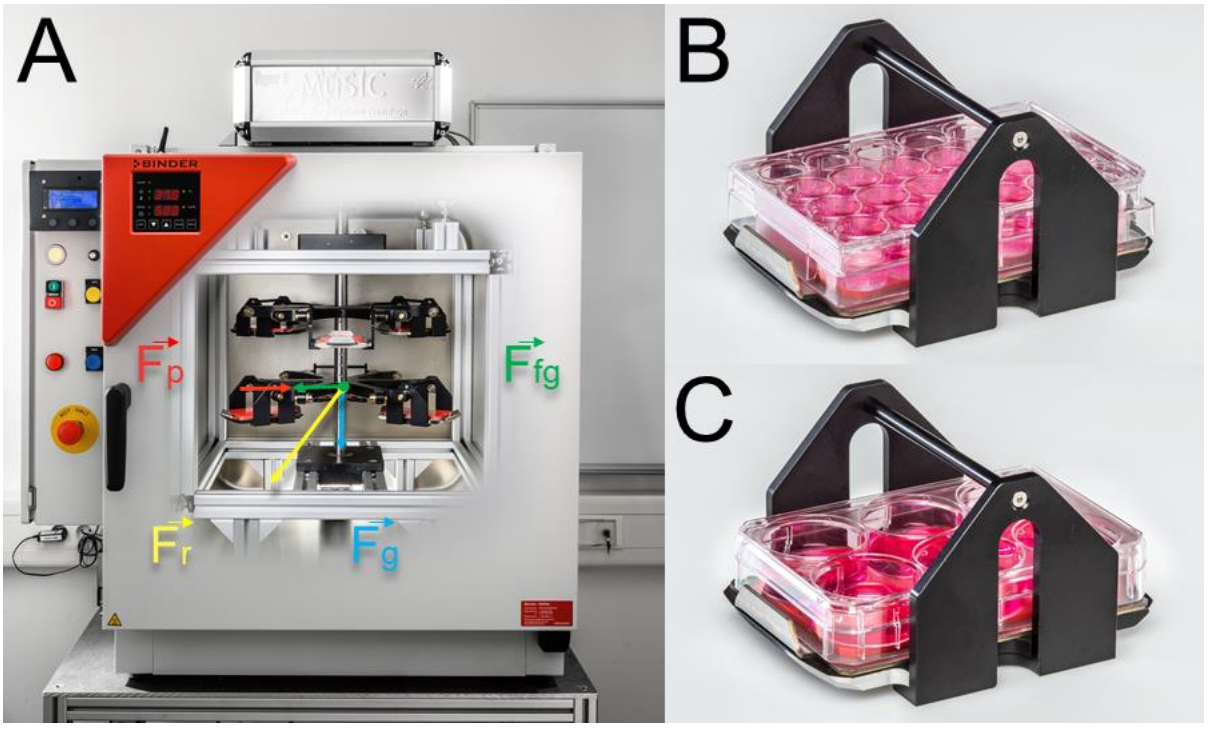

Figure 36: The Multi Sample Incubator Centrifuge (MuSIC). (A) Front view of the centrifuge device inside the incubator, with the exerted and resulting forces marked with arrows. F_p: Centripetal force, F_{fg}: centrifugal force, F_r: resultant force, F_g: gravitational force. **(B)** One centrifuge gondola with a 24-well plate installed. **(C)** One gondola with a 6-well plate installed.

The centrifuge arms accept swing-out gondolas which can be adapted to various cell culture vessels. Since the centrifuge unit is contained in an incubator, biological samples can be exposed to finely tunable hypergravity conditions in an otherwise unchanged cell culture environment with regards to temperature, CO_2, and humidity. The swing-out gondolas ensure

that the gravity vector resulting from centripetal/centrifugal force and Earth gravity always acts perpendicularly onto the sample. This is to prevent unwanted shear forces or movements of the sample. The centrifuge rotor is connected to the direct drive motor via magnet coupling, preventing any vibrations that would otherwise function as an environmental stimulus and disturb the experiment. The centrifuge unit is controlled by a microprocessor which and can be fine-tuned for duration, ramp-up and ramp-down time and the exhibited *g* force or rotations speed of up to 50*g* ± 0.1*g*.

Biological samples can be exposed inside the MuSIC for seconds up to weeks, depending on the amount of growth medium and nutrients exchange necessities. If applicable, programs with varying levels of hypergravity to simulate e.g., rocket starts, or parabolic flights can be programmed. The necessary 1*g* control samples can be stored on the aluminum profile bars that hold the centrifuge rotors, so that the controls are exposed to any eventual vibrations that might affect the samples subjected to hypergravity. The whole incubator including the centrifuge unit can be sterilized with a dry-heat program to prevent any contaminations. In this thesis, 24-well plates including coverslips, 6-well plates, and 3.5 cm dishes were used for hypergravity exposure in the MuSIC. The samples had to be chemically fixated with PFA (cells on coverslips or 3.5 cm dishes) or lysed for biochemistry (6-well plates) immediately after stopping of the MuSIC as to prevent readaptation to normal gravity.

4.1.2 The Hyperscope

Samples that were exposed to hypergravity inside the MuSIC had to be chemically fixated after stopping of the centrifuge to be imaged, or otherwise they would readapt to 1*g*. To circumvent this problem and to be able to visualize dynamic changes in altered gravity, the Hyperscope was designed to enable live-cell microscopy under hypergravity conditions. The Hyperscope is a combination of the Axio Observer Z.1 live-cell fluorescence microscope (see 5.4.2) which is placed on a swing-out platform on one arm of the short-arm human centrifuge (SAHC1) situated at the DLR :envihab facility (see Figure 37). The microscope control computer is accessible via remote desktop, giving access to outside operators to all imaging functions while the centrifuge is spinning. This makes live-cell imaging of biological samples under direct hypergravity exposure of up to 2*g* possible. Since the microscope is fully automated, all functions such as filter, camera, exposure, LEDs and the x-, y- and z-drives can be controlled and adjusted during centrifugation. Due to the swing-out platform, the gravity vector acts perpendicular on the samples, preventing unwanted shear forces. The centrifuge is powered by a magnetic direct drive, allowing for a near vibration free operation.

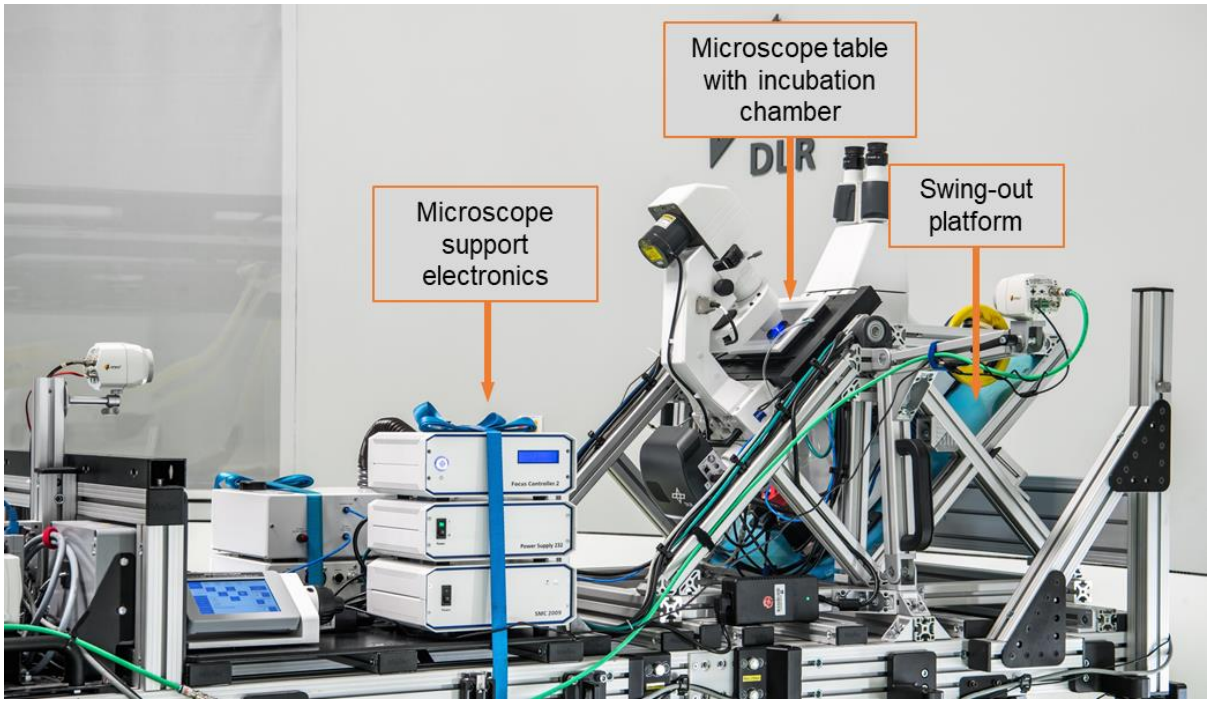

Figure 37: Side-view of the Hyperscope on one arm of the SAHC1 with the main components marked.

A PeCon incubation system is mounted on the microscope table to supply samples with steady environmental conditions, such as temperature (37°C), CO_2 (5%), and humidity (>90%) which can be controlled with the microscope software. The incubation chamber has a heated glass cover to prevent condensation. Various cell culture vessels such as Ibidi slides, chambers and 3.5 cm dishes can be used with the incubator. The microscope possesses a Definite Focus.2 physical autofocus module which keeps the sample plane in focus and mitigates focus drift caused by temperature gradients and the physical compression of material caused by centrifugation. It is equipped with an LED light source to reduce the energy and thus phototoxic potential of the excitation light. Aside from the standard excitation and emission filter cubes, a triple bandpass filter can be used to for fast multispectral image acquisition without the need to change filters between channels. The camera is a monochrome CMOS camera with a speed of up to 128 fps to be able to resolve fast processes. The Hyperscope has an indefinite runtime and centrifugation times of 24 hours have successfully been completed. For longer imaging duration or to add stimulants and other drugs to the imaging chamber, a remotely controllable peristaltic pump can be mounted on the system. Centrifugation at 2*g* requires a ramp-up time of 2 minutes, which can be prolonged in case of acceleration-sensitive samples. For all experiments, the 1*g* control samples are imaged also on the Hyperscope but without rotation, to control for any environmental changes in the centrifuge chamber.

4.1.3 Slide flask clinostat

To expose astrocytes to simulated microgravity, the slide flask clinostat was used. This fast-rotating 2D clinostat is set to 60 rpm and consists of six axes rotating in parallel that can each be loaded with four slide flasks, or a total of 24 slide flasks (see Figure 38). The clinostat principle is based on the rotation of a sample on an axis perpendicular to the normal gravity vector. This distributes the gravitational pull over 360° and thus prevents sedimentation of particles. Adherent cells such as astrocytes can be seeded in slide flasks and will adhere to the slide flask bottom which can function as a plastic microscope slide and can be removed from the flask after the experiment. The clinostat can be placed in a sufficiently sized cell culture incubator to supply the flasks with 37°C, 5% CO_2 and >90% humidity during exposure. Samples can be exposed days up to weeks and are limited to by the amount of growth medium and medium refresh necessities. Slide flasks of the 1*g* control are placed on top of the clinostat's aluminum frame so that they are exposed to eventual vibrations that might affect the samples exposed to simulated microgravity.

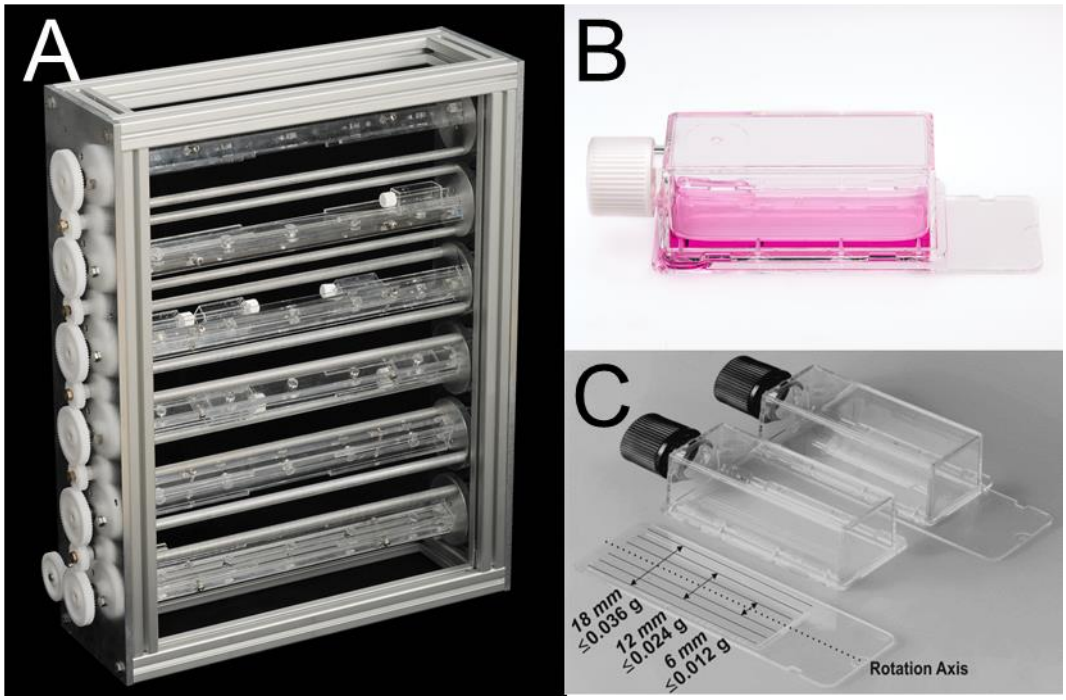

Figure 38: The slide flask clinostat (A) with a slide flask seen from the side (B) and disassembled into the slide and flask (C) with the quality of microgravity achieved in different regions of the slide (Eiermann et al.).

Simulated microgravity exposure is highly susceptible to outside disturbances such as vibration and also to shear forces induced by gas bubbles inside the slide flasks. The slide flasks are filled completely with degassed cell culture medium and any remaining bubbles are removed before closing the flasks, to avoid any shear forces. The residual acceleration depends on the effective radius of the rotation. This means that it approaches zero on the center of the axis and increases the further away a sample is on the axis. Only the growth

surface that is closest to the rotation axis is exposed to the highest quality simulated microgravity (see Figure 38C), for this reason in the microscopic analyses performed here, only this part was imaged and analyzed, excluding the cells that grew on the perimeter of the slide flasks.

4.2 Astrocyte culture

All experiments in this thesis were performed on primary embryonic murine cortical astrocytes, isolated from 18.5-day old embryos with either a wildtype C57Bl/6J or LifeAct-GFP background.

4.2.1 Preparation of primary cortical astrocytes

Primary murine astrocytes were generated from the cortices of 18.5-day old C57Bl/6J or heterozygous LAGFP/+ mouse embryos. At this point in embryonal development, a high percentage of astrocytes are present in the cortex and only few neurons or microglia which could contaminate the culture. For the dissection, a pregnant mouse was sacrificed by cervical dislocation and the embryos extracted. The single embryos were decapitated and the scalp, as well as the cranium removed with fine forceps. The brain was then transferred to a 6 cm cell culture dish containing 5 mL of prewarmed HBSS-HEPES (see 5.1.1). The dish was moved to a stereo microscope (see 5.4.1) where the following steps were performed.

A single hemisphere was removed from the brain stem, the meninges removed, and the hippocampus and olfactory bulbs removed with fine forceps. The cortex was then moved into an Eppendorf tube containing 1 mL of prewarmed HBSS-HEPES. These steps were repeated until all embryos were dissected.

The extracted cortices were moved under a laminar flow hood and transferred into a 15 mL low-bind tube and the HBSS-HEPES was aspirated. 5 mL of prewarmed Trypsin-HEPES (see 5.1.1) was pipetted onto the cortices and incubated for 15 min. in a water bath at 37°C. After the incubation, the Trypsin-HEPES was aspirated, and the cortices were washed three times with prewarmed HBSS-HEPES. Following the washing, 5 mL of prewarmed MEM-FCS (see 5.1.1) was pipetted into the tube and the cortices were dissociated by pipetting up and down with a glass Pasteur pipet until no pieces of cortices were visible. Afterwards, a fire-polished glass Pasteur pipet with approximately one third of the normal opening diameter was used to dissociate the cells and to generate a single cell solution. This solution was then seeded onto T75 Nunclon Delta flasks (see 5.3.1) with a density of 3 – 5 embryos per flask.

The cells were incubated in normal cell culture conditions for 24 hours and a complete medium exchange was performed. These P0 (passage 0) astrocytes were grown until confluency and split 1:3 (passage 1, P1) into new cell culture flasks (see 4.2.2). Remaining microglia were removed from the culture by regular medium changes and shaking the flask before aspiration

of the medium. Neuronal contamination is prevented since these cells cannot survive in MEM-FCS astrocyte medium. The purity of the astrocyte culture was controlled fluorescent staining with an antibody against the astrocyte-marker protein GFAP.

4.2.2 Passaging primary astrocytes

For passaging, a 90 - 100% confluent T75 flask of primary murine astrocytes (see 4.2.1) was first thoroughly washed with 15 mL HBSS-HEPES, the washing buffer was then completely aspirated and 5 mL of prewarmed Trypsin-HEPES was pipetted onto the cells. The flasks were tilted to distribute the solution over the whole surface. It was then incubated for 5 minutes in an incubator at 37°C. After the incubation, the flask was rigorously tapped on all sides to loosen the trypsinated cells from the growth surface. Detachment of the cells was verified under a cell culture microscope.

As a next step, 5 mL of MEM-FCS was pipetted into the flask and the whole cell solution was distributed into three fresh T75 Nunclon Delta flasks. Lastly, 10 mL fresh MEM-FCS was pipetted into each flask. After 24 hours a complete medium exchange with fresh MEM-FCS was performed.

4.2.3 Seeding astrocytes for experiments

For the multitude of conducted experiments, different cell seeding protocols were established to reach an appropriate cell density and good viability on the different cell culture vessels and microscopy cover slips. If not stated otherwise, all assays were performed using P2 (passage 2) astrocytes.

4.2.3.1 Ibidi 8-well chambers for live spreading analysis

The analysis of the initial spreading of freshly seeded astrocytes was performed on the Hyperscope. The 2*g* samples and 1*g* control samples were imaged in sequential order. To achieve the best comparability of the two paired samples, they were imaged in close temporal proximity. Thus, for each biological replicate two flasks of P1 cultured astrocytes derived from the same animal were required. The hypergravity run was started in the morning, and the 1*g* control was done analogously in the afternoon of the same day.

For the seeding procedure, one confluent T75 flask was washed with 15 mL prewarmed HBSS-HEPES and then incubated with 3 mL of Trypsin-HEPES in the incubator for five minutes. After the incubation, astrocyte detachment was checked with a cell culture microscope. The cell solution was diluted with 7 mL prewarmed MEM-FCS and transferred into a 50 mL centrifuge tube and the cell density counted.

Because of spatial limitations of the microscope incubation stage, only the four central wells of one Ibidi µ-Slide 8 Well with Ibitreat coating were seeded with 6000 cells per well. The wells

were filled up with 200 µL of MEM-FCS each and the µ-Slides were closed with Ibidi DIC lids. The remaining cell solution was split onto three new T75 flasks for cells at passage 2 (P2). Immediately after seeding, the experiment procedure and imaging protocol was started to record the early cell adhesion and spreading. Image acquisition process is explained in 4.6.3 and image analysis in 4.8.1.

4.2.3.2 Astrocytes on PLL-coated coverslips for immuno-fluorescence experiments

For high-resolution immunofluorescence microscopy following hypergravity exposure in the MuSIC, primary murine astrocytes were grown on 13 mm diameter coverslips treated as described below. Marienfeld precision cover glasses with a No. 1.5H thickness of 170 µm (see 5.3.2) were first incubated for 24 hours in porcelain racks with concentrated nitric acid (65%), then washed five times with ultrapure water and sterilized for 6 hours in 220°C dry heat. Next, the coverslips were transferred into a 24-well plate and coated with 100µL of a poly-L-lysine solution in borate buffer at a concentration of 1 mg/mL (see 5.1.1). The coating was incubated in a wet chamber for 24 hours and then washed five times with sterile ultrapure water. Finally, the coverslips were equilibrated in MEM-FCS for at least two hours at 37°C before seeding the cells by pipetting 1 mL into each well. For immunofluorescence experiments, primary murine astrocytes in P1 were used. A confluent T75 flask was washed with prewarmed HBSS-HEPES and then incubated with 5 mL prewarmed Trypsin-HEPES at 37°C. Afterwards the flask was tapped on each side to loosen the cells and dissolution was verified with a microscope. 5 mL MEM-FCS was added to the flask and the cell solution transferred to a 50 mL falcon tube. The cells were counted in a Neubauer chamber and $1.5 * 10^4$ cells were then seeded into each well. After 24 hours medium was changed completely. Staining is explained in 4.5.1 and image acquisition in 4.6.1.

4.2.3.3 Ibidi cell culture inserts for scratch assays

The migration speed of primary murine astrocytes was measured in a “scratch” or wound-healing assay. For this, Ibidi 3.5 cm Ibitreat dishes with preinserted Ibidi cell culture inserts (4-well) were utilized. The outer sides and edges of each cell culture insert were marked on the underside of each dish, to facilitate faster image acquisition with the live-cell microscope. For the wound healing experiments, primary murine P1 astrocytes were used for splitting. A confluent T75 flask was washed with prewarmed HBSS-HEPES and then incubated with 3 mL prewarmed Trypsin-HEPES at 37°C. Afterwards the flask was tapped on each side to loosen the cells and dissolution was verified with a microscope. 3 mL MEM-FCS was added to the flask and the cell solution transferred to a 50 mL falcon tube. Next, 100 µL of cell solution was

pipetted into each well of the cell culture insert, and the cells were left to adhere for 24 hours in an incubator. The next day, the medium and non-adherent cells were completely aspirated from each well, and the whole dish including the inserts was filled up with 4.5 mL of prewarmed MEM-FCS. The astrocytes inside the cell culture insert were grown to confluency for one to two weeks with regular medium changes. Image acquisition is explained in 4.3 and 4.4, image analysis is explained in 4.8.5.

4.2.3.4 Ibidi 3.5cm dishes for live-cell immunofluorescence

To be able to accurately image intracellular actin in primary astrocytes, the LifeAct-GFP mouse model was employed. The mouse line was first generated by Riedl et al. (Riedl, Crevenna et al. 2008) as Tg(CAG-GFP). The small peptide LifeAct was fused to the enhanced version of the green fluorescent protein (EGFP) to bind exclusively to filamentous actin (F-actin) without cross-detection of non-polymerized globular (G-actin). Thus, actin filaments were labelled with the GFP moiety by the LifeAct-GFP construct and were still able to polymerize in the cells without major disturbances in dynamic actin remodeling. The LifeAct-GFP transgene was expressed ubiquitously in the whole animal including astrocytes already at embryonic stage E18.5. Heterozygous LifeAct-GFP/+ breeder pairs were used to generate ca. 50% LifeAct-GFP-expressing mouse embryos in each litter. Homozygous LifeAct-GFP animals are embryonic lethal. A confluent T75 flask of LifeAct-GFP transgenic astrocytes at P1 was washed with prewarmed HBSS-HEPES and then incubated with 5 mL prewarmed Trypsin-HEPES at 37°C. Afterwards the flask was tapped on each side to loosen the cells and detachment was verified with a microscope. 5 mL MEM-FCS was added to the flask and the cell solution was transferred to a 50 mL falcon tube and to the cell number was counted with a Neubauer chamber. Sterile Ibidi 35 mm µ-Dishes with Ibitreat coating were seeded with $1 * 10^5$ cells and filled up with 3 mL MEM-FCS. The astrocytes were left to adhere in an incubator for 24 hours, and the medium was exchanged completely. From this time on, the cells could be imaged on the Axio Observer epifluorescence microscope with the PeCon incubation chamber, either under normal 1*g* laboratory conditions, or in the Hyperscope configuration for live-cell imaging under hypergravity. Image acquisition is explained in 4.6.4.

4.2.3.5 Slide flasks for simulated microgravity exposure

Primary murine astrocytes were cultured on slide flasks to be exposed to simulated microgravity on the slide flask clinostat. A confluent T75 flask of primary murine astrocytes at P1 was washed with prewarmed HBSS-HEPES and then incubated with 5 mL prewarmed Trypsin-HEPES at 37°C. Afterwards the flask was tapped on each side to loosen the cells and dissolution was verified with a microscope. 5 mL MEM-FCS was added to the flask and the cell solution was transferred to a 50 mL falcon tube. The cell solution was counted using a

Neubauer chamber so that $1 * 10^5$ cells could be seeded on each slide flask. The slide flasks were filled up with 5 mL MEM-FCS and left in the incubator for 24 hours. The next day, the medium was aspirated, and the flasks filled up completely with degassed MEM-FCS. For this the empty flasks were placed upright and slowly with a 50 mL pipet filled with MEM-FCS which was left overnight in an incubator with the bottle lid slightly opened to degas. After filling the slide flasks, they were controlled for bubbles and remaining bubbles were removed from the flask. Before screwing on the lid, a piece of U.V. sterilized parafilm was placed over the flask opening and the lid was tightly screwed on top of it. In this configuration and after repeated bubble-checks, the slide flasks could be placed on the clinostat in an incubator. The 1*g* control samples were prepared in the same way but placed on the static structure of the clinostat and not on the rotating axis. Image acquisition is explained in 4.6.1 and image analysis is explained in 4.8.2, 4.8.3, 0, and 4.8.9 respectively.

4.2.3.6 6-well plates for cytoplasmic lysates

To prepare cytoplasmic protein lysates from primary murine astrocytes exposed to hypergravity, a T75 flask derived from an individual culture was evenly split onto sufficient 6-well plates for the desired time points bot for hypergravity exposure and the 1*g* control. The astrocytes were grown to 70% confluence inside a cell culture incubator and then exposed to 2*g* hypergravity inside the MuSIC. The 1*g* control cells were cultured inside the MuSIC-incubator on the non-rotating structure. Western blotting and lysing procedures are explained in 4.7.3 and 4.7.1.

4.3 Cell migration assay on the MuSIC

Confluent astrocytes grown in Ibidi Cell Culture inserts from 4.2.3.3 were used for this experiment. Right before the start of the experiment, the silicone cell culture inserts were removed from the 3.5 cm dishes under sterile conditions and a complete medium exchange was performed. Insert stages were 500 µm wide and 4 mm long, thus 4 defined cell-free areas were uncovered upon removal of the cell culture insert with minimal harm to surrounding cells. Directly afterwards, the dishes were transferred into the MuSIC and centrifuged at 2*g* for five days. The 1*g* controls were placed on a non-rotating platform inside the MuSIC incubator which was part of the centrifuge structure to control for eventual vibrations. The MuSIC was stopped daily for approximately 20 minutes per sample to image the cell-free areas on the Zeiss Observer live-cell microscope. A transport incubator was used for transfer and an incubation chamber supplying temperature and CO_2 was installed on the microscope. Each scratch was imaged in phase contrast using a 20x long-distance air objective (Zeiss, NA 0.4 LD, Ph2, Jena, Germany). A predefined tile-setup encompassing the whole scratch area was utilized to limit

the time spent under 1*g*. Image acquisition is explained in 4.6.3 and image analysis is explained in 4.8.5.

4.4 Cell migration assay on the Hyperscope

Confluent astrocytes grown in Ibidi Cell Culture inserts from 4.2.3.3 were used for this experiment. Right before the start of the experiment, the silicone cell culture insert was removed from the 3.5 cm dish under sterile conditions and a complete medium exchange was performed. Directly afterwards, the dish was transferred onto the Hyperscope. The incubator of the microscope was set to 37°C and 5% CO_2 and the dish was inserted. An imaging program was designed to automatically image the whole scratch area every 30 minutes for 22h with a 20x long distance air objective (Zeiss, NA 0.4 LD, Ph2, Jena, Germany) using phase contrast. All 1*g* control samples and the 1*g* phases in multi-stage migration experiments were imaged on the Hyperscope with the centrifuge standing still. For acceleration to 2*g*, a 10% ramp, equaling a ramp-up time of 2 min, was utilized, and the centrifuge operator only accelerated when no image was being taken. Microscope incubator temperature, CO2-level as well as the centrifuge acceleration were continuously monitored while the experiments were performed. The matching 1*g* control and hypergravity samples from one biological replicate were sequentially imaged in close temporal proximity to each other to avoid different growth stages of the cells. The migration speed of astrocytes in the wound-healing assay was calculated from the linear regression lines. The slopes of the regression lines could be seen as the cell-free area closing speed with the unit %/h. The observed cell free area had a width of 500 µm set to 100% of the cell-free area, and the cell fronts migrated from both sides of the ”wound”. For this reason, cell migration speeds in this assay could be calculated as $Speed^{Migration}[\mu m/h] = \frac{Slope * 5}{2}$. The wound-healing assay was developed and established during this thesis.

4.5 Chemical fixation

To fix samples for immunofluorescence staining, a prewarmed solution of 4% PFA was used. Before fixation, the cells were washed once with prewarmed HBSS-HEPES before the PFA solution was pipetted onto the sample. The PFA solution was incubated for 20 minutes at 37°C. After the incubation time, most of the PFA solution was aspirated and the dishes or flasks filled up with HBSS-HEPES and stored at 4°C in the dark until further processing. A small amount of remaining PFA solution was used as a preservative during storage.

4.5.1 Staining protocol for immunofluorescence of astrocytes on coverslips

Primary murine astrocytes which were grown and fixed on coverslips were stained in a wet chamber. The coverslips were transferred to a wet chamber and washed with cold PBS before

permeabilization by flipping them onto a 100µL drop of TBS/0.2% TritonX-100 (TBS-T) and incubating for 1 minute at room temperature. As the next step, the autofluorescence was quenched by incubating the coverslips for 10 minutes at room temperature on a 100µL drop 50mM Ammonium chloride. After quenching, the coverslips were washed by slowly dipping them into cold PBS several times and blocked overnight at 4°C on a drop of 10% FCS/TBS-T to avoid unspecific binding of the antibodies. The blocked cells were incubated with the primary antibody (see 5.5.1) and, if needed, fluorophore-conjugated Phalloidin (see 5.5.3) by placing the coverslip on a 100µL drop of antibody solution diluted in 10% FCS/TBS-T and incubating overnight at 4°C in the wet chamber. On the next day, the coverslips were washed by slowly dipping them into cold PBS several times and then incubating them on a drop of TBS-T for 10 minutes three times. The secondary antibodies (see 5.5.2) were diluted in 10% FCS/TBS-T and incubated with the cells in a 100µL drop for 2 hours at room temperature. After the secondary antibody incubation, the coverslips were washed three times by dipping them into cold PBS and incubating them on a drop of cold PBS for 10 minutes. For mounting, the coverslips were placed on a microscopy slide with a drop of 16µL Everbrite Hardset Mounting Medium with DAPI. The mounted coverslips were left to cure in the dark at room temperature for at least 24 hours before imaging. Negative controls with either only primary or only secondary antibodies incubated were prepared in parallel to the fully stained samples.

4.5.2 Staining protocol for immunofluorescence of astrocytes on slide flasks

Primary murine astrocytes which were grown and fixed on slide flasks were stained in a wet chamber. Before the first staining step, the flask lids were separated from the slides with the proprietary tool. The slides were washed with cold PBS and then permeabilized by pipetting 250µL TBS/0.2% TritonX-100 (TBS-T) onto the growth area of the cells and incubating for 1 minute at room temperature. In the next step, autofluorescence was quenched by incubating the slides for 10 minutes at room temperature with 250µL of 50mM Ammonium chloride. After quenching, the slides were washed by slowly dipping them into cold PBS several times and blocked overnight at 4°C with 250µL of 10% FCS/TBS-T. A piece of parafilm was cut to fit on top of the liquid to prevent evaporation. The blocked cells were incubated with the primary antibody (see 5.5.1) and, if needed, fluorophore-conjugated Phalloidin (see 5.5.3) by pipetting 180 µL of antibody solution diluted in 10% FCS/TBS-T onto the slide and incubating overnight at 4°C in the wet chamber with a piece of parafilm as cover. On the next day, the slides were washed by slowly dipping them into cold PBS several times and then incubating them with 250µL of TBS-T for 10 minutes three times. The secondary antibodies (see 5.5.2) were again diluted in 10% FCS/TBS-T and incubated with the cells for 2 hours at room temperature. After the secondary antibody incubation, the slides were washed three times by dipping them into

cold PBS and incubating them with 250µL cold PBS for 10 minutes. For mounting, 50µL of Everbrite Hardset Mounting Medium with DAPI was pipetted onto the slides and a highest quality No. 1.5H 24mm x 60mm coverslip was placed on top of the slide. The mounted slides were left to cure in the dark at room temperature for at least 24 hours before imaging. Negative controls with either only primary or only secondary antibodies incubated were prepared in parallel to the fully stained samples.

4.5.3 Annexin V / PI apoptosis assay

For the apoptosis/necrosis assay, primary murine astrocytes were grown in 24-well plates on PLL-treated coverslips and exposed to hypergravity in the MuSIC. Annexin-V is a protein specifically recognizing apoptotic cells by binding phosphatidyl-serine amino acid-residues that are exposed on the outer layer of plasma membrane already during early stages of apoptosis. Propidium iodide is a DNA stain, which can only enter the cell through holes in the cell membrane, correlating with later stages of apoptosis.

The 1*g* control samples were treated similarly without centrifugation. The staining mix was prepared from Annexin V binding buffer (see 5.1.3) with the Annexin V-protein conjugated to Atto488 (see 5.5.3) at a concentration of 2.5µg/mL and Propidium iodide at a concentration of 0.1 mg/mL (see 5.5.3). After hypergravity exposure, the 24-well plates were removed from the MuSIC and quickly washed once in HBSS-HEPES. To minimize the exposure of the hypergravity samples to normal gravity and avoid unwanted readaptation, all incubation steps were performed inside the MuSIC during active centrifugation. After washing, 100 µL of the prepared staining mix was pipetted into each well and incubated in the MuSIC in darkness at 37°C for 20 minutes. After incubation, the coverslips were washed once with HBSS-HEPES and fixed in 4% PFA for 20 minutes at 37°C. Negative controls were treated similarly, but without the incubation in staining solution.

4.6 Microscopy and analysis

Astrocytes were imaged after fixation in epifluorescence and STED microscopy and live cells via DIC, phase contrast and epifluorescence microscopy. These different techniques required verified and standardized microscope settings to be comparable and yield relevant results. Analysis of these images was performed with the software Zeiss Zen or ImageJ.

4.6.1 Epifluorescence microscopy of fixed cells

Fixed astrocytes were stained as described above (see 4.5.1 and 4.5.2) and imaged with the Zeiss Axio Observer.Z1 epifluorescence microscope (see 5.4.2). For every fluorophore or dye, the LED power and exposure time with the least background and the highest dynamic range was established. Most samples were imaged using the tiling mode with many single fields of

view taken in one project to be stitched together by the software. A tile overlap of 5% was defined and an appropriate number of focus support points distributed over the tile area. After setting the z-plane for every focus support point the image was acquired and then stitched by the Zeiss Zen stitching algorithm. Using this approach, a high number of cells could be imaged. The following settings were used for the experiments. For each experiment, exposure times, filters, and camera settings were constant in between the replicates.

Experiment	Paragraph	Objective	Fluorophore: LED (Power)	Exposure	Tiles
Spreading, Morphology MuSIC	2.1.1.2, 2.1.1.3, 2.1.1.4, 2.3	25x, oil	DAPI: 385 nm (50%) Atto550: 567 nm (50%)	200 ms 400 ms	450
Annexin V / PI	2.1.1.5	25x, oil	DAPI: 385 nm (50%) Atto488: 475 nm (20%) PI: 567 nm (50%) Atto633: 630 nm (20%)	22 ms 818 ms 150 ms 150 ms	96
Proliferation (Ki67)	2.1.1.5	25x, oil	DAPI: 385 nm (50%) Atto488: 475 nm (20%) Atto550: 567 nm (50%)	22 ms 44 ms 400 ms	100
GFAP, LZK	2.2.1 / 2.2.2	25x, oil	DAPI: 385 nm (50%) Atto488: 475 nm (20%) Atto550: 567 nm (50%) Atto633: 630 nm (20%)	22 ms 818 ms 150 ms 150 ms	96
Vimentin, nestin	2.2.2	25x, oil	DAPI: 385 nm (50%) Atto488: 475 nm (20%) Atto550: 567 nm (50%) Atto633: 630 nm (20%)	22 ms 818 ms 150 ms 150 ms	96
Morphology, GFAP clinostat	2.8.1, 2.8.2, 2.8.3 2.8.5	25x, oil	DAPI: 385 nm (50%) Atto488: 475 nm (30%) Atto633: 630 nm (50%)	30 ms 300 ms 500 ms	96
Proliferation clinostat	2.8.4	25x, oil	DAPI: 385 nm (50%) Atto488: 475 nm (40%)	68 ms 200 ms	132
Tubulin clinostat	2.8.6	25x, oil	DAPI: 385 nm (50%) Atto488: 475 nm (30%) Atto550: 567 nm (50%) Atto633: 630 nm (50%)	30 ms 600 ms 2.2 s 500 ms	96

4.6.2 STED microscopy

To image astrocyte cytoskeletal components in super-resolution, the Abberior Infinity Line STED microscope (see 5.4.2) was employed. Stimulated Emission Depletion (STED) microscopy is able to achieve super resolution through the use of two lasers and can thus circumvent Abbe's law of the diffraction limit set by the excitation wavelength used. The STED depletion laser (775 nm) has a ring form, which temporary de-excites or quenches all fluorophores in the region. The center spot where the depletion laser is inactive can be excited with an excitation laser (561 nm or 640 nm) and can be engineered to be as small as 30 nm. Since after de-excitation of the surrounding fluorophores, only this small, defined spot of the sample can be excited and the emitted photons detected. Only specific secondary antibodies can be used for STED microscopy as the fluorophores must tolerate repeated quenching by

the de-excitation laser. During this thesis a screening of matching secondary antibodies was performed to establish STED microscopy in astrocytes. The laser settings for excitation and STED lasers were similarly tested and the achieved resolution was measured by the half width of the maximum intensity peak of a fluorescent signal per fluorescent dye channel. These procedures resulted in the following settings for the STED microscope.

Experiment	Paragraph	Objective	Fluorophore: LED (Power)	Detector	Pixel size	Dwell time
Cytoskeleton STED	2.5	60x, oil	DAPI: 405 nm (04%) Atto542: 561 nm (26%) STED 775 nm (20%) StarRed: 640 nm (4%) STED 775 nm (20%)	571-630 nm 650-755 nm	40 nm	5 µs

4.6.3 Wide field imaging

The live spreading and migration experiments were performed using the wide field with phase contrast and differential interference contrast (DIC) and if applicable time-lapse capabilities of the Zeiss Axio Observer.Z1 microscope. For live cell imaging, the physical auto focus function of the Definite Focus 2 module was used. This module uses an infrared laser aligned with the objective to measure the exact distance between the sample and the objective by refraction of the laser at the sample plane.

Experiment	Paragraph	Objective	LED (Power)	Exposure	Interval	Tiles
Initial spreading	2.5	40x, oil, DIC	TL (49%)	800 µs	30 min	70
Migration MuSIC	2.4.1	20x, air, Ph 1	TL (51%)	24 ms	Daily	66
Migration Hyperscope	2.4.2, 2.4.3	20x, air, Ph 1	TL (52%)	9 ms	30 min	86

4.6.4 LifeAct-GFP fluorescent live-cell imaging

To visualize the dynamics of actin fibers under hypergravity, primary murine astrocytes generated from LifeAct-GFP transgenic mice were imaged on the Hyperscope. These mice express a peptide which is coupled to GFP and binds to filamentous (F-) actin, hereby staining the actin cytoskeleton. Imaging protocols for these cells had to be optimized to prevent phototoxicity and apoptosis in the sample. Several test runs with different LED power settings (20%, 5%, and 2%) and exposure times, and imaging intervals were tested until a combination of microscope settings was found that did not cause dystrophic changes in the cells even after several hours of continued imaging. Ibidi 3.5 cm dishes were finally chosen as vessels for the imaging procedures, as they allow cell growth and adherence with high resolution, oil immersion microscopy.

Experiment	Paragraph	Objective	LED (Power)	Exposure	Interval	Tiles
LAGFP imaging	2.6	40x, oil	GFP 475 nm (2%)	200 ms	2.5 min	169

4.7 Biochemistry

4.7.1 Cytoplasmic Lysates

Astrocyte cytoplasmic lysates were prepared from cells cultured in 6-well plates (see 4.2.3.6) and exposed to hypergravity in the MuSIC. After exposure, the hypergravity- and control samples were removed from the MuSIC and quickly washed once with cold PBS. On ice, 80 µL of TLB with protease inhibitor (see 5.1.2) were pipetted into each well and the cells were scraped off. The TLB buffer lyses the cell membrane, but not the nuclear envelope. The lysates from all wells of one plate were pooled into a 1.5 mL tube and incubated on ice for 10 minutes. After incubation, the lysates were centrifuged at 14.000 rpm and 4°C for 10 minutes and the supernatant transferred into fresh 1.5 mL tubes. Protein concentration in each lysate was determined via BCA assay (see 4.7.2), afterwards the lysates were boiled in 1x sample buffer at 99°C for 10 minutes, aliquoted in 100 µL volumes, and stored at -20°C until use.

4.7.2 BCA assay

To ensure equal loading of the gels used for the SDS Page, the protein concentration in cytoplasmic lysates had to be determined. For this, the Pierce BCA Protein Assay Kit (see 5.2.3) was used. The BCA assay relies on the reduction of Cu^{+2} to Cu^{+1} by proteins, which is called the biuret reaction. This reduction is then colorimetrically detected using a reagent containing bicinchoninic acid (BCA). BCA reacts with Cu^{+1} to form a purple-colored reaction product which can be detected in a plate reader by its absorbance at 562nm. For the BCA assay, a working reagent has to be freshly prepared by mixing the BCA reagents A and B by 50:1. Next, 25 µL of each lysate, as well as protein standards with defined BSA concentrations and a negative control consisting of pure TLB with protease inhibitor were pipetted into a 96 well plate. All measurements were done in triplicates. Then, 200 µL of the BCA working reagent were pipetted into the wells and the solutions mixed for 30 s on an orbital shaker. The 96 well plate was then incubated at 37°C in an incubator for 30 min. After the incubation, the absorption of the samples was measured in a plate reader at 562nm. Using the protein standards, a standard curve was created from which the concentration of the protein lysate samples could be calculated.

4.7.3 SDS-PAGE and Blotting

An SDS-PAGE (sodium dodecyl sulfate polyacrylamide gel electrophoresis) was employed to separate proteins in the cytoplasmic lysates (see 4.7.1) by their molecular weight. It relies on the masking of the protein's intrinsic charges by SDS molecules, thus separating them only by

their size. For the SDS-PAGE, precast Bio-Rad Mini-Protean 12% gels were used (see 5.2.3). These gels consist of a stacking gel with a neutral pH in which the proteins are stacked near the border of the separation gel using a relatively low voltage. By increasing the voltage, the negatively-charged proteins travel into the direction of the positively charged anode. Smaller proteins travel faster through the pores in the gels, so that the proteins are separated by their size.

Two gels were placed into the gel holder and inserted into the running chamber in SDS running buffer (see 5.1.2). The amount of 15µg of cytoplasmic protein lysate was loaded into each well. The two outermost lanes were used to load 3µL of the PageRuler prestained protein ladder (see 5.2.3). The gels ran at 80V for 30 minutes to stack the proteins in the stacking gel and then at 150V for 1.5 hours to separate them by molecular weight in the separation gel.

After the electrophoresis, the gel was extracted from the gel holder and the stacking gel removed. The separation gel containing the proteins was placed on top of a methanol-activated Amersham PVDF membrane (see 5.2.3) which was then sandwiched between blotting papers and sponges in a gel holder cassette. Two of these cassettes, containing one gel each, were placed in the electrode assembly and submerged in a blotting tank filled with Towbin transfer buffer (see 5.1.2). The proteins in the gels were then transferred onto the blotting membrane by submerged transfer at 4°C with 20V overnight. The next morning, the blotting tank was disassembled and the membranes retrieved. The membranes were blocked for 1 hour at room temperature in 5% milk/NCP to prevent unspecific binding of the antibodies, and the primary antibodies (see 5.5) were diluted in milk/NCP (see 5.1.2) and incubated overnight at 4°C. At the same time, the gel was stained with Coomassie gel staining solution (see 5.1.2) for 20 minutes and then photographed with the Intas Chemostar Touch gel scanner to control that most of the protein was transferred onto the membrane. After incubation with the primary antibodies, the membrane was washed three times for 15 minutes in NCP (see 5.1.2) and incubated with the secondary antibody coupled to the enzyme horse radish peroxidase (HRP) diluted in milk/NCP for 2 hours at room temperature. After secondary antibody incubation, the membrane was again washed three times for 15 minutes in NCP and the ECL detection was started. For ECL detection, the Pierce ECL Western Blotting Substrate was employed (see 5.2.3). It consists of two reagents, which are a peroxide solution and a Luminol solution. 1.5 mL of each solution was mixed and incubated with the membrane for 2 min, and the membrane placed in the Intas Chemostar Touch gel scanner. The protein-bound HRP then reduced the peroxides in the solution, thereby catalyzing the Luminol chemiluminescence reaction. The emitted photons were detected in an additive scanning mode for 60 minutes in total. The number of photons detected on the membrane was equivalent to the amount of protein.

4.8 Image analysis with Zeiss Zen

To detect and analyze cells and intracellular structures, the image analysis module of the Zeiss Zen software (see 5.6) was used. With this semi-automated analysis suite, cells or features could be detected in fluorescence or wide field channels of whole images or in regions of interest (ROIs). Geometrical measurements, relative intensity, metadata, and multidimensional imaging data was read out from a large number of samples. For each of the following analyses, an image analysis program was defined as follows. To analyze cellular morphology, the Zeiss Zen Image Analysis Wizard was employed. An object class was created in the Phalloidin-stained fluorescence channel and it was set to be segmented by variance-based thresholding. The minimum variance was manually adjusted for every experiment to detect the Phalloidin-stained cell perimeter and the maximum variance was set to the maximum value. Through this algorithm and using the “fill holes” function which fills free areas inside detected objects, most imaged cells could be detected reliably and with detailed cell perimeter resolution. A region filter with a minimum object area of 200 µm² was employed to filter out debris and staining artifacts. As a last step, the image and all detected objects were manually controlled for artifacts and multicellular clusters which were removed to attain only single cells for the morphological analysis.

4.8.1 Initial Spreading

To measure the spreading speed of single astrocytes directly after seeding, DIC time-lapse tile-images of cells seeded into Ibidi 8-well µ-Slides were acquired (see 4.2.3.1). Adhering and spreading cells were identified in the first frame of the image and regions of interest fitted around ca. 50 these cells per condition. The ROIs were then extracted from the large image and analyzed with the Zeiss Zen image analysis module. Cells in each ROI were localized using variance-based thresholding to separate the cell perimeter from the substrate and determine the cell area, by setting the threshold values correctly, depending on the brightness and contrast of the image. The image segmentation was controlled and if needed corrected manually for each frame in case the image contrast or fidelity did not suffice to automatically detect the cell perimeter. With this approach, the enlargement in cell area over time for every selected cell could be measured and analyzed.

4.8.2 Cell spreading and morphology on fixed samples

Multiple cellular morphology parameters were measured by analyzing fluorescence images of fixed cells with the image analysis module. For all morphology analyses, variance-based thresholding was applied to the Phalloidin fluorescence channel, since the actin at the cell perimeter was robustly stained and thus easily detectable by the program. After setting the threshold values to correctly detect all cells in the image, dead or dying cells as well as debris

were excluded by setting a low cut off value of 200 µm². The segmentation in each image was controlled manually to fix incompletely detected cells and to remove cell clusters that were detected as one cell and would otherwise falsify the results. Between 2000 and 3000 single cells were detected for each condition. For these cells, various morphological perimeters were read-out: area in µm², perimeter in µm, and the circularity, which was calculated from cell area and Feret maximum according to the formula: $\sqrt{\frac{4 * Area}{\pi * Feret\ Max^2}}$. A perfectly round cell or a circle would have a circularity of 1 whereas more elongated or coarse shapes will have a decreasing circularity approaching 0.

Other parameters were the Feret minimum, maximum, and ratio. Within the cell outline in 2D as detected semi-automatically by Zeiss Zen, the program placed two straight lines on opposite sides of the detected cell area and measured their distance. These straight lines were then rotated in 32 angle positions. The shortest measured distance was the Feret minimum (see Figure 14D, bright blue line). The Feret maximum was the longest of such distances, respectively (see Figure 14C, bright blue line). The Feret ratio was calculated from $\frac{FeretMin}{FeretMax}$.

4.8.3 Fluorescence intensity of reactivity markers

Fluorescence images of fixed cells were analyzed to determine the fluorescent intensity of astrocyte reactivity marker proteins (see 4.8.2). A wide range of literature was screened to find appropriate astrocyte reactivity markers in addition to the widely used protein GFAP. Several marker proteins were selected and antibody staining protocols were established for several marker staining combinations. The target reactivity markers GFAP, nestin, LZK and vimentin were stained and additionally Phalloidin was used to stain F-actin. In the image analysis module of the Zeiss Zen software (see 5.6), F-actin was used with the variance-based method to detect cells and the fluorescence values of the channels in which the reactivity markers had been imaged were read out inside the detected boundaries of the cells. The mean fluorescence intensity of each fluorescence channel in every cell was then read out by the software and could be analyzed.

4.8.4 Nucleus morphology

Nuclear morphology was determined by imaging fixed cells stained with DAPI and analyzing the fluorescence microscopy images with the image analysis module of the Zeiss Zen software. Variance-based thresholding was employed to detect nuclei in the DAPI channel and the thresholds were set accordingly. After segmentation, each image was controlled manually to exclude artefacts and separate nuclei that were too close to each other and got detected as one. The same morphological parameters as described for cell morphology analysis were employed (see 4.8.2) to analyze the detected single nuclei.

4.8.5 Wound-healing assay

To analyze “scratch” or wound-healing assays (see 4.2.3.3), the cell free area of the scratch was detected by using the variance-based thresholding function of the image analysis module of the Zeiss Zen software. The threshold values were set so that the two opposing cell fronts were not detected as objects, but the cell free area between them was detected. For each image and frame the detected area was controlled manually for holes where dirt or cell debris was wrongly detected. This resulted in one area value per scratch per frame that could be analyzed further as a x/y graph from which linear regression lines could be generated. The slopes of the regression lines could be seen as the cell-free area closing speed with the unit %/day. The observed cell free area had a width of 500 µm set to 100% of the cell-free area, and the cell fronts migrated from both sides of the ”wound”. For this reason, cell migration speeds in this assay could be calculated with the following equation $Speed^{Migration}\ [\mu m/h] = \left(\frac{Slope * 5}{2}\right)$.

4.8.6 Annexin V and propidium iodide cell death assay

To calculate the ratio of Annexin V-positive astrocytes in a sample, first the total number of cells in the microscopy images was calculated by detection of all nuclei through DAPI staining analysis as described in 4.8.4. Next, all cells showing a positive Annexin V fluorescence signal were counted by hand and divided by the total cell number. For late apoptosis, all Annexin V and propidium iodide-positive cells were counted by hand and divided by the total cell number.

4.8.7 Ki-67 proliferation assay

To calculate the ratio of proliferating and non-proliferating astrocytes, the total cell number in the samples was determined by detection of all nuclei through DAPI staining as described in 4.8.4. The number of Ki-67-positive nuclei was similarly determined by using the variance-based thresholding function of the Zeiss Zen image analysis program to detect fluorescent nuclei in the Ki-67 fluorescence channel. The number of these fluorescent nuclei was then divided by the total number of cells to calculate the ratio of proliferating cells in the sample.

4.8.8 GFAP expression quantification

To quantify the number of GFAP-expressing cells in a sample, first the total number of cells in each image was determined by the detection of their nuclei through DAPI staining (see 4.8.4). Next, all cells expressing a strong GFAP signal, characterized by a clearly visible intracellular GFAP intermediate filament network, were counted by hand and divided by the total cell number.

4.8.9 Microtubule stability

Analogous to previous publications (Wuest, Arnold et al. 2020) the fluorescently-stained microtubule networks in astrocytes exposed to s-µ*g* and normal gravity were classified into three categories. By visual inspection of single cells, they were then sorted into category 1 (well-defined microtubule network), category 2 (few well-defined microtubules), and category 3 (diffuse cloud). Using Zeiss Zen, regions of interest with a defined size were overlaid on the microscopy images and cells were marked with three different point markers according to their microtubule status. The numbers of cells sorted into these three categories were then exported from the software for further analysis.

4.9 Statistical analysis

All statistical analyses were performed using the program Graphpad PRISM 9. Raw data was filtered for outliers with the ROUT method set to an aggressiveness of 1% (Motulsky and Brown 2006). Column data of two conditions (1*g* and 2*g* or s-µ*g*), or single time points of x/y data graphs were compared by employing a parametric unpaired t-test. The same method was used to compare column data of the same condition at different time points. To compare the similarity of x/y data curves, the nonparametric Mann-Whitney rank sum test was used.

For all graphs, if not stated otherwise, data is shown as mean ± SEM (standard error of the mean).

5. Material

5.1 Solutions and buffers

5.1.1 Solutions for astrocyte culture

Name	Substance	concentration
MEM-HS/FCS	MEM (10x) Glucose (20%) $NaHCO_3$ (5,5%) L-glutamine (200 mM) MEM essential amino acids (50x) MEM non-essential amino acids (100x) Horse serum (HS)/fetal calf serum (FCS), heat-inactivated @ 56°C Ultrapure water	50 mL 15 mL 20 mL 5 mL 10 mL 10 mL 50 mL to 400 mL adjust pH to 7.3 fill up to 500 mL filter sterile
HBSS-HEPES	HBSS 10x HEPES 1 M pH 7.25	50 mL 700 µL filter sterile
Trypsin-HEPES	Trypsin/EDTA (0.05%) HEPES 1 M pH 7.25	100 mL 3.5 mL
4% PFA for fixation	PFA PBS	4% filter sterile
Borate buffer	Boric acid Borax Ultrapure water	1.24 g 1.9 g to 400 mL filter sterile
PLL coating solution 1mg / mL	Poly-L-Lysine hydrobromide Borate buffer	1 mg 1 mL filter sterile

5.1.2 Solutions for biochemistry

Name	Substance	concentration
SDS-loading buffer 5x (SDS-sample buffer 5x)	Tris-HCl pH 6.8 Glycerol SDS β-mercaptoethanol Bromphenole blue	110 mM 20% 3.8% 8% ad libitum
SDS-running buffer 10x	Tris Glycine SDS (20%)	0.25 M 1.92 M 1%
Triton lysis buffer (TLB)	NaCl Tris-HCl pH 7.4- 8 TritonX-100 Complete protease inhibitor, EDTA-free, Roche	150 mM 50 mM 1% 1x
Towbin transfer buffer 1x	Tris Glycine methanol	25 mM 192 mM 20%

NCP 10x pH 8-8.2	NaCl	1.47 M
	Tris	0.4 M
	Tween-20	0.5%
	HCl 6 M	ca. 40-45 mL
Coomassie gel destain (fixation solution)	Methanol	40%
	Acetic acid	10%
Coomassie gel staining solution	Methanol	50%
	Acetic acid	10%
	Coomassie Brilliant Blue G-250	0.1%
Coomassie gel destain (washing solution)	Methanol	20%
	Acetic acid	10%

5.1.3 Solutions for immunofluorescence

Name	Substance	concentration
TBS 10x	Tris-HCl pH 7.4	400 mM
	NaCl	1.5 M
TBS-T	TBS	1x
	Triton-X 100	0.2%
Blocking solution	FCS	10%
	TBS-T	1x
Annexin V binding buffer (10x)	HEPES / NaOH pH 7.4	0.1 M
	NaCl	1.4 M
	$CaCl_2$	25 mM

5.2 Chemicals and reagents

5.2.1 Solid chemicals

Name	Company
Poly-L-lysine hydrobromide	Sigma
Ammonium chloride	Roth
Borax	Roth
Boric acid	Roth
Bovine serum albumin	Roth
Bromphenol blue	Roth
cOmplete™, EDTA-free Protease Inhibitor Cocktail	Roche
Coomassie brilliant blue	Roth
Glucose	Roth
NaCl	Roth
NaHCO3	Roth
NaOH	Roth
Non-fat milk powder	Roth
Paraformaldehyde	Roth
Tris	Roth

5.2.2 Liquid chemicals

Name	Company
Acetic acid	Roth
DPBS, (10x)	PAN Biotech
Ethanol, 70%	Roth
FCS standard	PAN Biotech
HBSS, (10x)	PAN Biotech
HS standard	PAN Biotech
Isopropanol	Roth

L-Glutamine 200 mM	PAN Biotech
MEM (100x)	Gibco
MEM Amino Acids Solution (50x)	PAN Biotech
MEM NEAA, Non-Essential Amino Acid Solution (100x	PAN Biotech
Methanol	Roth
Triton-X 100	Roth
Trypsin 0.05 %/EDTA 0.02 % in PBS	PAN Biotech

5.2.3 Commercial solutions and kits

Name	Company
12% Mini-PROTEAN® TGX Precast Protein Gels 10-well	Bio-Rad
12% Mini-PROTEAN® TGX Precast Protein Gels 12-well	Bio-Rad
Amersham ECL Prime Blot Detection Kit	Amersham
EverBrite solid mounting medium	Biotium
Hybond PVDF membrane	Amersham
PageRuler prestained protein ladder 180 kDa - 10 kDa	Thermo Scientific
Pierce BCA protein assay kit	Thermo Scientific

5.3 Laboratory material

5.3.1 Plastic ware

Name	Company
µ-Dish 35 mm	Ibidi
µ-Slide 8-Well	Ibidi
24-well plates	VWR
60 mm cell culture dish	VWR
6-well plates	VWR
Cell culture insert 4-Well	Ibidi
Centrifuge Tubes 15 mL / 50 mL	Labsolute
Centrifuge Tubes 15 mL Low-Bind	Corning
Eppendorf Tubes (0.5 mL, 1.5 mL, 2 mL)	Eppendorf
Filtration unit complete, 500 mL	Labsolute
Nunclon Delta 60 mm dishes	ThermoFisher
Nunclon Delta 6-well plates	ThermoFisher
Pipette tips (20 µL, 200 µL, 1000 µL)	Labsolute
Pipettes (1 mL, 2 mL, 5 mL, 10 mL, 25 mL, 50 mL)	Roth
Slide Flask	ThermoFisher

5.3.2 Glass ware

Name	Company
Cover Slips 13 mm 1.5H	Marienfeld
Glass bottles (50 mL, 100 mL, 250 mL, 500 mL, 1000 mL, 2000 mL)	Schott
Microscope Slides	VWR
Pasteur Pipettes (short, long)	VWR
Plugged Pasteur Pipettes (short, long)	VWR

5.4 Technical equipment

5.4.1 General technical equipment

Name	Company
Cell culture vacuum pump	Integra

Cell culture microscope AxioVert.A1	Zeiss
Chemostar Touch Gel Imager	Intas
Clean Bench Herasafe	Thermo Scientific
Cooling Centrifuge	Eppendorf
Freezer -20°C	Liebherr
Freezer -80°C	Panasonic
Fridge	Liebherr
Heating block	Thermo Scientific
Incubator CB220	Binder
Microliter Pipettes	Eppendorf
pH-Meter Lab 860	Schott instruments
Pipet-Boy	Integra
SDS Gel running and blotting chamber	Bio-Rad
SDS-Page Power supply	Bio-Rad
Stereo microscope SMZ1500	Nikon
Table centrifuge	LLG Labware
Transport incubator	Labotect
Vortex	Scientific Industries
Water Bath SW23	Julabo
Water purifier	Millipore

5.4.2 Microscopes

Zeiss Axio Observer.Z1 epifluorescence microscope

Part	
Body	Axio Observer.Z1
Camera	Axiocam 702: 2.3 MP, 5.86 µm x 5.86 µm, 128 fps, Axiocam 705: 5.07 MP, 3.45 µm x 3.45 µm, 60 fps
Light Source	Colibri 7 LED: 385 nm, 475 nm, 555 nm, 590 nm, 630 nm
Filters	DAPI (49), eGFP (38 HE), Alexa 555(Cy3) (43 HE), mCherry (64 HE), Cy5 (50 HE)
Objectives	Air: LD Plan-Neofluar 20x/0.4 corr. Oil: LD LCI Plan-Apochromat 25x/0.8 corr.; Plan-Apochromat 40x/1.4
Incubation:	PeCon Heating Insert P 2000, Incubator HF 2000

Abberior Infinity Line LSM/STED microscope

Part	
Body	Olympus IX 83
Detectors	3x APD spectral detectors with by 1 nm adjustable band-pass filters
Lasers	405 nm (cw), 485 nm (pulsed), 561 nm (pulsed), 640 nm (pulsed)
Objectives	Oil: UPLANXAPO60XO 60x/1.42

5.5 Antibodies and dyes

5.5.1 Primary antibodies

Antigen	Host Species	Company	Dilution	Condition
FAK	rabbit	Synaptic Systems	1:500	o.n. ,4°C
GAPDH	mouse	abcam	1:1000	2h, RT
GFAP	guinea Pig	Synaptic Systems	1:500	o.n. ,4°C
GFAP	chicken	abcam	1:500	o.n. ,4°C
Ki67	rabbit	Thermo	1:500	o.n. ,4°C

MAP3K13	rabbit	Sigma	1:500	o.n. ,4°C
Nestin	mouse	Merck	1:100	o.n., 4°C
Rac1	rabbit	abcam	1:250	o.n., 4°C
Rac3	rabbit	abcam	1:250	o.n., 4°C
RhoA	rabbit	abcam	1:250	o.n., 4°C
RhoG	rabbit	abcam	1:250	o.n., 4°C
Vimentin	chicken	Sigma	1:1000	o.n., 4°C
α-Tubulin	mouse	Sigma	1:500	o.n., 4°C

5.5.2 Secondary antibodies

Antigen Species	Conjugate	Host Species	Company	Dilution	Condition
Mouse	Atto-488	Goat	Attotech	1:1000	2h, RT
Rabbit	Atto-488	Goat	Attotech	1:1000	2h, RT
Mouse	Atto-550	Goat	Attotech	1:1000	2h, RT
Rabbit	Atto-550	Goat	Attotech	1:1000	2h, RT
Mouse	Atto-647	Goat	Attotech	1:1000	2h, RT
Rabbit	Atto-647	Goat	Attotech	1:1000	2h, RT
Mouse	Star Red	Goat	Abberior	1:500	2h, RT
Guinea pig	Alexa Fluor 488	Goat	ThermoFisher	1:1000	2h, RT
Chicken	Alexa Fluor 488	Goat	ThermoFisher	1:1000	2h, RT
Rabbit	HRP	Goat	Sigma	1:2000	1h, RT
Mouse	HRP	Donkey	Jackson	1:2000	1h, RT

5.5.3 Dyes

Dye type	Conjugate	Company	Dilution	Condition
Phalloidin	Atto-488	Attotech	1:250	o.n., 4°C
Phalloidin	Atto-542	Attotech	1:250	o.n., 4°C
Phalloidin	Atto-633	Attotech	1:250	o.n., 4°C
Annexin V	Atto-488	Enzo	1:20	30 min, 37°C
DAPI		Sigma	1:100	1h, RT
Propidium Iodide		ThermoFisher	1:10	10 min, RT

5.6 Software

Epifluorescence image acquisition, processing, and analysis: Zeiss Zen 3.1

Super-resolution STED image acquisition: Abberior Imspector

Super-resolution STED image processing: ImageJ (FIJI) 1.52e

Documents and tables: Microsoft Word and Excel, Endnote 20

Western blot analysis: Licor Image Studio lite

Statistics and graphs: Graphpad PRISM 9

Graphics: Biorender

6. References

A. Tschopp, A. C. (1983). "Hypergravity promotes cell proliferation." Experintia **39**(12): 1323 - 1438.
Agulhon, C., T. A. Fiacco and K. D. McCarthy (2010). "Hippocampal short- and long-term plasticity are not modulated by astrocyte Ca2+ signaling." Science **327**(5970): 1250-1254.

Agulhon, C., M. Y. Sun, T. Murphy, T. Myers, K. Lauderdale and T. A. Fiacco (2012). "Calcium Signaling and Gliotransmission in Normal vs. Reactive Astrocytes." Front Pharmacol **3**: 139.

Allen, N. J. and C. Eroglu (2017). "Cell Biology of Astrocyte-Synapse Interactions." Neuron **96**(3): 697-708.

arianespace (2012). "Soyuz User's Manual." (2.0).

Battaglia, R. A., S. Delic, H. Herrmann and N. T. Snider (2018). "Vimentin on the move: new developments in cell migration." F1000Res **7**.

Bazargani, N. and D. Attwell (2016). "Astrocyte calcium signaling: the third wave." Nat Neurosci **19**(2): 182-189.

Biedzinski, S., G. Agsu, B. Vianay, M. Delord, L. Blanchoin, J. Larghero, L. Faivre, M. Thery and S. Brunet (2020). "Microtubules control nuclear shape and gene expression during early stages of hematopoietic differentiation." EMBO J **39**(23): e103957.

Blanchoin, L., R. Boujemaa-Paterski, C. Sykes and J. Plastino (2014). "Actin dynamics, architecture, and mechanics in cell motility." Physiol Rev **94**(1): 235-263.

Block, J., D. Breitsprecher, S. Kuhn, M. Winterhoff, F. Kage, R. Geffers, P. Duwe, J. L. Rohn, B. Baum, C. Brakebusch, M. Geyer, T. E. Stradal, J. Faix and K. Rottner (2012). "FMNL2 drives actin-based protrusion and migration downstream of Cdc42." Curr Biol **22**(11): 1005-1012.

Bradbury, E. J. and L. M. Carter (2011). "Manipulating the glial scar: chondroitinase ABC as a therapy for spinal cord injury." Brain Res Bull **84**(4-5): 306-316.

Braun, M., M. Böhmer, D.-P. Häder, R. Hemmersbach and K. Palme (2018). Gravitational Biology I Gravity Sensing and Graviorientation in Microorganisms and Plants. G. Ruyters and M. Braun, Springer.
Burridge, K. and C. Guilluy (2016). "Focal adhesions, stress fibers and mechanical tension." Exp Cell Res **343**(1): 14-20.

Buxboim, A., J. Swift, J. Irianto, K. R. Spinler, P. C. Dingal, A. Athirasala, Y. R. Kao, S. Cho, T. Harada, J. W. Shin and D. E. Discher (2014). "Matrix elasticity regulates lamin-A,C phosphorylation and turnover with feedback to actomyosin." Curr Biol **24**(16): 1909-1917.

Cecile Gauthier-Rouviere, E. V., Mayya Meriane, Pierre Roux, Philippe Montcourier, Philippe Fort (1998). "RhoG GTPase Controls a Pathway That Independently
Activates Rac1 and Cdc42Hs." Molecular Biology of the Cell **9**: 1379 - 1394.

Chadi, S. M. C. G. (1999). "S100 IMMUNOREACTIVITY IS INCREASED IN REACTIVE ASTROCYTES OF THE VISUAL PATHWAYS FOLLOWING A MECHANICAL LESION OF THE RAT
OCCIPITAL CORTEX." Cell Biology International **24**(1): 35-49.

Charles M. Oman, I. P. H., Theodore Smith, Andrew C. Beall, Alan Natapoff, James E. Zacher, Heather L. Jenkin (2003). "The Role of Visual Cues in Microgravity Spatial Orientation." The Neurolab Spacelab Mission: Neuroscience Research in Space: Results from the STS-90, Neurolab Spacelab Mission.

Chen, M., C. G. Geoffroy, J. M. Meves, A. Narang, Y. Li, M. T. Nguyen, V. S. Khai, X. Kong, C. L. Steinke, K. I. Carolino, L. Elziere, M. P. Goldberg, Y. Jin and B. Zheng (2018). "Leucine Zipper-Bearing Kinase Is a Critical Regulator of Astrocyte Reactivity in the Adult Mammalian CNS." Cell Rep **22**(13): 3587-3597.

Cheng, S., V. Castillo, M. Welty, I. Eliaz and D. Sliva (2016). "Honokiol inhibits migration of renal cell carcinoma through activation of RhoA/ROCK/MLC signaling pathway." Int J Oncol **49**(4): 1525-1530.

Cornish, N., D. Blas and G. Nardini (2017). "Bounding the Speed of Gravity with Gravitational Wave Observations." Phys Rev Lett **119**(16): 161102.

Corydon, T. J., S. Kopp, M. Wehland, M. Braun, A. Schutte, T. Mayer, T. Hulsing, H. Oltmann, B. Schmitz, R. Hemmersbach and D. Grimm (2016). "Alterations of the cytoskeleton in human cells in space proved by life-cell imaging." Sci Rep **6**: 20043.

Costa-Almeida, R., D. T. Carvalho, M. J. Ferreira, G. Aresta, M. E. Gomes, J. J. van Loon, K. Van der Heiden and P. L. Granja (2016). "Effects of hypergravity on the angiogenic potential of endothelial cells." J R Soc Interface **13**(124).

Crossley, D., J. Hinderer and U. Riccardi (2013). "The measurement of surface gravity." Rep Prog Phys **76**(4): 046101.

Crucian, B. E., M. L. Cubbage and C. F. Sams (2000). "Altered cytokine production by specific human peripheral blood cell subsets immediately following space flight." J Interferon Cytokine Res **20**(6): 547-556.

Cunningham, L. A., M. Wetzel and G. A. Rosenberg (2005). "Multiple roles for MMPs and TIMPs in cerebral ischemia." Glia **50**(4): 329-339.

Davidson, P. M. and B. Cadot (2021). "Actin on and around the Nucleus." Trends Cell Biol **31**(3): 211-223.

Del Bigio, M. R. (2010). "Ependymal cells: biology and pathology." Acta Neuropathol **119**(1): 55-73.

Demertzi, A., A. Van Ombergen, E. Tomilovskaya, B. Jeurissen, E. Pechenkova, C. Di Perri, L. Litvinova, E. Amico, A. Rumshiskaya, I. Rukavishnikov, J. Sijbers, V. Sinitsyn, I. B. Kozlovskaya, S. Sunaert, P. M. Parizel, P. H. Van de Heyning, S. Laureys and F. L. Wuyts (2016). "Cortical reorganization in an astronaut's brain after long-duration spaceflight." Brain Struct Funct **221**(5): 2873-2876.

Donna R Roberts, A. C. S. and F. L. W. Rachael D Seidler (2020). "Towards understanding the effects of spaceflight on the brain." Lancet **19**: 808.

Eiermann, P., S. Kopp, J. Hauslage, R. Hemmersbach, R. Gerzer and K. Ivanova (2013). "Adaptation of a 2-D Clinostat for Simulated Microgravity Experiments with Adherent Cells." Microgravity Science and Technology **25**(3): 153-159.

Erturk, A., F. Hellal, J. Enes and F. Bradke (2007). "Disorganized microtubules underlie the formation of retraction bulbs and the failure of axonal regeneration." J Neurosci **27**(34): 9169-9180.

Escartin, C., E. Galea, A. Lakatos, J. P. O'Callaghan, G. C. Petzold, A. Serrano-Pozo, C. Steinhauser, A. Volterra, G. Carmignoto, A. Agarwal, N. J. Allen, A. Araque, L. Barbeito, A. Barzilai, D. E. Bergles, G. Bonvento, A. M. Butt, W. T. Chen, M. Cohen-Salmon, C. Cunningham, B. Deneen, B. De Strooper, B. Diaz-Castro, C. Farina, M. Freeman, V. Gallo, J. E. Goldman, S. A. Goldman, M. Gotz, A. Gutierrez, P. G. Haydon, D. H. Heiland, E. M. Hol, M. G. Holt, M. Iino, K. V. Kastanenka, H. Kettenmann, B. S. Khakh, S. Koizumi, C. J. Lee, S. A. Liddelow, B. A. MacVicar, P. Magistretti, A. Messing, A. Mishra, A. V. Molofsky, K. K. Murai, C. M. Norris, S. Okada, S. H. R. Oliet, J. F. Oliveira, A. Panatier, V. Parpura, M. Pekna, M. Pekny, L. Pellerin, G. Perea, B. G. Perez-Nievas, F. W. Pfrieger, K. E. Poskanzer, F. J. Quintana, R. M. Ransohoff, M. Riquelme-Perez, S. Robel, C. R. Rose, J. D. Rothstein, N. Rouach, D. H. Rowitch, A. Semyanov, S. Sirko, H. Sontheimer, R. A. Swanson, J. Vitorica, I. B. Wanner, L. B. Wood, J. Wu, B. Zheng, E. R. Zimmer, R. Zorec, M. V. Sofroniew and A. Verkhratsky (2021). "Reactive astrocyte nomenclature, definitions, and future directions." Nat Neurosci **24**(3): 312-325.

Fields, R. D., A. Araque, H. Johansen-Berg, S. S. Lim, G. Lynch, K. A. Nave, M. Nedergaard, R. Perez, T. Sejnowski and H. Wake (2014). "Glial biology in learning and cognition." Neuroscientist **20**(5): 426-431.

Fletcher, D. A. and R. D. Mullins (2010). "Cell mechanics and the cytoskeleton." Nature **463**(7280): 485-492.

Frett, T., G. Petrat, J. J. W. A. van Loon, R. Hemmersbach and R. Anken (2015). "Hypergravity Facilities in the ESA Ground-Based Facility Program – Current Research Activities and Future Tasks." Microgravity Science and Technology **28**(3): 205-214.

Fukata, M. W., T.; Noritake, J.; Nakagawa, M.; Yamaga, M.; Kuroda, S.; Matsuura, Y.; Iwamatsu, A.; and F. K. Perez, K. (2002). "Rac1 and Cdc42 capture microtubules through IQGAP1 and CLIP-170." Cell **109**.

Galimberti, M., I. M. Tolic-Norrelykke, R. Favillini, R. Mercatelli, F. Annunziato, L. Cosmi, F. Liotta, V. Santarlasci, E. Maggi and F. S. Pavone (2006). "Hypergravity speeds up the development of T-lymphocyte motility." Eur Biophys J **35**(5): 393-400.
0
Garcia-Caceres, C., C. Quarta, L. Varela, Y. Gao, T. Gruber, B. Legutko, M. Jastroch, P. Johansson, J. Ninkovic, C. X. Yi, O. Le Thuc, K. Szigeti-Buck, W. Cai, C. W. Meyer, P. T. Pfluger, A. M. Fernandez, S. Luquet, S. C. Woods, I. Torres-Aleman, C. R. Kahn, M. Gotz, T. L. Horvath and M. H. Tschop (2016). "Astrocytic Insulin Signaling Couples Brain Glucose Uptake with Nutrient Availability." Cell **166**(4): 867-880.

Genchi, G. G., F. Cialdai, M. Monici, B. Mazzolai, V. Mattoli and G. Ciofani (2015). "Hypergravity stimulation enhances PC12 neuron-like cell differentiation." Biomed Res Int **2015**: 748121.

Grimm, D., M. Egli, M. Kruger, S. Riwaldt, T. J. Corydon, S. Kopp, M. Wehland, P. Wise, M. Infanger, V. Mann and A. Sundaresan (2018). "Tissue Engineering Under Microgravity Conditions-Use of Stem Cells and Specialized Cells." Stem Cells Dev **27**(12): 787-804.

Grimm, D., H. Schulz, M. Kruger, J. L. Cortes-Sanchez, M. Egli, A. Kraus, J. Sahana, T. J. Corydon, R. Hemmersbach, P. M. Wise, M. Infanger and M. Wehland (2022). "The Fight against Cancer by Microgravity: The Multicellular Spheroid as a Metastasis Model." Int J Mol Sci **23**(6).

Grosser, S., J. Lippoldt, L. Oswald, M. Merkel, D. M. Sussman, F. Renner, P. Gottheil, E. W. Morawetz, T. Fuhs, X. Xie, S. Pawlizak, A. W. Fritsch, B. Wolf, L.-C. Horn, S. Briest, B. Aktas, M. L. Manning and J. A. Käs (2021). "Cell and Nucleus Shape as an Indicator of Tissue Fluidity in Carcinoma." Physical Review X **11**(1).

Gu, Z., E. H. Noss, V. W. Hsu and M. B. Brenner (2011). "Integrins traffic rapidly via circular dorsal ruffles and macropinocytosis during stimulated cell migration." J Cell Biol **193**(1): 61-70.

Gurniak, C. B., E. Perlas and W. Witke (2005). "The actin depolymerizing factor n-cofilin is essential for neural tube morphogenesis and neural crest cell migration." Dev Biol **278**(1): 231-241.

Häder, D. P., M. Braun, D. Grimm and R. Hemmersbach (2017). "Gravireceptors in eukaryotes-a comparison of case studies on the cellular level." NPJ Microgravity **3**(1): 13.

Hanahan, D. and R. A. Weinberg (2011). "Hallmarks of cancer: the next generation." Cell **144**(5): 646-674.

Hanke, W., F. P. M. Kohn, M. Neef and R. Hampp (2018). Gravitational Biology II Interaction of Gravity with Cellular Components and Cell Metabolism. G. Ruyters and M. Braun, Springer.

Hara, M., K. Kobayakawa, Y. Ohkawa, H. Kumamaru, K. Yokota, T. Saito, K. Kijima, S. Yoshizaki, K. Harimaya, Y. Nakashima and S. Okada (2017). "Interaction of reactive astrocytes with type I collagen induces astrocytic scar formation through the integrin-N-cadherin pathway after spinal cord injury." Nat Med **23**(7): 818-828.

Hauslage, J., V. Cevik and R. Hemmersbach (2017). "Pyrocystis noctiluca represents an excellent bioassay for shear forces induced in ground-based microgravity simulators (clinostat and random positioning machine)." NPJ Microgravity **3**(1): 12.

Herranz, R., R. Anken, J. Boonstra, M. Braun, P. C. Christianen, M. de Geest, J. Hauslage, R. Hilbig, R. J. Hill, M. Lebert, F. J. Medina, N. Vagt, O. Ullrich, J. J. van Loon and R. Hemmersbach (2013). "Ground-based facilities for simulation of microgravity: organism-specific recommendations for their use, and recommended terminology." Astrobiology **13**(1): 1-17.

Hodge, R. G. and A. J. Ridley (2016). "Regulating Rho GTPases and their regulators." Nat Rev Mol Cell Biol **17**(8): 496-510.

Hohmann, T. and F. Dehghani (2019). "The Cytoskeleton-A Complex Interacting Meshwork." Cells **8**(4).

Hughes-Fulford, M. (2003). "Function of the cytoskeleton in gravisensing during spaceflight." Adv Space Res **32**(8): 1585-1593.

Hur, E. M., Saijilafu and F. Q. Zhou (2012). "Growing the growth cone: remodeling the cytoskeleton to promote axon regeneration." Trends Neurosci **35**(3): 164-174.

Ishibashi, T., K. A. Dakin, B. Stevens, P. R. Lee, S. V. Kozlov, C. L. Stewart and R. D. Fields (2006). "Astrocytes promote myelination in response to electrical impulses." Neuron **49**(6): 823-832.

Jakel, S. and L. Dimou (2017). "Glial Cells and Their Function in the Adult Brain: A Journey through the History of Their Ablation." Front Cell Neurosci **11**: 24.

Janmey, P. A., B. Hinz and C. A. McCulloch (2021). "Physics and Physiology of Cell Spreading in Two and Three Dimensions." Physiology (Bethesda) **36**(6): 382-391.

Kalb, H., DeFelipe, Garcia-Segura, Walton, Llinas (2003). "Motor System Development Depends on Experience: A microgravity study of rats." The Neurolab Spacelab Mission: Neuroscience Research in Space: Results from the STS-90, Neurolab Spacelab Mission.

Kamermans, A., K. E. Planting, K. Jalink, J. van Horssen and H. E. de Vries (2019). "Reactive astrocytes in multiple sclerosis impair neuronal outgrowth through TRPM7-mediated chondroitin sulfate proteoglycan production." Glia **67**(1): 68-77.

Kanas, N. and D. Manzey (2008). Space Psychology and Psychiatry, Springer Netherlands.

King, C. M., K. Bohmbach, D. Minge, A. Delekate, K. Zheng, J. Reynolds, C. Rakers, A. Zeug, G. C. Petzold, D. A. Rusakov and C. Henneberger (2020). "Local Resting Ca(2+) Controls the Scale of Astroglial Ca(2+) Signals." Cell Rep **30**(10): 3466-3477 e3464.

Kirby, T. J. and J. Lammerding (2018). "Emerging views of the nucleus as a cellular mechanosensor." Nat Cell Biol **20**(4): 373-381.

Komarova, Y., C. O. De Groot, I. Grigoriev, S. M. Gouveia, E. L. Munteanu, J. M. Schober, S. Honnappa, R. M. Buey, C. C. Hoogenraad, M. Dogterom, G. G. Borisy, M. O. Steinmetz and A. Akhmanova (2009). "Mammalian end binding proteins control persistent microtubule growth." J Cell Biol **184**(5): 691-706
.
Koppelmans, V., J. J. Bloomberg, A. P. Mulavara and R. D. Seidler (2016). "Brain structural plasticity with spaceflight." NPJ Microgravity **2**: 2.

Kovar, D. R., E. S. Harris, R. Mahaffy, H. N. Higgs and T. D. Pollard (2006). "Control of the assembly of ATP- and ADP-actin by formins and profilin." Cell **124**(2): 423-435.

Koyama, T., C. Kimura, M. Hayashi, M. Watanabe, Y. Karashima and M. Oike (2009). "Hypergravity induces ATP release and actin reorganization via tyrosine phosphorylation and RhoA activation in bovine endothelial cells." Pflugers Arch **457**(4): 711-719.

Kraft, A. W., X. Hu, H. Yoon, P. Yan, Q. Xiao, Y. Wang, S. C. Gil, J. Brown, U. Wilhelmsson, J. L. Restivo, J. R. Cirrito, D. M. Holtzman, J. Kim, M. Pekny and J. M. Lee (2013). "Attenuating astrocyte activation accelerates plaque pathogenesis in APP/PS1 mice." FASEB J **27**(1): 187-198.

Krause, M. and A. Gautreau (2014). "Steering cell migration: lamellipodium dynamics and the regulation of directional persistence." Nat Rev Mol Cell Biol **15**(9): 577-590.

Lagos-Cabre, R., A. Alvarez, M. Kong, F. Burgos-Bravo, A. Cardenas, E. Rojas-Mancilla, R. Perez-Nunez, R. Herrera-Molina, F. Rojas, P. Schneider, M. Herrera-Marschitz, A. F. G. Quest, B. van Zundert and L. Leyton (2017). "alphaVbeta3 Integrin regulates astrocyte reactivity." J Neuroinflammation **14**(1): 194.

Lagos-Cabre, R., F. Burgos-Bravo, A. M. Avalos and L. Leyton (2019). "Connexins in Astrocyte Migration." Front Pharmacol **10**: 1546.

LeBlanc, A., C. Lin, L. Shackelford, V. Sinitsyn, H. Evans, O. Belichenko, B. Schenkman, I. Kozlovskaya, V. Oganov, A. Bakulin, T. Hedrick and D. Feeback (2000). "Muscle volume, MRI relaxation times (T2), and body composition after spaceflight." J Appl Physiol (1985) **89**(6): 2158-2164.

Lee, A. G., T. H. Mader, C. R. Gibson, W. Tarver, P. Rabiei, R. F. Riascos, L. A. Galdamez and T. Brunstetter (2020). "Spaceflight associated neuro-ocular syndrome (SANS) and the neuro-ophthalmologic effects of microgravity: a review and an update." NPJ Microgravity **6**: 7.

Lee, M., D. Kim and S. Kwon (2021). "Hypergravity-induced changes in actin response of breast cancer cells to natural killer cells." Sci Rep **11**(1): 7267.

Lichterfeld, Y., L. Kalinski, S. Schunk, T. Schmakeit, S. Feles, T. Frett, H. Herrmann, R. Hemmersbach and C. Liemersdorf (2022). "Hypergravity Attenuates Reactivity in Primary Murine Astrocytes." Biomedicines **10**(8).

Liddelow, S. A. and B. A. Barres (2017). "Reactive Astrocytes: Production, Function, and Therapeutic Potential." Immunity **46**(6): 957-967.

Liddelow, S. A., K. A. Guttenplan, L. E. Clarke, F. C. Bennett, C. J. Bohlen, L. Schirmer, M. L. Bennett, A. E. Munch, W. S. Chung, T. C. Peterson, D. K. Wilton, A. Frouin, B. A. Napier, N. Panicker, M. Kumar, M. S. Buckwalter, D. H. Rowitch, V. L. Dawson, T. M. Dawson, B. Stevens and B. A. Barres (2017). "Neurotoxic reactive astrocytes are induced by activated microglia." Nature **541**(7638): 481-487.

Liemersdorf, C., Y. Lichterfeld, R. Hemmersbach and J. Hauslage (2020). "The MAPHEUS module CellFix for studying the influence of altered gravity on the physiology of single cells." Rev Sci Instrum **91**(1): 014101.

Madaule, P. A., R. (1985). "A novel ras related gene family." Cell **41**: 31 - 40.

Maier, J. A., F. Cialdai, M. Monici and L. Morbidelli (2015). "The impact of microgravity and hypergravity on endothelial cells." Biomed Res Int **2015**: 434803.

Marian Lewis, J. R., Luis. Cubano, Jason Hatton, B. Desales Lawless, Eward Piepmeier (1998). "Spaceflight alters microtubules and increases apoptosis in human lymphocytes (Jurkat)." The FASEB Journal.

Martin Paez, Y., L. I. Mudie and P. S. Subramanian (2020). "Spaceflight Associated Neuro-Ocular Syndrome (SANS): A Systematic Review and Future Directions." Eye Brain **12**: 105-117.

Matsui, T., T. Ishikawa, H. Ito, M. Okamoto, K. Inoue, M. C. Lee, T. Fujikawa, Y. Ichitani, K. Kawanaka and H. Soya (2012). "Brain glycogen supercompensation following exhaustive exercise." J Physiol **590**(3): 607-616.

Middeldorp, J. and E. M. Hol (2011). "GFAP in health and disease." Prog Neurobiol **93**(3): 421-443.

Miller, P. M., A. W. Folkmann, A. R. Maia, N. Efimova, A. Efimov and I. Kaverina (2009). "Golgi-derived CLASP-dependent microtubules control Golgi organization and polarized trafficking in motile cells." Nat Cell Biol **11**(9): 1069-1080.

Moeton, M., O. M. Stassen, J. A. Sluijs, V. W. van der Meer, L. J. Kluivers, H. van Hoorn, T. Schmidt, E. A. Reits, M. E. van Strien and E. M. Hol (2016). "GFAP isoforms control intermediate filament network dynamics, cell morphology, and focal adhesions." Cell Mol Life Sci **73**(21): 4101-4120.

Moll, R., M. Divo and L. Langbein (2008). "The human keratins: biology and pathology." Histochem Cell Biol **129**(6): 705-733.

Morris, E. J., G. P. Nader, N. Ramalingam, F. Bartolini and G. G. Gundersen (2014). "Kif4 interacts with EB1 and stabilizes microtubules downstream of Rho-mDia in migrating fibroblasts." PLoS One **9**(3): e91568.

Motulsky, H. J. and R. E. Brown (2006). "Detecting outliers when fitting data with nonlinear regression - a new method based on robust nonlinear regression and the false discovery rate." BMC Bioinformatics **7**: 123.

Nakamura, M. Z., X.Z.; Lu, K.P (2001). "Critical role for the EB1 and APC interaction in the regulation of microtubule polymerization." Curr Biol **11**: 1065 - 1067.

Nassef, M. Z., S. Kopp, M. Wehland, D. Melnik, J. Sahana, M. Kruger, T. J. Corydon, H. Oltmann, B. Schmitz, A. Schutte, T. J. Bauer, M. Infanger and D. Grimm (2019). "Real Microgravity Influences the Cytoskeleton and Focal Adhesions in Human Breast Cancer Cells." Int J Mol Sci **20**(13).

Nathan, F. M. and S. Li (2017). "Environmental cues determine the fate of astrocytes after spinal cord injury." Neural Regen Res **12**(12): 1964-1970.

Naumanen, P. L., P.; Hotulainen (2008). "Mechanisms of actin stress fibre assembly." J. Microsc **231**: 446 - 454.

Ohi, R. and M. Zanic (2016). "Ahead of the Curve: New Insights into Microtubule Dynamics." F1000Res **5**.

Okada, S., M. Hara, K. Kobayakawa, Y. Matsumoto and Y. Nakashima (2018). "Astrocyte reactivity and astrogliosis after spinal cord injury." Neurosci Res **126**: 39-43.

Okada, S., M. Nakamura, H. Katoh, T. Miyao, T. Shimazaki, K. Ishii, J. Yamane, A. Yoshimura, Y. Iwamoto, Y. Toyama and H. Okano (2006). "Conditional ablation of Stat3 or Socs3 discloses a dual role for reactive astrocytes after spinal cord injury." Nat Med **12**(7): 829-834.

Ombergen, A. V. (2018). "Brain Tissue–Volume Changes in Cosmonauts." N. Engl. J. Med **379**.

Omura, T., K. Omura, A. Tedeschi, P. Riva, M. W. Painter, L. Rojas, J. Martin, V. Lisi, E. A. Huebner, A. Latremoliere, Y. Yin, L. B. Barrett, B. Singh, S. Lee, T. Crisman, F. Gao, S. Li, K. Kapur, D. H. Geschwind, K. S. Kosik, G. Coppola, Z. He, S. T. Carmichael, L. I. Benowitz, M. Costigan and C. J. Woolf (2015). "Robust Axonal Regeneration Occurs in the Injured CAST/Ei Mouse CNS." Neuron **86**(5): 1215-1227.

Paulsen, K., C. Thiel, J. Timm, P. M. Schmidt, K. Huber, S. Tauber, R. Hemmersbach, D. Seibt, H. Kroll, K.-H. Grote, F. Zipp, R. Schneider-Stock, A. Cogoli, A. Hilliger, F. Engelmann and O. Ullrich (2010). "Microgravity-induced alterations in signal transduction in cells of the immune system." Acta Astronautica **67**(9-10): 1116-1125.

Pekny, M., C. B. Johansson, C. Eliasson, J. Stakeberg, A. Wallen, T. Perlmann, U. Lendahl, C. Betsholtz, C. H. Berthold and J. Frisen (1999). "Abnormal reaction to central nervous system injury in mice lacking glial fibrillary acidic protein and vimentin." J Cell Biol **145**(3): 503-514.

Pekny, M. and M. Nilsson (2005). "Astrocyte activation and reactive gliosis." Glia **50**(4): 427-434.
Pekny, M. and M. Pekna (2014). "Astrocyte reactivity and reactive astrogliosis: costs and benefits." Physiol Rev **94**(4): 1077-1098.

Pellegrin, S. and H. Mellor (2007). "Actin stress fibres." J Cell Sci **120**(Pt 20): 3491-3499.

Petry, S. (2016). "Mechanisms of Mitotic Spindle Assembly." Annu Rev Biochem **85**: 659-683.

Pollard, T. D. (2016). "Actin and Actin-Binding Proteins." Cold Spring Harb Perspect Biol **8**(8).

Popova, N. K., A. V. Kulikov and V. S. Naumenko (2020). "Spaceflight and brain plasticity: Spaceflight effects on regional expression of neurotransmitter systems and neurotrophic factors encoding genes." Neurosci Biobehav Rev **119**: 396-405.

Porseva, V. V., V. V. Shilkin, A. A. Strelkov, I. B. Krasnov and P. M. Masliukov (2017). "Changes in the Neurochemical Composition of Motor Neurons of the Spinal Cord in Mice under Conditions of Space Flight." Bull Exp Biol Med **162**(3): 336-339.

Retamal, M. A., N. Froger, N. Palacios-Prado, P. Ezan, P. J. Saez, J. C. Saez and C. Giaume (2007). "Cx43 hemichannels and gap junction channels in astrocytes are regulated oppositely by proinflammatory cytokines released from activated microglia." J Neurosci **27**(50): 13781-13792.

Ridley, A. J. (2011). "Life at the leading edge." Cell **145**(7): 1012-1022.

Riedl, J., A. H. Crevenna, K. Kessenbrock, J. H. Yu, D. Neukirchen, M. Bista, F. Bradke, D. Jenne, T. A. Holak, Z. Werb, M. Sixt and R. Wedlich-Soldner (2008). "Lifeact: a versatile marker to visualize F-actin." Nat Methods **5**(7): 605-607.

Romero, M. I., L. Lin, M. E. Lush, L. Lei, L. F. Parada and Y. Zhu (2007). "Deletion of Nf1 in neurons induces increased axon collateral branching after dorsal root injury." J Neurosci **27**(8): 2124-2134.

Rosner, H., T. Wassermann, W. Moller and W. Hanke (2006). "Effects of altered gravity on the actin and microtubule cytoskeleton of human SH-SY5Y neuroblastoma cells." Protoplasma **229**(2-4): 225-234.

Ross, M. D. (2009). "A Spaceflight Study of Synaptic Plasticity in Adult Rat Vestibular Maculas." Acta Oto-Laryngologica **114**(sup516): 3-14.

Rotty, J. D. and J. E. Bear (2014). "Competition and collaboration between different actin assembly pathways allows for homeostatic control of the actin cytoskeleton." Bioarchitecture **5**(1-2): 27-34.

Sachs, J. (1882). Arbeiten des Botanischen Institus in Würzburg.

Schatten, H., M. L. Lewis and A. Chakrabarti (2001). "Spaceflight and clinorotation cause cytoskeleton and mitochondria changes and increases in apoptosis in cultured cells." Acta Astronaut **49**(3-10): 399-418.

Schildge, S., C. Bohrer, K. Beck and C. Schachtrup (2013). "Isolation and culture of mouse cortical astrocytes." J Vis Exp(71).

Schiweck, J., B. J. Eickholt and K. Murk (2018). "Important Shapeshifter: Mechanisms Allowing Astrocytes to Respond to the Changing Nervous System During Development, Injury and Disease." Front Cell Neurosci **12**: 261.

Semyanov, A., C. Henneberger and A. Agarwal (2020). "Making sense of astrocytic calcium signals - from acquisition to interpretation." Nat Rev Neurosci **21**(10): 551-564.

Shaopeng Chi, Y. C., Haiping Wang, Jinghui Jiang, Tingxin Zhang, Suhua Sun, Zhuan Zhou, Yi Zhong, Bailong Xiao, (2022). "Astrocytic Piezo1-mediated mechanotransduction determines adult neurogenesis and cognitive functions." Neuron **110**(18): 2984-2999.

Skinner, B. M. and E. E. Johnson (2017). "Nuclear morphologies: their diversity and functional relevance." Chromosoma **126**(2): 195-212.

Sofroniew, M. V. (2009). "Molecular dissection of reactive astrogliosis and glial scar formation." Trends Neurosci **32**(12): 638-647.

Sofroniew, M. V. and H. V. Vinters (2010). "Astrocytes: biology and pathology." Acta Neuropathol **119**(1): 7-35.

Sosunov, A., X. Wu, R. McGovern, C. Mikell, G. M. McKhann and J. E. Goldman (2020). "Abnormal mitosis in reactive astrocytes." Acta Neuropathologica Communications **8**(1).

Sulkowski, G. M., G. H. Li and E. M. Sajdel-Sulkowska (2004). "Environmental impacts on the developing CNS: CD15, NCAM-L1, and GFAP expression in rat neonates exposed to hypergravity." Adv Space Res **33**(8): 1423-1430.

Takemura, M. and S. Yoshida (2001). "Stimulation of DNA polymerase alpha by hypergravity generated by centrifugal acceleration." Biochem Biophys Res Commun **289**(2): 345-349.

Tedeschi, A. and F. Bradke (2017). "Spatial and temporal arrangement of neuronal intrinsic and extrinsic mechanisms controlling axon regeneration." Curr Opin Neurobiol **42**: 118-127.

Thomas D. Pollard, R. R. W. M. R. A. (1974). "Actin And Myosin And Cell Movement." CRC Critical Reviews in Biochemistry **2**: 1 - 65.

Thornton, M. A. and E. G. Hughes (2020). "Neuron-oligodendroglia interactions: Activity-dependent regulation of cellular signaling." Neurosci Lett **727**: 134916.

Tominari, T., R. Ichimaru, K. Taniguchi, A. Yumoto, M. Shirakawa, C. Matsumoto, K. Watanabe, M. Hirata, Y. Itoh, D. Shiba, C. Miyaura and M. Inada (2019). "Hypergravity and microgravity exhibited reversal effects on the bone and muscle mass in mice." Sci Rep **9**(1): 6614.

Turovsky, E. A., A. Braga, Y. Yu, N. Esteras, A. Korsak, S. M. Theparambil, A. Hadjihambi, P. S. Hosford, A. G. Teschemacher, N. Marina, M. F. Lythgoe, P. G. Haydon and A. V. Gourine (2020). "Mechanosensory Signaling in Astrocytes." J Neurosci **40**(49): 9364-9371.

Uva, B. M., M. A. Masini, M. Sturla, P. Prato, M. Passalacqua, M. Giuliani, G. Tagliafierro and F. Strollo (2002). "Clinorotation-induced weightlessness influences the cytoskeleton of glial cells in culture." Brain Res **934**(2): 132-139.

van Loon, J. J. W. A. (2016). "Centrifuges for Microgravity Simulation. The Reduced Gravity Paradigm." Frontiers in Astronomy and Space Sciences **3**.

Van Ombergen, A., A. Demertzi, E. Tomilovskaya, B. Jeurissen, J. Sijbers, I. B. Kozlovskaya, P. M. Parizel, P. H. Van de Heyning, S. Sunaert, S. Laureys and F. L. Wuyts (2017). "The effect of spaceflight and microgravity on the human brain." J Neurol **264**(Suppl 1): 18-22.

Van Ombergen, A., Jillings, S., Jeurissen, B., Tomilovskaya, E., Rühl, R. M., Rumshiskaya, A. (2018). "Brain Tissue-Volume Changes in Cosmonauts." N. Engl. J. Med **379**: 1678-1680.

Vassy, J., Portet, S., Beil, M., Millot, G., Fauvel-Lafève, F., Karniguian, A., Gasset, G.,R and T. Irinopoulou, Calvo, F., Rigaut, J.P., Schoevaert, D (2001). "Effect of weightlessness on cytoskeleton architecture and

proliferation of human breast cancer cell line MCF-7." The FASEB Journal.

Verkhratsky, A. and M. Nedergaard (2018). "Physiology of Astroglia." Physiol Rev **98**(1): 239-389.

Verslegers, M., K. Lemmens, I. Van Hove and L. Moons (2013). "Matrix metalloproteinase-2 and -9 as promising benefactors in development, plasticity and repair of the nervous system." Prog Neurobiol **105**: 60-78.

Vignjevic, D., D. Yarar, M. D. Welch, J. Peloquin, T. Svitkina and G. G. Borisy (2003). "Formation of filopodia-like bundles in vitro from a dendritic network." J Cell Biol **160**(6): 951-962.

von Bartheld, C. S., J. Bahney and S. Herculano-Houzel (2016). "The search for true numbers of neurons and glial cells in the human brain: A review of 150 years of cell counting." J Comp Neurol **524**(18): 3865-3895.

Walz, W. (2000). "Role of astrocytes in the clearance of excess extracellular potassium." Neurochem Int **36**(4-5): 291-300.

Wittmann, T., G. M. Bokoch and C. M. Waterman-Storer (2003). "Regulation of leading edge microtubule and actin dynamics downstream of Rac1." J Cell Biol **161**(5): 845-851.

Wollseiffen, P., T. Klein, T. Vogt, V. Abeln, H. K. Struder, T. Stuckenschneider, M. Sanders, J. Claassen, C. D. Askew, H. Carnahan and S. Schneider (2019). "Neurocognitive performance is enhanced during short periods of microgravity-Part 2." Physiol Behav **207**: 48-54.

Wuest, S. L., J. Arnold, S. Gander, C. Zumbühl, C. Jost, C. Giger-Lange, G. Cerretti, M. Caliò, K. Rattenbacher-Kiser, C. Follonier, O. Schälli, G. S. Székely, M. Egli and F. Ille (2020). "Microtubules and Vimentin Fiber Stability during Parabolic Flights." Microgravity Science and Technology **32**(5): 921-933.

Xiong, Y., S. Sun, S. Teng, M. Jin and Z. Zhou (2018). "Ca(2+)-Dependent and Ca(2+)-Independent ATP Release in Astrocytes." Front Mol Neurosci **11**: 224.

Xue, L., Y. Li and J. Chen (2017). "Duration of simulated microgravity affects the differentiation of mesenchymal stem cells." Mol Med Rep **15**(5): 3011-3018.

Yang, C., R. R. Iyer, A. C. Yu, R. L. Yong, D. M. Park, R. J. Weil, B. Ikejiri, R. O. Brady, R. R. Lonser and Z. Zhuang (2012). "beta-Catenin signaling initiates the activation of astrocytes and its dysregulation contributes to the pathogenesis of astrocytomas." Proc Natl Acad Sci U S A **109**(18): 6963-6968.

Yu, H., M. Gao, Y. Ma, L. Wang, Y. Shen and X. Liu (2018). "Inhibition of cell migration by focal adhesion kinase: Time-dependent difference in integrin-induced signaling between endothelial and hepatoblastoma cells." Int J Mol Med **41**(5): 2573-2588.

Zhan, J. S., K. Gao, R. C. Chai, X. H. Jia, D. P. Luo, G. Ge, Y. W. Jiang, Y. W. Fung, L. Li and A. C. Yu (2017). "Astrocytes in Migration." Neurochem Res **42**(1): 272-282.

7. Supplementary Material

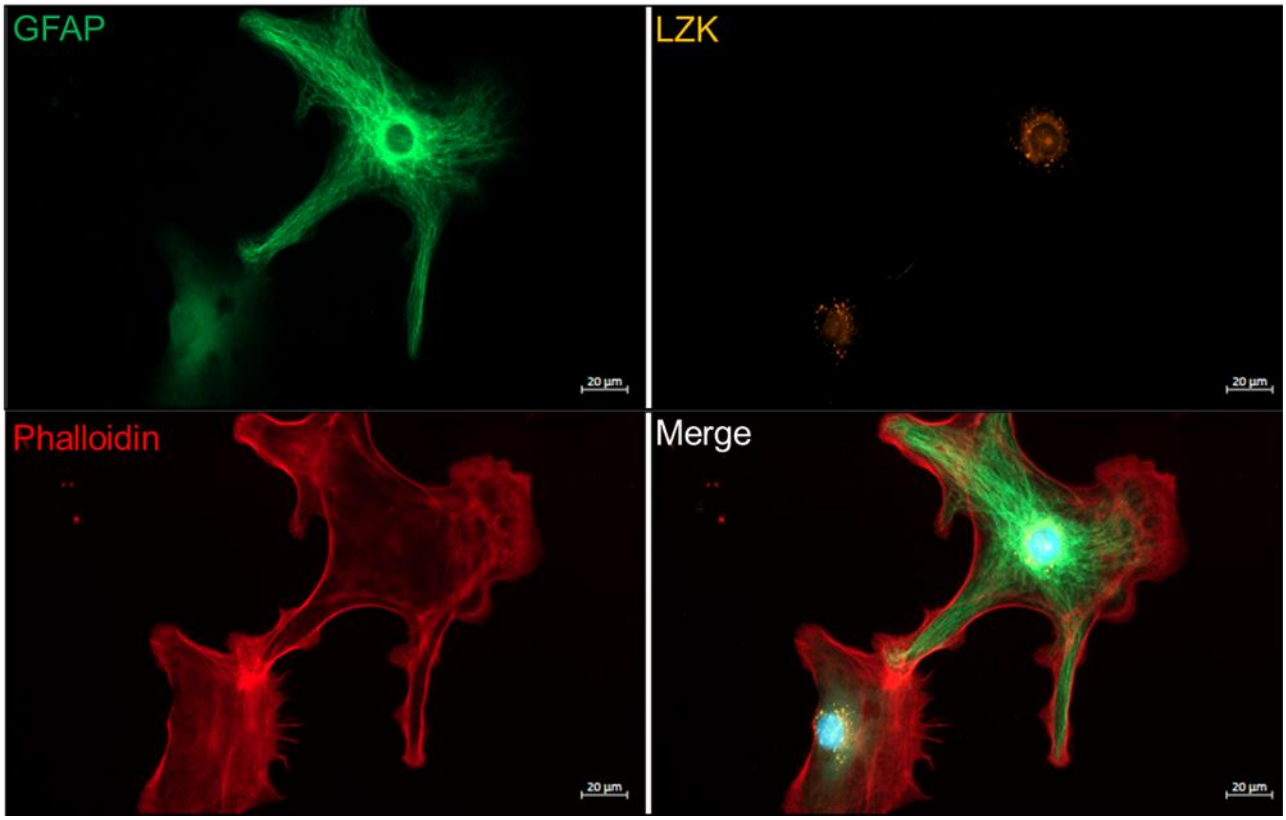

Supplementary Figure 1: Immunofluorescence staining of the reactivity markers GFAP and LZK.

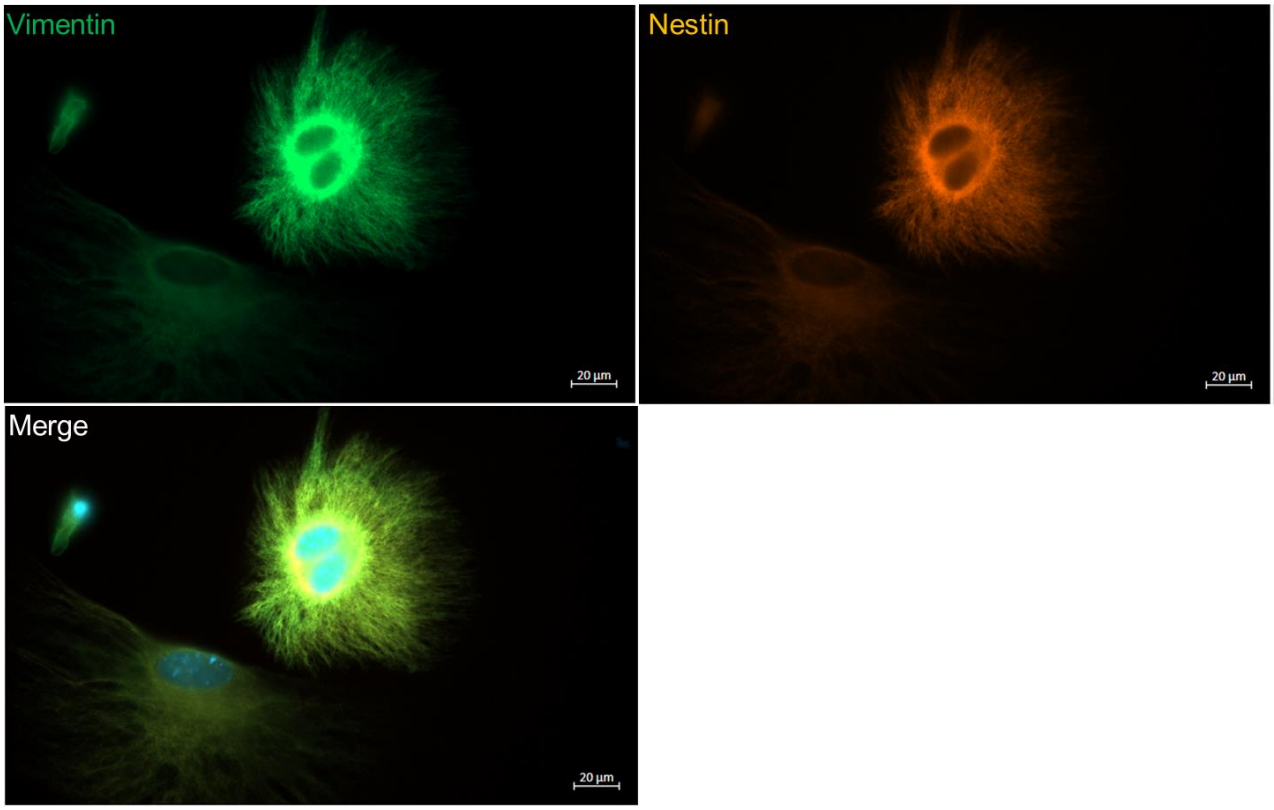

Supplementary Figure 2: Immunofluorescence staining of the reactivity markers vimentin and nestin.